



DEPARTMENT OF PHYSICS

UNIVERSITY OF CAPE TOWN

IYUNIVESITHI YASEKAPA • UNIVERSITEIT VAN KAAPSTAD

Search for tWZ production in the Full Run 2 ATLAS
dataset using events with four leptons

Jake Reich

Student Number: RCHJAK001

Supervisor: Dr. James Keaveney

Co-Supervisor: Dr. Sahal Yacoob

A thesis submitted in fulfilment
of the requirements for the degree of
Master in Science

August 2021

Abstract

The search for tWZ production using 139 fb^{-1} of pp collision data at a centre-of-mass energy of $\sqrt{s} = 13 \text{ TeV}$, recorded by the ATLAS experiment at CERN, is presented. Events containing exactly four electrons or muons (tetralepton) are selected with additional criteria based on the number of jets, the number of b -tagged jets, and the number of Z boson candidates are used to define signal and control regions. The large $t\bar{t}Z$ and ZZ backgrounds are distinguished from signal by a BDT-based algorithm. Inputs to the BDT-based algorithm include, a kinematic reconstruction algorithm which reconstructs leptonically decaying top quarks and a BDT-based algorithm which aims to classify ℓb systems originating from top quarks. The expected signal strength is extracted via a blinded maximum-likelihood fit to multiple signal and control regions. The measured signal strength is $\mu(tWZ) = 1.91^{+0.95}_{-0.82}$, leading to an expected significance of 1.44σ . An expected upper limit on the signal strength is set and is given by $\mu_{up}^{exp} = 1.61^{+2.35}_{-1.16}$. Furthermore, a combined blinded maximum-likelihood fit was performed across the tetralepton and trilepton (studied in an independent analysis by Benjamin Warren (UCT) [66]) channels, to further increase the sensitivity of $\sigma(tWZ)$. The measured signal strength is $\mu(tWZ) = 1.80^{+0.70}_{-0.65}$, leading to an expected significance of 1.61σ . An expected upper limit on the signal strength is set and is given by $\mu_{up}^{exp} = 1.43^{+2.04}_{-1.03}$.

Declaration

*17 I certify that this assignment/report is my own work, based on my personal study and/or research and that I have
18 acknowledged all material and sources used in its preparation, whether they be books, articles, reports, lecture notes,
19 and any other kind of document, electronic or personal communication. I also certify that this assignment/report
20 has not previously been submitted for assessment in any other unit, except where specific permission has been granted
21 from all unit coordinators involved, or at any other time in this unit, and that I have not copied in part or whole
22 or otherwise plagiarised the work of other students and/or persons.*

Acknowledgements

24

Contents

25	1 Introduction	7
26	2 Theory	8
27	2.1 Standard Model of Particle Physics	8
28	2.1.1 The Top Quark	9
29	2.2 tWZ	10
30	2.2.1 Tetralepton Channel	10
31	2.2.2 Comparison to Trilepton Channel	11
32	2.2.3 Motivation for the search for tWZ production in the tetralepton channel	12
33	3 The ATLAS Experiment and Detector	13
34	3.1 The ATLAS Experiment	13
35	3.1.1 Large Hadron Collider (LHC)	13
36	3.2 The ATLAS Detector	14
37	3.2.1 Coordinate System and Kinematics	15
38	3.2.2 Inner Detector	15
39	3.2.3 Electromagnetic and Hadronic Calorimeters	16
40	3.2.4 Muon Spectrometer	16
41	3.2.5 Trigger and Data Acquisition System	16
42	3.2.6 Particle Identification and Object Reconstruction	16
43	4 Analysis Setup and Strategy	19
44	4.1 Data and Monte Carlo Simulation	19
45	4.1.1 Data Samples	19
46	4.1.2 Monte Carlo Samples	19
47	4.2 Objects	20
48	4.2.1 Leptons	21
49	4.2.2 Jets	21
50	4.2.3 b -tagging	22
51	4.3 Kinematic cuts	22
52	4.4 Regions and Event Selection	22
53	4.4.1 Optimization studies for event selection	23
54	4.5 Signal and Control Regions	25
55	4.5.1 tWZ OF SR	27
56	4.5.2 tWZ SF SR	27
57	4.5.3 $t\bar{t}Z$ CR	28
58	4.5.4 $Z Z b$ CR	28
59	4.5.5 $(tWZ)_{\text{fake}}$ CR	37
60	4.6 Fake Lepton Estimation	37
61	4.7 Machine Learning Techniques	44
62	4.7.1 Object-level BDT	46
63	4.7.2 Event-level BDT	52
64	4.8 Two Neutrino Scanning Method ($2\nu\text{SM}$) Algorithm	57
65	4.8.1 The algorithm	57
66	4.8.2 Calculating $w_{2\nu\text{SM}}$	58

67	4.8.3 Kinematic Veto	59
68	4.9 Systematics	61
69	4.9.1 Experimental uncertainties	62
70	4.9.2 Theoretical uncertainties	64
71	4.9.3 Generic shape systematics	64
72	4.10 Analysis Pipeline and TRexFitter	65
73	4.10.1 Fitting Procedure	66
74	4.11 Results	67
75	4.11.1 Tetralepton Channel	67
76	4.11.2 Trilepton and Tetralepton Channels	69
77	5 Conclusion	75
78	A Appendix	76
79	A.1 Pre-Fit Plots	76
80	A.1.1 tWZ OF SR	76
81	A.1.2 tWZ SF SR	83
82	A.1.3 $t\bar{t}Z$ CR	90
83	A.1.4 ZZb CR	97
84	A.1.5 $(tWZ)_{\text{fake}}$ CR	105

85

Chapter 1

86

Introduction

87 The production of a single top quark in association with a W^\pm and Z boson ($tW^\pm Z$) at the CERN LHC is sensitive
 88 to both the neutral and charged electroweak couplings of the top quark as the process involves the simultaneous
 89 production of a W boson and a Z boson in association with the top quark. Due to the very large coupling of the
 90 top quark to the Higgs boson, the electroweak couplings of the top quark are a theoretically well-motivated area in
 91 which to search for the first signs of new physics. The recent lack of signs of new physics from LHC data tells us
 92 that new physics is either very heavy, or is very weakly coupled to Standard Model particles, therefore we might
 93 only observe signs of new physics in anomalous rates of well-chosen processes. A prime example of such a process
 94 is tWZ . This has an extremely low production cross section (0.7 fb for $\sqrt{s} = 13$ TeV [23]), meaning that it is an
 95 extremely rare process to observe and subsequently, it has never been observed by any particle physics experiment.
 96 However, the latest datasets recorded by the ATLAS experiment at the CERN LHC are sufficiently large to allow
 97 a potential observation of this rare process. We use the Full Run 2 dataset recorded by the ATLAS to search for
 98 the production of a top quark together with a W^\pm and Z boson in the channel with four leptons (two originating
 99 from the decay of the Z boson, one from the associated W boson and one from the W boson which decays from
 100 the top quark (together with a b quark)). In this analysis, we use a kinematic reconstruction technique which aims
 101 to discriminate between tWZ and our most prominent background process, $t\bar{t}Z$. In addition to this, we implement
 102 Machine Learning techniques (Boosted Decision Trees) to further isolate our tWZ signal. The dominant source of
 103 the fake lepton background is from $t\bar{t}Z$ events containing at least one fake lepton. The kinematic distributions of
 104 this background are taken from simulation and its normalisation is constrained using a dedicated control region. As
 105 this work forms the basis of an official ATLAS analysis, only blinded results are shown. A maximum likelihood fit
 106 (blinded) is performed over our two tWZ signal regions and three control regions, measure the cross section of tWZ
 107 in the tetralepton channel. In order to increase the sensitivity of our tWZ signal, we perform another maximum
 108 likelihood fit (blinded) over all regions defined for the tetralepton channel and the trilepton channel¹.

¹an independent analysis conducted by Benjamin Warren (University of Cape Town) [66]

109

Chapter 2

110

Theory

2.1 Standard Model of Particle Physics

112 The Standard Model (SM) is a Quantum Field Theory (QFT) which classifies all known elementary particles and
 113 describes their interactions. It is a well-tested model and has shown to be hugely successful in describing experi-
 114 mental data to great precision. It incorporates three of the four fundamental forces of nature: the electromagnetic,
 115 the weak and the strong forces. In Figure 2.1, all known elementary particles described by the SM, are shown.

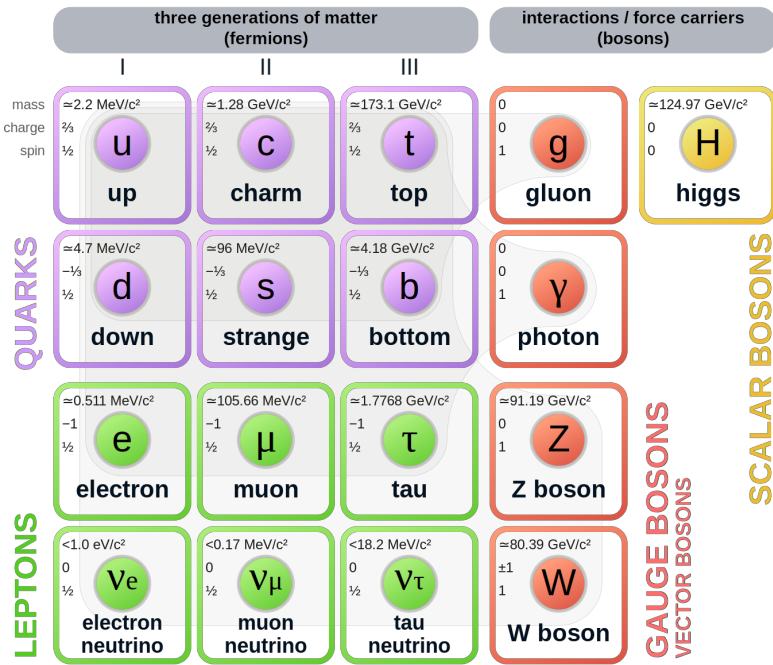


Figure 2.1: A summary of the elementary particles described by the SM [53] is shown. Fermions are shown on the left, with quarks shown in purple and leptons shown in green. Bosons are shown on the right, with gauge bosons shown in red and the Higgs boson shown in yellow. The mass, electric charge and spin of each particle is shown on the top left of each particle's block.

116 SM particles are uniquely described by their quantum numbers: mass, electric charge and spin. The SM particles
 117 are split into main two classes, based off their spin quantum numbers. Particles which have half-integer spin are
 118 called fermions, and those which have integer spin are called bosons. Fermions are further divided into three gener-
 119 ations, each comprising of two quarks, one charged lepton and one neutrino. The particles of each generation have
 120 identical electric charge and spin, but their masses differ. The masses of the particles in a generation increase with
 121 increasing generation number, with generation 1 particles being the least massive and generation 3 particles being
 122 the most massive. Quarks carry electric and colour charge, and can therefore interact via the electromagnetic, weak

and strong forces. Colour charge can take on three values: red, green and blue. Due to colour confinement [67], quarks cannot be isolated from one another. They exist in colourless bound states, called hadrons, consisting of two or more quarks. Hadrons consisting of an even number of quarks are known as mesons and those consisting of an odd number of quarks are known as baryons. On the other hand, charged leptons (electron (e), muon (μ) and tau (τ)) only carry electric charge and can therefore interact electromagnetically and weakly, but not through the strong interaction. The electric and colour neutral fermions, neutrinos, can only interact via the weak force.

Particles are able to interact with one-another via the exchange of a gauge boson (boson with spin-1). Photons are massless, spin-1 gauge bosons which mediate electromagnetic interactions between particles which carry electric charge, such as quarks and charged leptons (e , μ and τ). The weak interaction is mediated by three massive gauge bosons, the electrically charged W^+ and W^- bosons and the electrically neutral Z boson. Gluons are massless, spin-1 gauge bosons which mediate strong interactions between particles which carry colour charge, such as quarks. Since gluons carry colour charge, they interact with themselves.

The massive, spin-0, electrically neutral Higgs boson mediates the Higgs field which gives mass to the W^\pm and Z bosons via the so-called Brout-Englert-Higgs mechanism [36, 43, 42]. The Brout-Englert-Higgs mechanism induces spontaneous electroweak symmetry breaking to provide mass terms for the W^\pm and Z bosons in the electroweak Lagrangian of the SM.

All particles described in the SM have their own antiparticle, with the same mass, but opposite charges. Some particles, such as the photon, are their own antiparticle.

Although the SM has shown to be hugely successful, it is incomplete and fails to describe certain observed phenomena. The most notable example being the absence of gravity from the SM. The gravitational force is $\approx 10^{24}$ weaker than the weak force, therefore quantum gravitational effects are expected to only become significant at energies much larger than that currently accessible by the LHC (known as the Planck scale $\approx 10^9$ GeV) [46]. This large difference in strength between the weak force and gravity is known as the Hierarchy Problem. Cosmological observations infer that around 84% of the matter in the universe consists of gravitationally interacting matter known as dark matter. None of the particles described in the SM are good dark matter candidates, therefore the SM only accounts for a small fraction of the total matter of the universe. The large discrepancy between the observed amount of matter and antimatter in the universe, sometimes referred to as the matter-antimatter asymmetry, is unable to be fully explained by the SM. Neutrinos in the SM are assumed to be massless, however observations of neutrino oscillations (neutrinos undergoing flavour change as they travel through space) imply that neutrinos do have mass [38]. Beyond the Standard Model (BSM) theories attempt to explain the phenomena which the SM cannot. For example, a popular extension to the SM, Supersymmetry (SUSY) introduces new particles to the SM which are counterparts to the existing SM particles with the same quantum numbers, except for their spins. SUSY provides elegant explanations to many shortcomings of the SM, however none of the supersymmetric particles described by SUSY have been observed experimentally.

2.1.1 The Top Quark

The top quark is the heaviest particle in the SM, with a mass of 172.76 ± 0.30 GeV [41]. Since the coupling to the Higgs boson is proportional to the the mass of the interacting particle, the top quark is strongly coupled to the Higgs boson. Physics processing involvng top quarks is therefore a theoretically well-motivated area to search for new physics, since it is the most likely particle to couple to new physics theories at the TeV scale. Its large mass also makes it highly unstable, with a mean lifetime of $\approx 0.5 \times 10^{-24}$ s [41]. The top quark's lifetime is shorter than that of the hadronisation process, and it therefore decays before hadronising. We therefore cannot measure the top quark directly, but indirectly via its decay products. Top quarks almost always decay to a W boson and a b -quark ($\frac{\Gamma(Wb)}{\Gamma(Wq(q=b,s,d))} = 0.957 \pm 0.034$ [41]). b -quarks are the second heaviest quark in the SM, however their lifetimes are still longer than the hadronisation time scale. In hadron collider experiments, b -quarks travel a short distance in the detector before hadronising to form jets. In Table 2.1, the dominant final state branching fractions of the top quark, are shown.

Hadronic final states are more than twice as likely than leptonic final states. Final state decays to different lepton flavours are roughly equally probable.

Top quark production can be placed into two main categories: pair production ($t\bar{t}$) and single-top production (t). In the LHC, top quarks are mainly produced in pairs via strong interactions in gluon-gluon fusion ($gg \rightarrow t\bar{t}$) or quark

Decay Mode	Branching Fraction ($\frac{\Gamma_i}{\Gamma}$)
$t \rightarrow Wb \rightarrow e\nu_e b$	$(11.10 \pm 0.30)\%$
$t \rightarrow Wb \rightarrow \mu\nu_\mu b$	$(11.40 \pm 0.20)\%$
$t \rightarrow Wb \rightarrow \tau\nu_\tau b$	$(10.70 \pm 0.50)\%$
$t \rightarrow Wb \rightarrow q\bar{q}b$	$(66.50 \pm 1.40)\%$

Table 2.1: The dominant final state branching fractions of the top quark [41] are shown.

annihilation ($q\bar{q} \rightarrow t\bar{t}$). Top quark production via gluon-gluon fusion is the dominating process, since gluons are the most dominant particles produced in pp collisions in the LHC. The production cross section for $t\bar{t}$ (leptonic final state) in pp collisions with $\sqrt{s} = 13$ TeV was measured by ATLAS with a value of $830 \pm 0.4(\text{stat}) \pm 36(\text{syst}) \pm 14(\text{lumi})$ pb [4], with good agreement between measurement and theoretical prediction.

The most abundant mechanisms leading to single top production include, those involving the exchange of a W boson and those involving the production of a top quark in association with a W boson. In Table 2.2, single top production cross sections in pp collisions at $\sqrt{s} = 13$ TeV for various channels, are shown.

Process	Total Cross Section [pb]
$bq' \rightarrow W \rightarrow tq$	$216.99^{+9.04}_{-7.71}$
$qq' \rightarrow W \rightarrow \bar{b}t$	$10.32^{+0.40}_{-0.36}$
$bg \rightarrow b/t \rightarrow Wt$	71.7 ± 3.85

Table 2.2: Single top production cross sections in pp collisions at $\sqrt{s} = 13$ TeV for various channels [27] are shown. The prime superscript on q' indicates that the quark has a different flavour to q .

Single top production is suppressed compared to pair produced top production, with $t\bar{t}$ production (leptonic final state) being around three times as likely to occur than single top production across all decay channels.

2.2 tWZ

2.2.1 Tetralepton Channel

In Figure 2.2, the Leading Order (LO) Feynman diagram for tWZ in the tetralepton channel, is shown.

2.2.1.1 Backgrounds

The main backgrounds for tWZ (tetralepton channel) are the production of a two tops, both in the $\ell\nu b$ final state channel, together with a Z boson ($t\bar{t}Z$) and diboson production with fully leptonic final states (ZZ). In Figure 2.2.1.1, LO Feynman diagrams for $t\bar{t}Z$ and ZZ in the tetralepton channel, are shown.

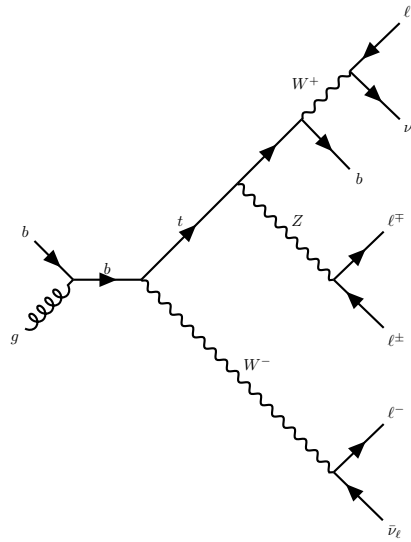


Figure 2.2: The LO Feynman diagram of tWZ production in the tetralepton channel is shown.

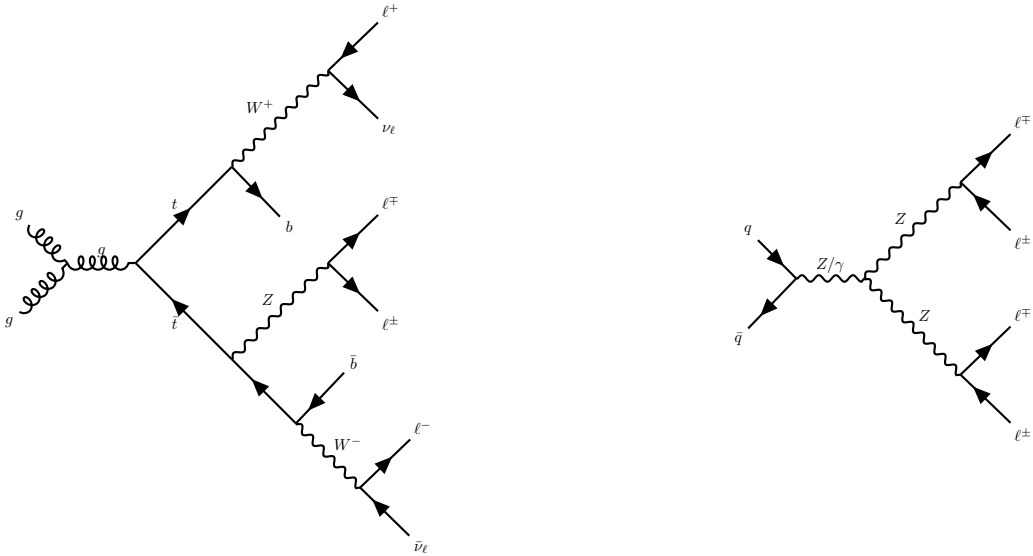


Figure 2.3: LO Feynman diagrams for $t\bar{t}Z$ (left) and ZZ (right) in the tetralepton channel are shown.

$t\bar{t}Z$ contains four leptons and two b -quarks in its final state (inclusive $\sigma(t\bar{t}Z) = 0.95 \pm 0.08_{\text{stat}} \pm 0.10_{\text{syst}}$ pb at $\sqrt{s} = 13$ TeV [2]) and can easily mimic the tWZ signal process, for instance, by one of its b -jets getting missed during detection. ZZ contains four leptons and zero b -quarks in its final state (inclusive $\sigma(ZZ) = 14.6^{+1.9}_{-1.8}(\text{stat})^{+0.5}_{-0.3}(\text{syst}) \pm 0.2(\text{theo}) \pm 0.4(\text{lumi})$ pb at $\sqrt{s} = 13$ TeV [47]). One way in which ZZ can mimic the tWZ signal process is by reconstruction of a non-prompt b -jet.

2.2.2 Comparison to Trilepton Channel

The most apparent difference between the tri and tetralepton channels is the amount of statistics present, with the tetralepton channel having far less events in its phase space than that of the tri-lepton channel. The lack of statistics in the tetralepton channel can be attributed to its low production cross section, $\sigma_{(tW^\pm Z).Br(4\ell)}^{\text{NLO}} = 0.7$ fb [23]. The tri-lepton channel has a production cross section ($\sigma_{(tW^\pm Z).Br(3\ell)}^{\text{NLO}} = 3.9$ fb [23]) around a factor of 4 larger than that of the tetralepton channel. This difference between the production cross section of the two decay channels can be largely attributed to the difference in branching ratios ($\frac{\Gamma_i}{\Gamma}$) between a hadronically decaying W

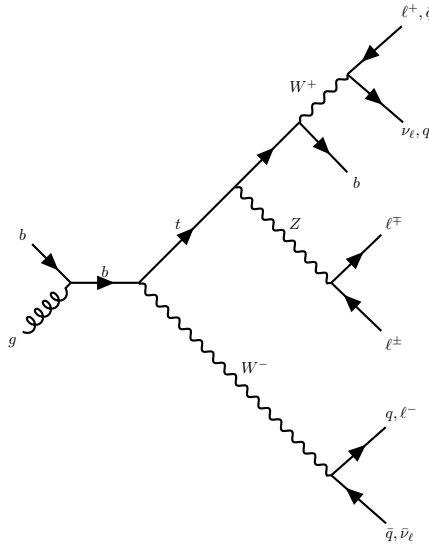


Figure 2.4: Example Feynman diagram of tWZ production in the tri-lepton channel.

208 boson, $\frac{\Gamma_{W \rightarrow had}}{\Gamma_W} = (67.41 \pm 0.27)\%$ [41], present in the tri-lepton channel and a leptonically decaying W boson,
 209 $\frac{\Gamma_{W \rightarrow \ell\nu}}{\Gamma_W} = (10.86 \pm 0.09)\%$ [41], present in the tetralepton channel.
 210

211 Despite the tetralepton channel's low statistics, it is not subject to the large WZ background present in the
 212 trilepton channel. The tetralepton channel has a relatively large ZZ background (not present in the trilepton
 213 channel), fortunately this can be easily suppressed due to the full reconstructability of the two leptonically decaying
 214 Z -bosons.

215 2.2.3 Motivation for the search for tWZ production in the tetralepton channel

216 The recent lack of signs of new physics from LHC data tells us that new physics is either very heavy, or is very
 217 weakly coupled to SM particles. We therefore might only observe signs of new physics in anomalous rates of
 218 well-chosen processes. tWZ is a prime example of such a process. It has an extremely low production cross section
 219 (0.7 fb for $\sqrt{s} = 13$ TeV [23]), and has subsequently never been observed by any particle physics experiment. Since
 220 tWZ involves a charged W boson and neutral Z boson, its cross section is sensitive to the charged and neutral
 221 couplings to the top quark. In turn, the top quark is strongly coupled to the Higgs boson, due to its large mass.
 222 In the SM Lagrangian, the top quark causes the Higgs boson mass to diverge to the Planck scale. Many BSM
 223 theories aim to get rid of this Higgs mass divergence to the Planck scale. tWZ is therefore an important process
 224 in the search for signs of new physics and BSM physics.
 225

226 Standard Model Effective Field Theory (SMEFT) is such a BSM theory which is sensitive to tWZ production.
 227 SMEFT attempts to describe physics at large energy scales which we have not yet been able to probe experimen-
 228 tally. SMEFT inherits the same QFT framework as the SM, and adds Lagrangian terms to the SM Lagrangian
 229 which describe the interactions of SM particles at higher energy scales. Analogous to the coupling constants
 230 found in the SM Lagrangian, which indicate the interaction strengths between different particles, SMEFT contains
 231 scalars which operate in the same way. These scalar coefficients are known as Wilson coefficients. It has been
 232 shown that the cross section of tWZ is sensitive to many Wilson coefficients. An experimental constraint on
 233 the cross section of tWZ is therefore expected to be impactful on a global fit on all the Wilson coefficients in SMEFT.
 234

235 Prior to this analysis, only two experimental studies of tWZ in ATLAS have been done. Both take advantage of
 236 trilepton channel to search for tWZ production. The first search utilised, 36 fb^{-1} of ATLAS data and an upper
 237 limit on the cross section of tWZ was set at a value of ≈ 6 times the SM cross section [56]. The second search
 238 utilised 139 fb^{-1} (Full Run 2) of ATLAS data and an expected upper limit on the cross section of tWZ was set at
 239 a value of ≈ 2.6 times the SM cross section [66]. In Section 4.11.2, the latter analysis will be used in combination
 240 with this analysis, in order to further increase the sensitivity of tWZ .

241

Chapter 3

242

The ATLAS Experiment and Detector

243

3.1 The ATLAS Experiment

244 ATLAS (A Toroidal LHC ApparatuS) is one of two general purpose detectors at CERN (the European Organization
 245 for Nuclear Research) near Geneva in Switzerland. These detectors collect data from the collisions
 246 provided by the worlds highest energy particle accelerator [24], the Large Hadron Collider (LHC) situated at CERN.

247

248 In this section, information about the LHC and the ATLAS detector are given. This includes technical aspects of
 249 the ATLAS detector and the processing of data into meaningful physics objects to be used in analyses.

250

3.1.1 Large Hadron Collider (LHC)

251 The LHC is a circular 27 km particle accelerator located in an underground tunnel on the border between France and
 252 Switzerland. The accelerator consists of supercooled, superconducting magnets which accelerate and collide beams
 253 of protons at centre-of-mass energies up to $\sqrt{s} = 13$ TeV at instantaneous luminosities of $\mathcal{L} \sim 10^{34}$ cm $^{-2}$ s $^{-1}$. The
 254 LHC mainly produces these pp collisions, however heavy-ion collisions can be produced (typically lasting a month,
 255 annually) which reach centre-of-mass energies of $\sqrt{s} = 5.02$ TeV/nucleon at instantaneous luminosities of $\mathcal{L} \sim 10^{27}$
 256 cm $^{-2}$ s $^{-1}$. pp beams consist of bunches of protons which collide every 25 ns, corresponding to a frequency of 40 MHz.

257

258 Several accelerator systems are used to accelerate protons and heavy ions to such high energies. Protons are
 259 extracted from a tank of ionised hydrogen gas and are injected into the Linear Accelerator 2 (LINAC), where
 260 they are linearly accelerated to momenta of 50 MeV. The proton bunches are then sequentially accelerated
 261 by a chain of circular accelerators. The chain starts with the Booster which accelerates the protons to mo-
 262 mента of up to 1.4 GeV. The proton bunches are then fed through to the Proton Synchrotron (PS) and the
 263 Super Proton Synchrotron (SPS) which accelerate the protons to momenta of up to 25 GeV and 450 GeV
 264 respectively. The protons are then transferred to two beam pipes of the LHC where they travel in opposite
 265 directions. Both proton beams are accelerated to their final momenta of 6.5 TeV, resulting in a centre-of-mass
 266 energy of 13 TeV. These proton beams then collide at one of the four main interaction points situated along the LHC.

267

268 The four main experiments located at the interaction points are ATLAS, the Compact Muon Solenoid (CMS),
 269 Large Hadron Collider Beauty (LHCb) Experiment and A Large Ion Collider Experiment (ALICE). ATLAS
 270 and CMS are general-purpose detectors which investigate a wide range of physics processes. Since both
 271 ATLAS and CMS can measure the same processes, they are able to cross-check and validate measurements
 272 taken by one another. LHCb is specifically designed to study decays of particles containing b -quarks. ALICE
 273 is designed to study the strongly interacting quark-gluon plasma which is formed at extremely high energy densities.

274

275 At the interaction points, the two proton beams which consist of protons in closely packed bunches, travel in
 276 opposite directions to one another and collide. We are only able to study one pp collision (event) at a time, however
 277 many hard pp collisions can occur per bunch crossing. These additional collisions are referred to as *pile-up*. Pileup
 278 complicates the reconstruction of the particles originating from the hard collision of interest.

279 **3.1.1.1 Luminosity**

280 The event production rate at the LHC, $R(t)$, for a certain process of interest is given by,

$$R(t) = \mathcal{L}(t)\sigma \quad (3.1)$$

281 where $\mathcal{L}(t)$ is the instantaneous luminosity and σ and is the cross section of the process of interest. The instantaneous
282 luminosity, $\mathcal{L}(t)$, is independent on the process of interest, and depends on various collider and beam parameters.
283 $\mathcal{L}(t)$ can be written in terms of these parameters as,

$$\mathcal{L}(t) = f \frac{N n_1 n_2}{4\pi \sigma_x \sigma_y} \quad (3.2)$$

284 where f is the beam revolution frequency, N is the number of proton bunches colliding per second, n_1 and n_2 are the
285 number of protons in the colliding bunches, σ_x and σ_y are the beam spread in the x and y directions respectively.
286 The total integrated luminosity, L , across some time interval, is given by,

$$L = \int \mathcal{L} dt. \quad (3.3)$$

287 The units of L are inverse area, and are given by fb^{-1} at the LHC and the ATLAS detector.

288 In Figure 3.1, the total integrated luminosity delivered to ATLAS, recorded by ATLAS, and certified to be good
289 enough for physics analyses (the data passes certain quality control criteria) for $\sqrt{s} = 13$ TeV pp collisions at the
290 LHC is shown [63].

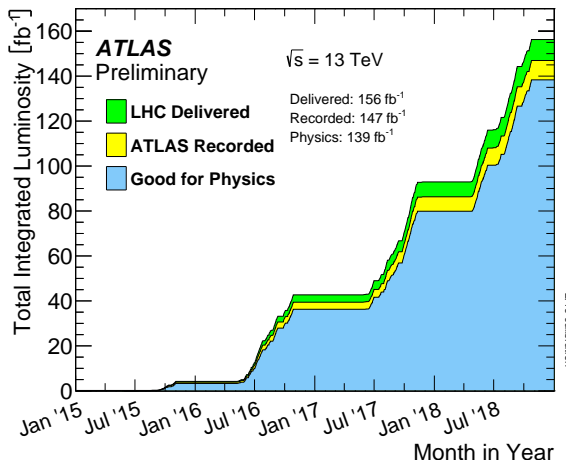


Figure 3.1: The total integrated luminosity delivered to ATLAS, recorded by ATLAS, and certified to be good enough for physics analyses (the data passes certain quality control criteria) for $\sqrt{s} = 13$ TeV pp collisions at the LHC is shown [63]. The total integrated luminosity delivered by the LHC, recorded by ATLAS and certified to be good quality data are shown by the green, yellow and blue histograms respectively. The month and year of data taking is shown on the x-axis and the total integrated luminosity (in fb^{-1}) is shown on the y-axis.

292 A total integrated luminosity of 139 fb^{-1} of data certified as good for physics was recorded by ATLAS between
293 2015 and 2018. This data taking period is referred to as Run 2, since it proceeds the Run 1 data taking period
294 (2011 and 2012) and the Long Shutdown 1 LHC upgrade period (2013 and 2014). In this analysis, we use the Full
295 Run 2 dataset.

296 **3.2 The ATLAS Detector**

297 The ATLAS detector is a general purpose particle detector, located at one of the four interaction points along the
298 LHC beam pipe (100 m below ground). In Figure 3.2, the schematic of the ATLAS detector, is shown.
299 The detector is cylindrically shaped which covers close to 4π in solid angle. It has a length of 44 m, a diameter of
300 25 m and a mass of 7000 tons. ATLAS consists of four main sub-detectors arranged in concentric cylindrical layers

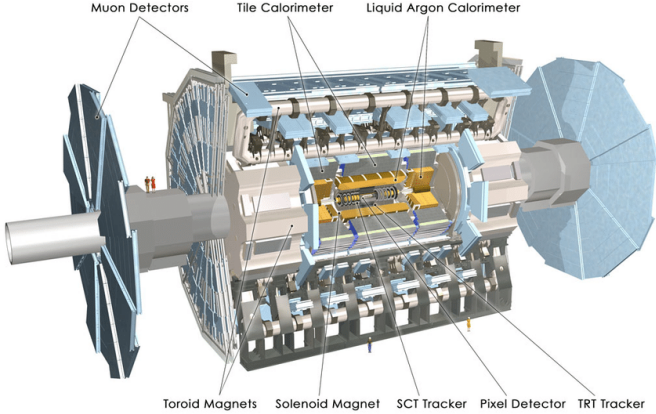


Figure 3.2: Schematic of the ATLAS detector [31]

301 around the beam pipe. These include the inner detector, the electromagnetic calorimeter, the hadronic calorimeters
 302 and the muon spectrometer. The sub-detectors record the momenta, energies and trajectories of different particles
 303 produced in the collider, allowing for the reconstruction and identification of these particles to be used in physics
 304 analyses.

305 3.2.1 Coordinate System and Kinematics

306 The ATLAS detector adopts a right-handed coordinate system. The origin is at the nominal interaction point with
 307 the beam direction defining the z -axis. The $x - y$ plane (or transverse plane) is perpendicular to the beam line,
 308 with the x -axis pointing towards the centre of the LHC ring and the y -axis pointing upwards towards the Earth's
 309 surface. The azimuthal angle, $\phi \in [-\pi, \pi]$, is measured in the transverse plane with respect to the positive x -axis.
 310 The polar angle, $\theta \in [0, \pi]$, is measured in the $z - y$ plane with respect to the positive y -axis. A quantity called
 311 the pseudorapidity, $\eta \in [0, \infty]$ is defined as,

$$\eta = -\ln \tan \left(\frac{\theta}{2} \right) \quad (3.4)$$

312 η is often used as a measure of the polar angle, instead of θ , since the difference in η between two particles, $\Delta\eta$, is
 313 invariant under a Lorentz boost in the z -direction. The angular distance between two physics objects, ΔR , can be
 314 written as,

$$\Delta R = \sqrt{(\Delta\phi)^2 + (\Delta\eta)^2} \quad (3.5)$$

315 where $\Delta\phi$ is the difference in ϕ between the two physics objects of interest. Quantities defined in the transverse
 316 plane are often used to describe the kinematics of physics objects in hadron collider experiments. The transverse
 317 momentum, p_T , is defined as,

$$p_T = \sqrt{(p_x)^2 + (p_y)^2} \quad (3.6)$$

318 where p_x and p_y are the x and y components of the physics object's momenta, respectively. The transverse energy,
 319 E_T , is defined as,

$$E_T = \sqrt{m^2 + p_T^2} \quad (3.7)$$

320 where m is the invariant mass of the physics object.

321 3.2.2 Inner Detector

322 The inner detector is the first layer of concentric cylindrical sub-detector layers in the ATLAS detector. It is used
 323 to identify charged particles and reconstruct the trajectories of charged particles produced in the collisions via
 324 energy deposition in semiconductor material (hits) and the ionisation of gas. It consists of three complementary
 325 sub-detectors (in order from nearest to farthest from the beam pipe): the Pixel Detector, the Semiconductor Tracker
 326 (SCT) and the Transition Radiation Detector (TRT). The Pixel Detector and SCT are based on semiconductor

327 technology and have the highest granularity of any sub-detector in ATLAS, in order to cope with the high frequency
 328 of collisions near the interaction point. The TRT consists of drift tubes (straws) containing a mixture of gas (70%
 329 Xe, 27% CO₂ and 3% O₂), which allows measurement of the energy deposited by charged particles through the
 330 ionisation of the gas. Solenoid magnets surround the inner detector and bend the trajectories of charged particles.
 331 The charges and momenta of particles can be inferred from their bent trajectories, which are reconstructed by the
 332 hits produced via energy deposition in the Inner Detector.

333 3.2.3 Electromagnetic and Hadronic Calorimeters

334 The Electromagnetic Calorimeter (ECAL) and Hadronic Calorimeter (HCAL) surround the Inner Detector, with
 335 the ECAL nearer to the beam line. The ECAL and HCAL provide accurate measurements of the energy of particles
 336 which interact electromagnetically (e.g. photons and electrons) and hadronically (e.g. jets), respectively. Particles
 337 entering the calorimeters interact with the detector material and create either a electromagnetic shower (in the
 338 ECAL) or a hadronic shower (in the HCAL), depositing all their energy in the calorimeter cells. The calorimeters
 339 consist of an active material and a passive absorber material. Active materials are used to measure the energy
 340 deposited by the particles and passive absorber materials induce the electromagnetic and hadronic showers. The
 341 ECAL uses liquid argon (LAr) as its active material and lead as its absorber material. The HCAL uses alternating
 342 steel absorber layers and plastic scintillating tile layers as its active material. The primary mechanism of energy
 343 deposition in the ECAL is through bremsstrahlung (for electrons) and pair production (photons). Hadrons usually
 344 deposit a small amount of their energy in the ECAL, and interact via inelastic scattering with the nuclei of the
 345 detector material. The hadronic showers (jets) produced in these nuclear interactions travel much further than an
 346 electromagnetic shower, and for that reason, the volume of the is designed HCAL occupies a much larger space
 347 than that of the ECAL.

348 3.2.4 Muon Spectrometer

349 The Muon Spectrometer (MS) is the outermost sub-detector of ATLAS and surrounds the HCAL. Muons traverse
 350 through the inner detector and calorimeters, with minimal energy loss, before reaching the MS. The MS consists
 351 of trigger and high-precision tracking systems. Large superconducting toroid shaped magnets deflect the incoming
 352 muons to measure their trajectories and subsequently their momenta via the curvature of the trajectories. The MS
 353 measures muon trajectories as they ionize gas (filled with Ar and CO₂ gas) in the MS drift chambers.

354 3.2.5 Trigger and Data Acquisition System

355 The Trigger and Data Acquisition System (TDAQ) manages and handles the large amount of data produced within
 356 the ATLAS detector. In Run 2, pp bunch crossings occur every 25 ns, corresponding to an event rate of 40 MHz [31].
 357 The TDAQ system performs a fast preliminary reconstruction to select events with signatures which are interesting
 358 for physics analyses. The information collected from these events are permanently stored for offline reconstruction
 359 and analysis, and the rest (the vast majority of events) are discarded. The trigger system reduces the 40 MHz data
 360 rate to around 1 kHz [31].

361 3.2.6 Particle Identification and Object Reconstruction

362 Particles originating from pp collisions, or from their subsequent decays, traverse through the ATLAS detector and
 363 interact with its different sub-detectors, producing characteristic electronic signals. These signals are then processed
 364 by various algorithms to reconstruct and identify the physics objects (e.g. electrons, muons, jets) in the event. This
 365 section outlines the procedures used to define these physics objects.

366 3.2.6.1 Tracks and primary vertices

367 The trajectories of charged particles, or tracks, are reconstructed in the ID. First, energy is deposited by charged
 368 particles (hits) in pixels or strips, in the Pixel and SCT detectors respectively. Adjacent pixels or strips are grouped
 369 together in *energy clusters*. Energy clusters define 3D space-points indicating the location where the charged
 370 particle traversed. Track seeds are then defined as sets of three space-points, in either the Pixel or SCT detectors.
 371 A Kalman filter [9] is then used to build track candidates from the track seeds. Often, multiple track candidates
 372 are built per track seed, therefore an ambiguity solver is needed for finding the track which best represents the
 373 traversal of the charged particle. The ambiguity solver ranks each track from a given seed based on, the number of

374 associated hits, the number of holes (expected hits which are absent), track momenta and the χ^2 of the track fit.
375 Low ranked tracks are then discarded. High ranked tracks are refitted, introducing information from the TRT.

376

377 The primary vertex is the location of the pp collision of interest (i.e. from the hard scatter). The primary vertex
378 from the hard scatter needs to be identified, to isolate the event of interest from unwanted pile-up events. In the
379 event reconstruction procedure, the primary vertex is defined as the vertex of the event with the largest sum of
380 (p_T)² (corresponding to the measured (p_T)² of the particle from its reconstructed track) of its associated tracks.
381 Furthermore, the primary vertex is required to have at least two associated tracks. To reduce contamination from
382 fake tracks used in primary vertex reconstruction, only tracks which pass certain tight selection criteria [52] are used
383 in the reconstruction procedure. An iterative fitting procedure [52] is then used to reconstruct the primary vertex.
384 The best vertex position is fitted from the reconstructed tracks and a selected seed position. In each iteration, the
385 less compatible tracks are down-weighted and the next best vertex position is recomputed. All incompatible tracks
386 are then removed and the fitting procedure is repeated until all tracks have a corresponding vertex or no additional
387 vertices can be found with the remaining set of tracks.

388 3.2.6.2 Electrons

389 Since electrons are charged particles, they give rise to tracks in the Inner Detector and deposit energy in the
390 ECAL via electromagnetic showering. Electrons are therefore reconstructed and identified from signals in the
391 Inner Detector and ECAL. Electrons are reconstructed using a dynamic clustering algorithm [1] which matches
392 electron candidate tracks in the Inner Detector to energy clusters in the ECAL. First, energy clusters which
393 have local maxima are identified using a sliding window algorithm [6]. Tracks are then matched to the energy
394 clusters, forming electron candidates for each energy cluster. Often, many electron candidates are found. Electron
395 candidates are ranked based on the ΔR between the track and energy cluster, and the number of Pixel Detector
396 hits and holes. The electron candidate with the highest rank is chosen as the electron track.

397

398 A likelihood discriminant is used to identify electrons. Quantities measured in the Inner Detector and ECAL
399 are used as input, such that they discriminate well between prompt isolated electrons and other physics objects
400 (e.g. jets, electron from a photon conversion, electron from a semi-leptonically decaying hadron). Important input
401 variables include the shape of the electromagnetic shower, track quality in the Inner Detector and information from
402 the TRT. Three working points (*loose*, *medium*, *tight*) are defined, based on different cuts on the output of the
403 likelihood discriminant. The *loose* working point has the weakest background rejection power (higher efficiency),
404 whereas the *tight* working point has the strongest background rejection power (lower efficiency).

405 3.2.6.3 Muons

406 Muons leave tracks in the Inner Detector and the MS. They traverse the ECAL and HCAL with no significant
407 energy loss. Muons are therefore reconstructed and identified from information in the Inner Detector and MS.
408 Tracks are reconstructed in the Inner Detector and MS independently. Both tracks are combined, using a global
409 χ^2 fit, resulting in reconstructed muon candidates.

410

411 Similar to electron identification, muons use a likelihood discriminant to identify prompt muons and suppress
412 background contamination (mainly from pion and kaon decays). Four working points are defined to cover needs of
413 different physics analyses: *loose*, *medium*, *tight* and *high- p_T* [5].

414 3.2.6.4 Jets and b -tagging

415 Due to colour confinement, free quarks and gluons cannot exist. Therefore, coloured particles emerging from the
416 interaction point result in collimated streams of colourless particles, known as jets. Jets deposit energy in the
417 Inner Detector and in the HCAL. Jets in ATLAS are reconstructed from topological clusters using the anti- k_t
418 algorithm [25]. Topological clusters are groups of adjacent calorimeter cells which originate from *seed* cells. Seed
419 cells are defined to contain at least 4 times the average amount of noise expected in the cell¹. All cells adjacent to
420 the seed cell are grouped together given that the energy deposited within the cell is at least 2σ . This process is
421 repeated until there are no adjacent cells which meet the above criteria. All adjacent cells to the cluster are then
422 added, with no requirement on the energy deposited within these cells.

423

¹ σ : average noise in a given cell

424 Different tagging algorithms are used to identify the quark flavour which initiated a jet. b -quark tagging is used
 425 extensively in top physics, due to the b -quark present in the top quark's dominant decay channel (See Table 2.1).
 426 Hadrons arising from b -quark hadronisation have mean lifetimes ~ 1.5 ps and travel (on average) a few mil-
 427 limetres before decaying. This creates a secondary vertex within the jet (See Figure 3.3). This characteristic decay
 428 signature, along with several other unique features of b -jets, are exploited in b -tagging algorithms to distinguish
 429 b -jets from c - or light flavour jets. In Figure 3.3, an illustration of the production of a b -jet, is shown.

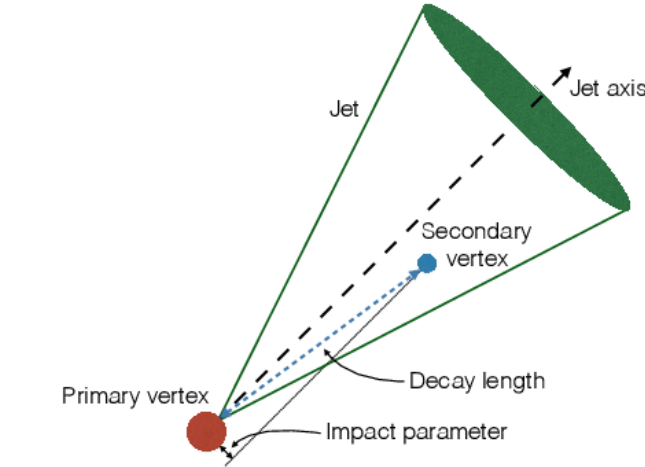


Figure 3.3: An illustration [32] of the production of a b -jet is shown. This illustrates the presence of a secondary vertex within a b -jet.

430 In this analysis, we use the recommended DL1r (Deep-Learning Flavour Tagger) tagging algorithm [17]. The DL1r
 431 algorithm combines outputs from several low-level tagging algorithms using a Deep Neural Network and outputs
 432 the probability that a given input jet is identified as a b , c or light flavoured jet.

433

Chapter 4

434

Analysis Setup and Strategy

435 4.1 Data and Monte Carlo Simulation

436 4.1.1 Data Samples

437 The pp collision data used in this analysis was collected with the ATLAS detector at the LHC from 2015 to 2018. This
 438 data period of data taking is referred to as Run 2. During this period, pp collisions at $\sqrt{s} = 13$ TeV, corresponding
 439 to an integrated luminosity (\mathcal{L}) of 156 fb^{-1} , were delivered by the LHC. The ATLAS detector managed to record
 440 147 fb^{-1} of this total delivered data. 139 fb^{-1} of the data recorded by ATLAS is considered to be good enough for
 441 physics analyses (the data passes certain quality control criteria) and placed into the *Good Runs List* [40]. We use
 442 the Run 2 datasets from the Good Runs List, called `mc16a`, `mc16d` and `mc16e` with integrated luminosity's of 36.2 fb^{-1} ,
 443 44.3 fb^{-1} and 58.5 fb^{-1} respectively.

444 4.1.2 Monte Carlo Samples

445 Simulated Monte Carlo (MC) samples were generated and used to model the SM tWZ signal and its backgrounds.
 446

447 The following background processes are considered:

- 448 • **$t\bar{t}Z$** : $t\bar{t}$ with an associated Z -boson, in the tetralepton final state. Therefore, both top-quarks decay leptonically
 449 (e.g. $t \rightarrow W^+ b \rightarrow \ell^+ \nu b$) and of these top-quarks emits a Z -boson which decays leptonically ($Z \rightarrow \ell^\pm \ell^\mp$
 450 (OSSF lepton pair)). This results in a final state with 4 leptons and 2 b-quarks.
- 451 • **ZZ** : Diboson production with a tetralepton final state, therefore both Z -bosons decay leptonically ($Z \rightarrow \ell^\pm \ell^\mp$
 452 (OSSF lepton pair)).
- 453 • **other**: Processes with a relatively minimal, but non-negligible background contribution

- 454 - $VVV (V = W/Z)$
- 455 - $t\bar{t}$
- 456 - $t\bar{t}W$
- 457 - $t\bar{t}WW$
- 458 - $t\bar{t}H$
- 459 - WZ
- 460 - $t\bar{t}t$
- 461 - $t\bar{t}t\bar{t}$
- 462 - tZq

463 The MC simulations are achieved via the use of event generators and parton shower generators. Event generators
 464 simulate the pp collisions (hard events) by sampling the proton's Parton Distribution Functions (PDFs) at the
 465 desired energy scale. The parton shower generators simulate any incoming or outgoing particles from the hard
 466 process, which carry QCD color charge and can therefore lead to parton showers.

467

468 The production of tWZ events is simulated with the `MADGRAPH5_AMC@NLO 2.3.3` generator providing matrix
 469 element (ME) calculations at NLO. The events are interfaced with `PYTHIA 8.235` for the parton shower.

470

471 The production of $t\bar{t}Z$ and $t\bar{t}W$ events are simulated with the `MADGRAPH5_AMC@NLO 2.3.3` generator providing ME
 472 calculations at NLO. The events are interfaced with `PYTHIA 8.210` for the parton shower.

473

474 Event generation of tWZ and $t\bar{t}Z$ results in diagrams which overlap with one another, that is, these diagrams
 475 contain the same initial and final state particles. Several methods exist in order to separate between the two
 476 processes, by removing the overlap, therefore avoiding double counting. There are two different diagram removal
 477 procedures, diagram removal procedure 1 (DR1) [34] and diagram removal procedure 2. We use the DR1 scheme
 478 to remove the overlap (interference) between tWZ and $t\bar{t}Z$.

479

480 Diboson processes which feature the three charged leptons and one neutrino or four charged lepton in their final
 481 states, such as WZ and ZZ , are simulated using `SHERPA 2.2.2` at NLO precision. The events are interfaced with
 482 `SHERPA` for the parton shower.

483

484 Fully leptonic triboson processes such as WWW , WWZ , WZZ , and ZZZ containing up to six leptons in their
 485 final states are simulated using `SHERPA 2.2.2` at NLO precision. The events are interfaced with `SHERPA` for the
 486 parton shower.

487

488 The production of $t\bar{t}$ events are simulated with the `POWHEG` generator providing ME calculations at NLO. The
 489 events are interfaced with `PYTHIA 8.210` for the parton shower.

490

491 The production of $t\bar{t}t$, $t\bar{t}\bar{t}$ and $t\bar{t}WW$ are simulated using the `MADGRAPH5_AMC@NLO 2.2.2` generator at LO
 492 precision. The events are interfaced with `PYTHIA 8.186` for the parton shower.

493

494 The production of $t\bar{t}$ with an associated Higgs boson, $t\bar{t}H$, are generated using the `MADGRAPH5_AMC@NLO 2.6.0`
 495 generator at NLO precision. The events are showered using `PYTHIA 8.230`.

496

497 The production of $t\bar{t}$ events is simulated with the `POWHEG` generator providing ME calcualtions at NLO. The events
 498 are showered using `PYTHIA 8.230`.

499

500 The production of a single top quark in association with a Z -boson and an extra parton, tZq , is simulated using
 501 `MADGRAPH5_AMC@NLO 2.3.3` at NLO prescision. The events are interfaced with `PYTHIA 8.230` for the parton shower.

502

503 In Table 4.1, the event generator and parton shower used for each process's sample are shown.

Process	Event Generator	Cross section calculation	Parton Shower
tWZ	<code>MADGRAPH5_AMC@NLO 2.3.3</code>	NLO	<code>PYTHIA 8.235</code>
$t\bar{t}Z$	<code>MADGRAPH5_AMC@NLO 2.3.3</code>	NLO	<code>PYTHIA 8.210</code>
ZZ, WZ	<code>SHERPA 2.2.2</code>	NLO	<code>SHERPA</code>
$VVV (V = W/Z)$	<code>SHERPA 2.2.2</code>	NLO	<code>SHERPA</code>
$t\bar{t}$	<code>POWHEG</code>	NLO	<code>PYTHIA 8.230</code>
$t\bar{t}W$	<code>MADGRAPH5_AMC@NLO 2.3.3</code>	NLO	<code>PYTHIA 8.210</code>
$t\bar{t}WW$	<code>MADGRAPH5_AMC@NLO 2.2.2</code>	LO	<code>PYTHIA 8.186</code>
$t\bar{t}H$	<code>MADGRAPH5_AMC@NLO 2.6.0</code>	NLO	<code>PYTHIA 8.230</code>
$t\bar{t}t, t\bar{t}\bar{t}$	<code>MADGRAPH5_AMC@NLO 2.2.2</code>	LO	<code>PYTHIA 8.186</code>
tZq	<code>MADGRAPH5_AMC@NLO 2.3.3</code>	NLO	<code>PYTHIA 8.230</code>

Table 4.1: The event generator and parton shower used for the signal and background process's MC samples is shown.

504 4.2 Objects

505 In this section the physics objects (leptons, jets and b -tagged jets) used in this analysis are outlined.

506 4.2.1 Leptons

507 In this analysis we only consider e and μ leptons, since τ leptons are difficult to detect in the ATLAS detector.
 508 τ leptons are challenging to detect since they have an extremely short lifetime (290.3 ± 0.5 fs [41]) which causes
 509 them to decay before reaching any detector components and therefore can only be reconstructed via their decay
 510 products.

511 In addition to our selection criteria of exactly four leptons, we require that the Leading (L), Next-to-Leading (NL),
 512 Next-to-Next-to-Leading (NNL) and Next-to-Next-to-Next-to-Leading (NNNL) leptons have p_T greater than 28,
 513 18, 10 and 10 GeV respectively. Here we have chosen to apply relatively loose object-level cuts in an attempt to
 514 maximize our signal statistics, since the analysis is heavily statistically limited.

515
 516 Reconstructed electrons are required to be within $|\eta| < 2.47$ and excluding the transition region between the barrel
 517 and end-cap calorimeters at $1.37 < |\eta| < 1.52$. Reconstructed muons are required to be within $|\eta| < 2.5$.

518
 519 The transverse impact parameter, d_0 , is defined as the minimal spacial distance between the object's (here we
 520 are referring to leptons) trajectory and the primary vertex (the vertex associated with the p - p hard scatter).
 521 The longitudinal impact parameter, z_0 , is defined as the value of z of the point on the object's trajectory which
 522 determines d_0 . To ensure consistency between the lepton and the primary vertex, we require that $|\frac{d_0}{\sigma(d_0)}| < 5$,
 523 $|z_0 \sin \theta| < 0.5$ mm for electrons and $|\frac{d_0}{\sigma(d_0)}| < 3$, $|z_0 \sin \theta| < 0.5$ mm for muons, following the current recommenda-
 524 tions [62].

525
 526 To avoid instances where one detector signal can result in multiple different reconstructed objects, an overlap
 527 removal is applied which ignores all but one of these objects. We use the current recommended configuration [39].

528
 529 Electrons are selected using a likelihood based discriminant [1] which takes measurements from the tracking
 530 system, calorimeter system and quantities derived from both the tracking and calorimeter system as input. Muons
 531 are selected using AnalysisBase's Muon Selection Tool [55].

532
 533 Loose electrons are defined with the criteria above, using the `LooseAndBLayerLH` ($\sim 91\%$ selection efficiency for
 534 electrons with $E_T > 30$ GeV [35]) identification working point. Similarly, tight electrons are defined with the
 535 criteria above, using the `TightLH` ($\sim 80\%$ selection efficiency for electrons with $E_T > 30$ GeV [35]) identification
 536 working point. Both loose and tight muons use the `Medium` ($\sim 95\%$ selection efficiency [5]) identification working
 537 point.

538
 539 Tight leptons additionally require that they are sufficiently isolated from other particles produced in the collision.
 540 This is done by defining a cone of radius $\Delta R = \sqrt{\Delta\eta^2 + \Delta\phi^2}$ around the particle of interest and summing the p_T
 541 of all the reconstructed particles surrounding the particle of interest, situated within the cone. A quantity, I_{rel} , is
 542 then defined as $I_{rel} = \frac{\sum p_T(\text{surrounding candidate})}{p_T(\text{candidate})}$, the ratio of this sum to the p_T of the lepton candidate. If this value
 543 is large, it is likely that the particle of interest originated from a jet (together with many other particles), whereas
 544 a prompt decay product resulting from the hard scatter will have little to no energy surrounding it ($I_{rel} \ll 1$).
 545 We use Analysis Base's `IsolationSelectionTool` with the `PLVTight` ($\sim 70\%$ efficiency [7]) and `PLVTight` (\sim
 546 70% efficiency at $p_T = 30$ GeV [29]) working points for tight electrons and tight muons respectively (following the
 547 current recommendations [59]).

548
 549 In Table 4.2, a summary of the selection criteria for leptons is shown.

551 4.2.2 Jets

552 Jets are reconstructed using the anti- k_t algorithm (See Section 3.2.6.4). We use the `AntiKt4EMPFflowjets` (\sim
 553 97% average efficiency with JVT (outlined in the subsequent paragraph) > 0.2 [62]) working point (following the
 554 current recommendations [62]).

555
 556 The jet-vertex-tagger (JVT) and the forward jet-vertex-tagger (fJVT) are likelihood discriminant which aim
 557 to suppress pile-up jets. We use the `Medium` working point for the JVT and the fJVT (following the current
 558 recommendations [58]). We additionally require that jets have a JVT value greater than 0.5.

	Electrons		Muons	
	Tight	Loose	Tight	Loose
p_T cuts	$p_T(\ell_1, \ell_2, \ell_3, \ell_4) > (28, 18, 10, 10)$ GeV "recommended"			
Overlap Removal				
η cuts	$ \eta(\ell_e) < 2.47$ excluding $1.37 < \eta(\ell_e) < 1.52$		$ \eta(\ell_\mu) < 2.5$	
Impact Parameters	$ \frac{d_0}{\sigma(d_0)} < 5$, $ z_0 \sin \theta < 0.5$ mm		$ \frac{d_0}{\sigma(d_0)} < 3$, $ z_0 \sin \theta < 0.5$ mm	
Identification WP	TightLH	LooseAndBLayerLH	Medium	Medium
Isolation WP	PLVTight	Not Used	PLVTight	Not Used

Table 4.2: A summary of the requirements applied for selecting tight and loose leptons (e, μ) is shown.

559
560 Jets are required to be within $p_T(\text{jet}) > 20$ GeV. We apply these looser p_T cuts in an attempt to increase our
561 limited signal statistics. A forward jet is a signature of single top production, we therefore require jets to have
562 $|\eta| < 4.5$ in order to include these forward jets.

563 4.2.3 b -tagging

564 The DL1r b -tagger [54] was used to identify jets as b -jets (See Section 3.2.6.4). We use different DL1r working
565 points to identify b -jets in our event selection (See Section 4.4). The working points are defined based off a cut on
566 the DL1r score corresponding to a b -jet tagging efficiency of 60%, 70%, 77% and 85%.

567 Since we are heavily statistically limited, we aim to increase the amount of statistics in our regions. In an attempt
568 to achieve this goal in the $t\bar{t}Z$ CR, b -tagged jets were placed under *tight* and *loose* definitions. A tight b -tagged jet
569 is defined as a jet which passes the 77%, 70%, 65% or 60% DL1r b -tagger working point. A loose b -tagged jet is
570 defined as a jet which passes 85% DL1r b -tagger working point, but not the 77%, 70%, 65% or 60% DL1r b -tagger
571 working points. Different numbers (and definitions) of tight and loose b -tagged jets were tried in each region, with
572 the final selection criteria being chosen which maximised the expected significance of $\sigma(tWZ)$ (See Section 4.4.1).

574 4.3 Kinematic cuts

575 The invariant mass of the OSSF lepton pair coming from the Z boson must equal the invariant mass of the Z boson,
576 and noting that e, μ reconstruction and identification in the ATLAS detector has a high efficiency [48], we can use
577 these OSSF leptons to reconstruct Z bosons with relatively high confidence. We therefore define a Z candidate
578 as an OSSF lepton pair with an invariant mass, m_{OSSF} , satisfying the condition, $|m_{\text{OSSF}} - m_Z| < 30$ GeV, where
579 $m(Z)$ is the nominal Z boson mass (91.1876 GeV [41]). We use this wider mass window to cover the full range of
580 the $m(Z)$ distribution, in an attempt to increase the number of events which pass our baseline selections. Multiple
581 Z candidates can be present in certain decay channels (e.g. $eeee$, $\mu\mu ee$, $\mu\mu\mu\mu$). In these cases, the Z candidate
582 which has an invariant mass closest to the nominal Z boson mass is chosen.

583 In order to suppress potential fakes and quarkonia (low mass resonances such as J/ψ and upsilon) we require that
584 all OSSF lepton pairs have an invariant mass, m_{OSSF} , greater than 10 GeV.

585
586
587 The final state lepton charges must sum to zero. We therefore require, $\sum_{i=1}^4 \text{charge}(\ell_i) = 0$.

588 4.4 Regions and Event Selection

589 We define two tWZ SRs, as opposed to one tWZ SR, in an attempt to suppress and constrain the ZZ background.
590 We require that both tWZ SRs have exactly four tight leptons, exactly one Z -boson candidate, exactly one tight
591 b -tagged jet (from the decay of the top quark) and greater than or equal to one jet. The two tWZ SR's differ
592 by the flavours of their leptons which don't originate from the decay of a Z -boson (Non- Z leptons). The ZZ
593 background has two Z -bosons which decay into a pair of OSSF lepton pairs, in order to mimic the tWZ signal.

Baseline selections				
$N_\ell = 4$				
$p_T(\ell_1, \ell_2, \ell_3, \ell_4) > (28, 10, 10, 10)$ GeV				
$p_T(\text{jet}) > 20$ GeV, $ \eta(\text{jet}) < 4.5$, $\text{jvt} > 0.5$				
$ \eta(\ell_e) < 2.47$ excluding $1.37 < \eta(\ell_e) < 1.52$				
$ \eta(\ell_\mu) < 2.5$				
$\sum_{i=1}^4 \text{charge}(\ell_i) = 0$				
All OSSF lepton pairs require $m_{OSSF} > 10$ GeV				
Regions				
tWZ OF SR	tWZ SF SR	$t\bar{Z}$ CR	ZZb CR	$(tWZ)_{fake}$ CR
$N_\ell(\text{tight}) = 4$	$N_\ell(\text{tight}) = 4$	$N_\ell(\text{tight}) = 4$	$N_\ell(\text{tight}) = 4$	$N_\ell(\text{tight}) = 3$ $N_\ell(\text{loose and NOT tight}) = 1$
N_Z candidate = 1	N_Z candidate = 1	N_Z candidate = 1	N_Z candidate = 2	N_Z candidate = 1
$N_{\text{jet}} \geq 1$	$N_{\text{jet}} \geq 1$	$N_{\text{jet}} \geq 2$	$N_{\text{jet}} \geq 1$	$N_{\text{jet}} \geq 1$
$N_{b\text{-jet}}(\text{tight}) = 1$	$N_{b\text{-jet}}(\text{tight}) = 1$	$N_{b\text{-jet}}(\text{tight}) \geq 1$ $N_{b\text{-jet}}(\text{loose}) \geq 0$ $N_{b\text{-jet}}(\text{tight}) + N_{b\text{-jet}}(\text{loose}) = 2$	$N_{b\text{-jet}}(\text{tight}) = 1$	$N_{b\text{-jet}}(\text{tight}) = 1$
Opp. Flavour Non-Z leptons	Same Flavour Non-Z leptons	-	-	-

Table 4.3: A summary of the requirements applied for selecting events in the signal and control regions is shown.

We take advantage of this to define a tWZ region rich in ZZ background and one with a minimal ZZ background component. This is done by requiring that one of the tWZ SRs has its two non- Z leptons to have opposite flavour and the other tWZ SR is required to have its non- Z leptons to have the same flavour. These two disjoint tWZ SRs are named tWZ OF SR and tWZ SF SR respectively. We therefore expect that the tWZ SF SR contains the majority of tWZ 's ZZ background events.

In order to check the modelling of the most dominant background components in our signal region, we have modified our selection criteria to define $t\bar{Z}$ and ZZb control regions. The $t\bar{Z}$ control region has the same requirement on the number of reconstructed Z boson candidates in the signal region (due to a commonality on the number of Z bosons present in both processes), however we require at least two jets and that exactly two of these jets are b -tagged (corresponding to the b -quark jets originating from the two top-quark decays). We choose to define a ZZb region, as opposed to a ZZ region, since the ZZ background present in the tWZ signal region contains exactly one b -tagged jet. Therefore defining a region with ZZ plus exactly one b -jet more closely resembles the ZZ background present in the signal region. In addition to this, mis-modelling of ZZ has been seen in other analyses [3, 30], further motivating the use of a ZZb control region over a ZZ CR. The ZZb CR requires exactly two Z boson candidates and exactly one b -tagged jet, resulting in an implicit requirement on the number of jets ($N_{\text{jet}} \geq 1$).

In order to constrain the fake lepton component contained within the $t\bar{Z}$ sample, we define a $(tWZ)_{fake}$ CR which is as similar as possible to the tWZ CR but is enhanced in fakes. This is achieved by defining the $(tWZ)_{fake}$ CR to inherit the same selection criteria as the tWZ SRs however, in this case, we require exactly 3 tight leptons and exactly 1 loose (and NOT tight) lepton (since looser leptons are more likely to be fakes, compared to tighter leptons). A $(t\bar{Z})_{fake}$ CR (requiring exactly 3 tight leptons and exactly 1 loose (and NOT tight) lepton) was tried as an alternative to the $(tWZ)_{fake}$ CR, however a much larger suppression of fakes were observed in this region (compared to the $(tWZ)_{fake}$ CR). This suppression of fakes can be explained by the extra b -tagged jet requirement (exactly two b -tagged jets are required in the $t\bar{Z}$ region, compared to exactly one in the tWZ SRs (See Table 4.3)) which causes suppression of fakes via the overlap removal procedure [39].

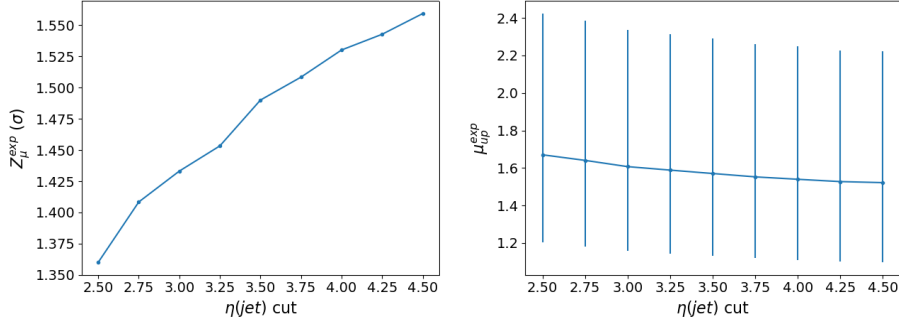
In Table 4.3, a summary of the final selection criteria and region definitions is shown.

4.4.1 Optimization studies for event selection

In order to find the selection criteria for jets and leptons which maximized sensitivity to the tWZ signal, studies were performed by plotting the expected significance (Z_μ^{exp}) and expected upper limit (μ_{up}^{exp}) for different selection

625 criteria. The fitting procedure as described in Section 4.10.1 was used to calculate the expected upper limits and
 626 expected significances in this study. The same selection criteria and regions defined in Table 4.3 was used (unless
 627 otherwise specified), except for the selection(s) which were being optimised in each case.

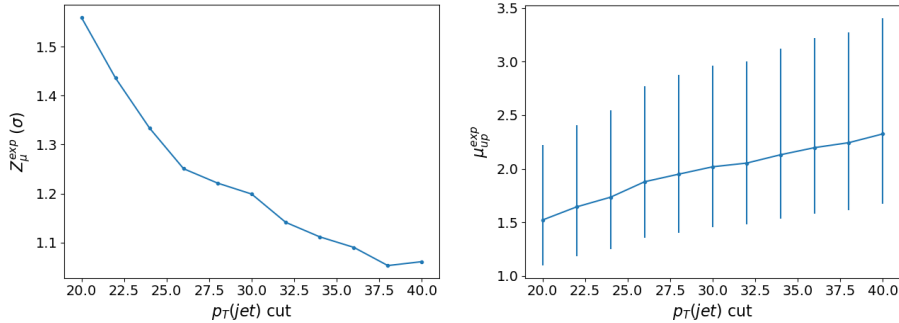
628
 629 In Figure 4.1 the expected significance (Z_μ^{exp}) and expected upper limits (μ_{up}^{exp}) for different $\eta(jet)$ cuts are shown.



630
 631 Figure 4.1: **Left:** Expected significance (Z_μ^{exp}) for different $\eta(jet)$ cuts is shown. The cuts applied on the $\eta(jet)$
 632 are shown on the x-axis and corresponding expected significance from the likelihood fit is shown on the y-axis.
Right: Expected upper limit (μ_{up}^{exp}) for different $\eta(jet)$ cuts is shown. The cuts applied on the $\eta(jet)$ are shown
 on the x-axis and corresponding expected upper limits are shown on the y-axis. Error bars representing the total
 uncertainty on the expected upper limits are shown as vertical lines.

633
 634 From Figure 4.1, we can see that the $\eta(jet)$ cut which maximises the sensitivity of tWZ in the tetralepton channel
 635 is requiring that $\eta(jet) < 4.5$. This selection criteria was set for the $\eta(jet)$ across all regions.

636 In Figure 4.2 the expected significance (Z_μ^{exp}) and expected upper limits (μ_{up}^{exp}) for different $p_T(jet)$ cuts are shown.



637
 638 Figure 4.2: **Left:** Expected significance (Z_μ^{exp}) for different $p_T(jet)$ cuts is shown. The cuts applied on the $p_T(jet)$
 639 are shown on the x-axis and corresponding expected significance from the likelihood fit is shown on the y-axis.
Right: Expected upper limit (μ_{up}^{exp}) for different $p_T(jet)$ cuts is shown. The cuts applied on the $p_T(jet)$ are shown
 on the x-axis and corresponding expected upper limits are shown on the y-axis. Error bars representing the total
 uncertainty on the expected upper limits are shown as vertical lines.

640
 641 From Figure 4.2, we can see that the $p_T(jet)$ cut which maximises the sensitivity of tWZ is requiring that
 642 $p_T(jet) > 20\text{GeV}$. This selection criteria was set for the $p_T(jet)$ across all regions.

643
 644 In Figure 4.3 the expected significance (Z_μ^{exp}) and expected upper limits (μ_{up}^{exp}) for a range of different configurations
 645 of DL1r b -tagged jet working points across different regions.

646 From Figure 4.3, we can see that requiring that b -tagged jets pass the 77% DL1r WP in the tWZ SR, $(tWZ)_{fake}$
 647 CR and the ZZb CR and that at least one b -tagged jet in the $t\bar{t}Z$ SR passes the 77% DL1r WP (the other jet is
 648 just required to pass the 85% DL1r WP) maximises the sensitivity overall (compared to the other investigated
 649 configurations). This configuration was chosen b -tagged jets.

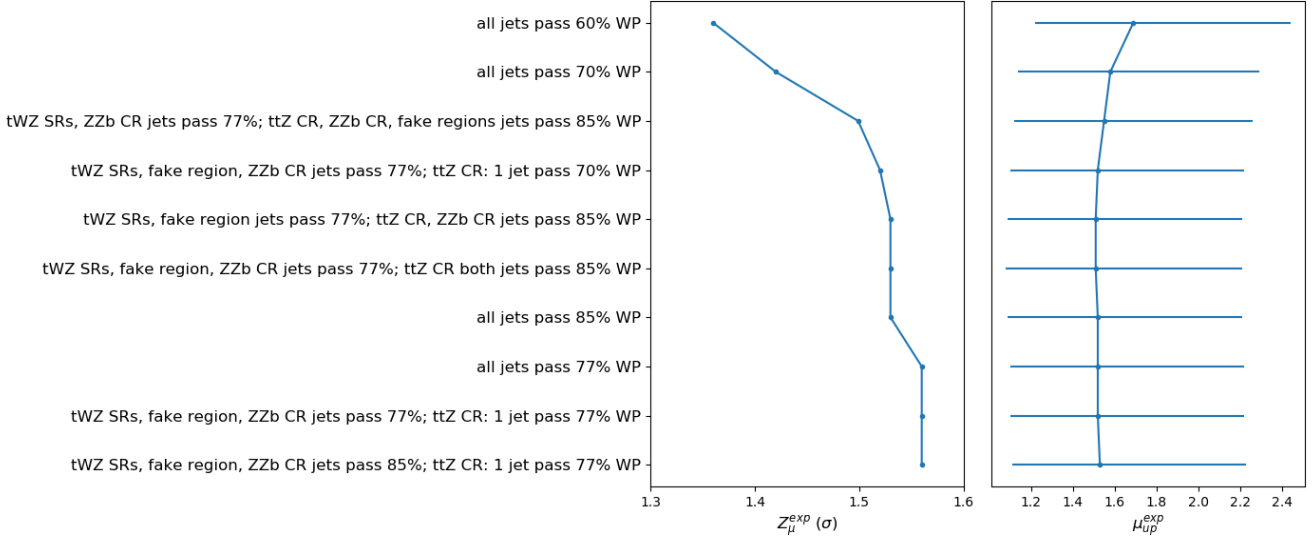


Figure 4.3: Expected significance (Z_μ^{exp}) and expected upper limit ($\mu_{\text{up}}^{\text{exp}}$) for different configurations of DL1r b -tagged jet working points is shown. The common y-axis shows the different configurations of DL1r b -tagged jet working points. On the left panel, the expected significance from the likelihood fit is shown on the x-axis. On the right panel, the expected upper limit from the likelihood fit is shown on the x-axis (with the corresponding total uncertainty represented by horizontal lines).

645
646 The p_T (L Lepton) is constrained by the single lepton triggers (Table ??). We choose to apply a cut on the
647 p_T (NL Lepton) slightly tighter than the tightest single lepton p_T cut in the trigger. We can however, try optimising
648 the p_T (NL Lepton) cut by comparing the expected significance and limit for a range of p_T NL Lepton cuts to
649 determine the cut which maximizes sensitivity.

650
651 In Figure 4.4 the expected significance (Z_μ^{exp}) and expected upper limits ($\mu_{\text{up}}^{\text{exp}}$) for different p_T (NL Lepton) cuts is
652 shown.

653 Since there is a very small change between the different p_T (NL Lepton) cuts on the sensitivity of tWZ , we choose
654 to apply a p_T (NL Lepton) cut at 18 GeV (avoiding a p_T cut near the sharp drop in expected significance after
655 28 GeV), therefore applying a cut above the tightest, looser dilepton trigger p_T cut (17 GeV) to suppress any
656 systematic from the modelling of the trigger efficiency.

657 4.5 Signal and Control Regions

658 In this section, pre-fit distributions of variables in each region are shown. More pre-fit distributions for each region
659 are shown in the appendix (Section A.1.5). For each figure in this section, the data is given by the black points and
660 the MC predictions for each process are given by the histograms. The vertical lines on the data points represent
661 the total uncertainty in the data and the diagonal lined bands represent the total MC uncertainty. The lower panel
662 in each plot shows the ratios of the data to the theoretical predictions. Bins with a $\frac{\text{signal}}{\text{background}}$ yield greater than
663 0.1 are kept blinded. Blinded bins are shaded with black diagonal lines and their data points are omitted.

664
665 In Table 4.4, the pre-fit yields for each sample in each region is shown.
666 The statistical uncertainty associated with the number of raw MC events (weighted by MC event weights) can
667 be quantified by the Number of Equivalent Events [37], N_{equiv} , which relates the sample of N weighted events to
668 N_{equiv} events with all MC event weights equal to 1, that would have the same relative statistical fluctuation. N_{equiv}
669 can be written as,

$$N_{\text{equiv}} = \frac{(\sum_i^N w_i)^2}{\sum_i^N w_i^2} \quad (4.1)$$

670 where w_i is the MC event weight for event i . The standard uncertainty of N_{equiv} is given by $u(N_{\text{equiv}}) = \sqrt{N_{\text{equiv}}}$.

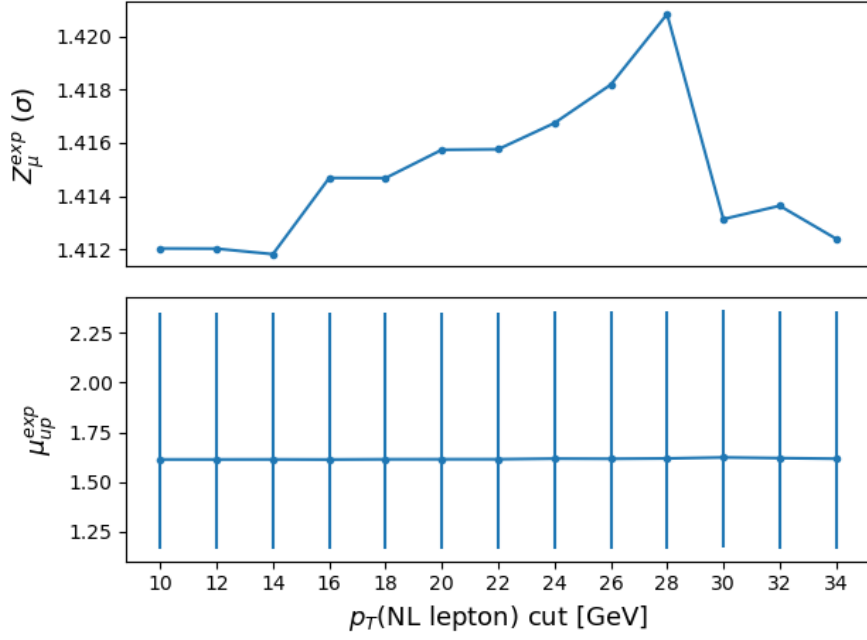


Figure 4.4: Expected significance (Z_μ^{exp}) and expected upper limit (μ_{up}^{exp}) for different p_T (NL Lepton) cuts is shown. The common x-axis shows cut applied to the p_T of the next-to-leading lepton. On the top panel, the expected significance from the likelihood fit is shown on the y-axis. On the bottom panel, the expected upper limit from the likelihood fit is shown on the y-axis (with the corresponding total uncertainty represented by vertical lines).

	tWZ OF SR	tWZ SF SR	$t\bar{t}Z$ CR	ZZb CR	(tWZ) fake CR
$t\bar{t}Z$	13.9325 ± 1.84643	10.1343 ± 1.36039	31.7149 ± 4.46776	5.26303 ± 0.696828	19.1224 ± 2.50011
$t\bar{t}Z$ fakes	0.0687541 ± 0.0482172	0.032827 ± 0.026286	0.0709734 ± 0.043509	0.0474576 ± 0.0301512	4.94775 ± 2.48939
tWZ	3.81359 ± 0.392241	2.57584 ± 0.326401	2.61991 ± 0.861557	1.4023 ± 0.156686	4.93485 ± 0.692143
ZZ	0.546045 ± 0.18975	8.76232 ± 2.66871	1.22357 ± 0.376889	46.0616 ± 13.9203	7.76724 ± 2.36894
$t\bar{t}$	$6e-06 \pm 3.04506e-06$	0.250783 ± 0.44226	0.269883 ± 0.223373	$6e-06 \pm 3.04506e-06$	2.36284 ± 0.927828
tZq	0.0827265 ± 0.0399222	0.0757694 ± 0.0355101	0.0637132 ± 0.0293762	0.0590199 ± 0.0244576	4.91371 ± 0.754695
$t\bar{t}W$	$0.00674747 \pm 0.00793546$	$0.00279491 \pm 0.00287747$	$6e-06 \pm 3.04506e-06$	$0.00221727 \pm 0.00562041$	0.944039 ± 0.296854
WZ	0.0439316 ± 0.0241635	0.0397876 ± 0.0154764	0.0134837 ± 0.0128327	0.0474188 ± 0.0330635	1.84471 ± 0.397076
other	$t\bar{t}t$	$0.000987429 \pm 0.000768187$	$0.00249801 \pm 0.00138007$	0.0141085 ± 0.00486102	$6e-06 \pm 3.04506e-06$
	$t\bar{t}\bar{t}$	0.00934516 ± 0.0080725	0.0107503 ± 0.00852049	0.0570846 ± 0.0206271	$6e-06 \pm 3.04506e-06$
	$t\bar{t}WW$	0.0293456 ± 0.0263573	0.0296011 ± 0.0196075	0.26412 ± 0.0936908	0.013096 ± 0.0323943
	$VVV(V = W/Z)$	0.280384 ± 0.0866421	0.191257 ± 0.0595588	0.0696624 ± 0.0228108	0.171171 ± 0.0526519
	$t\bar{t}H$	0.854064 ± 0.177974	0.674566 ± 0.141771	1.98187 ± 0.406211	0.151447 ± 0.0357703
	Total	19.6684 ± 1.95158	22.7832 ± 3.10338	38.3633 ± 4.6342	53.2187 ± 13.9618
	data	-	-	36	49
					57

Table 4.4: The pre-fit yields for each sample in each region is shown.

671

672 In Table 4.5, the number of equivalent events, N_{equiv} (and its percentage uncertainty), is shown for each sample in each region. N_{equiv} is relatively large, compared to the background processes, for the tWZ signal in all regions.

	tWZ OF SR	tWZ SF SR	$t\bar{t}Z$ CR	ZZb CR	(tWZ) fake CR			
	N_{equiv}	Uncertainty [%]	N_{equiv}	Uncertainty [%]	N_{equiv}	Uncertainty [%]	N_{equiv}	Uncertainty [%]
tWZ	6463.29 ± 80.39	1.24	4153.0 ± 64.44	1.55	4800.67 ± 69.29	1.44	2497.07 ± 49.97	2.0
$t\bar{t}Z$	1363.87 ± 36.93	2.71	1031.04 ± 32.11	3.11	3237.01 ± 56.89	1.76	561.41 ± 23.69	4.22
ZZ	50.89 ± 7.13	14.02	975.61 ± 31.23	3.2	267.85 ± 16.37	6.11	7023.35 ± 83.81	1.19
other	748.0 ± 27.35	3.66	2.47 ± 1.57	63.58	4.23 ± 2.06	48.6	255.32 ± 15.98	6.26
$t\bar{t}Z$ fakes	6.72 ± 2.59	38.56	1.31 ± 1.14	87.34	16.05 ± 4.01	24.96	7.15 ± 2.67	37.41
Total	8632.77 ± 92.91	1.08	6163.44 ± 78.51	1.27	8325.81 ± 91.25	1.1	10344.3 ± 101.71	0.98
							12044.27 ± 109.75	0.91

Table 4.5: The number of equivalent events, N_{equiv} (and its percentage uncertainty), is shown for each sample in each region.

673

674 This tells us that we have a large number of raw MC events for the tWZ sample. An extended tWZ sample was
 675 generated to increase the number of signal events used to train the event-level BDT (See Section 4.7.2).

676 4.5.1 tWZ OF SR

677 In this section, pre-fit distributions of variables in the tWZ OF SR are shown. More pre-fit distributions for the
 678 tWZ OF SR are shown in the appendix (Section A.1.1).

679
 680 In Figure A.1 MC predictions for p_T , η and ϕ for leading (L) leptons and next-to-leading (NL) leptons in the tWZ
 681 OF SR region is shown.

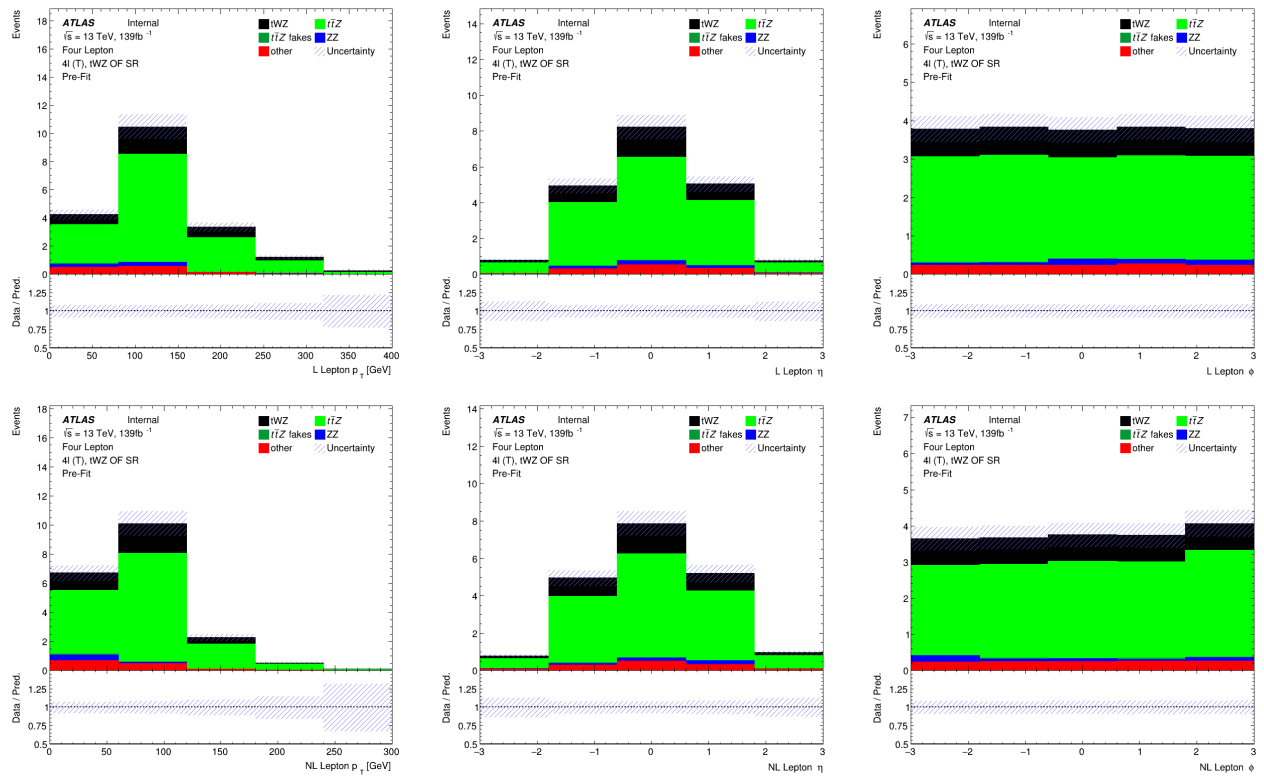


Figure 4.5: MC predictions for p_T , η and ϕ for leading (L) leptons (top row) and next-to-leading (NL) leptons (bottom row) in the tWZ OF SR region is shown.

682 In Figure 4.6 MC predictions for p_T , η and ϕ for leading (L) jets and next-to-leading (NL) jets in the tWZ OF SR
 683 region is shown.

684 In Figure 4.7 MC predictions for p_T , η and ϕ of the next-to-next-to-leading (NNL) jets, H_T (scalar sum of Jet p_T)
 685 and the Number of jets in the tWZ OF SR region is shown.

686 In Figure 4.8 MC predictions for p_T , η and ϕ of the leading b-tagged jets, the scalar sum of b-tagged jet p_T and
 687 the Number of b-tagged jets in the tWZ OF SR region is shown.

688 4.5.2 tWZ SF SR

689 In this section, pre-fit distributions of variables in the tWZ SF SR are shown. More pre-fit distributions for the
 690 tWZ SF SR are shown in the appendix (Section A.1.2).

691
 692 In Figure A.14 MC predictions for p_T , η and ϕ for leading (L) leptons and next-to-leading (NL) leptons in the tWZ
 693 SF SR region is shown.

694 In Figure 4.10 MC predictions for p_T , η and ϕ for leading (L) jets and next-to-leading (NL) jets in the tWZ SF SR
 695 region is shown.

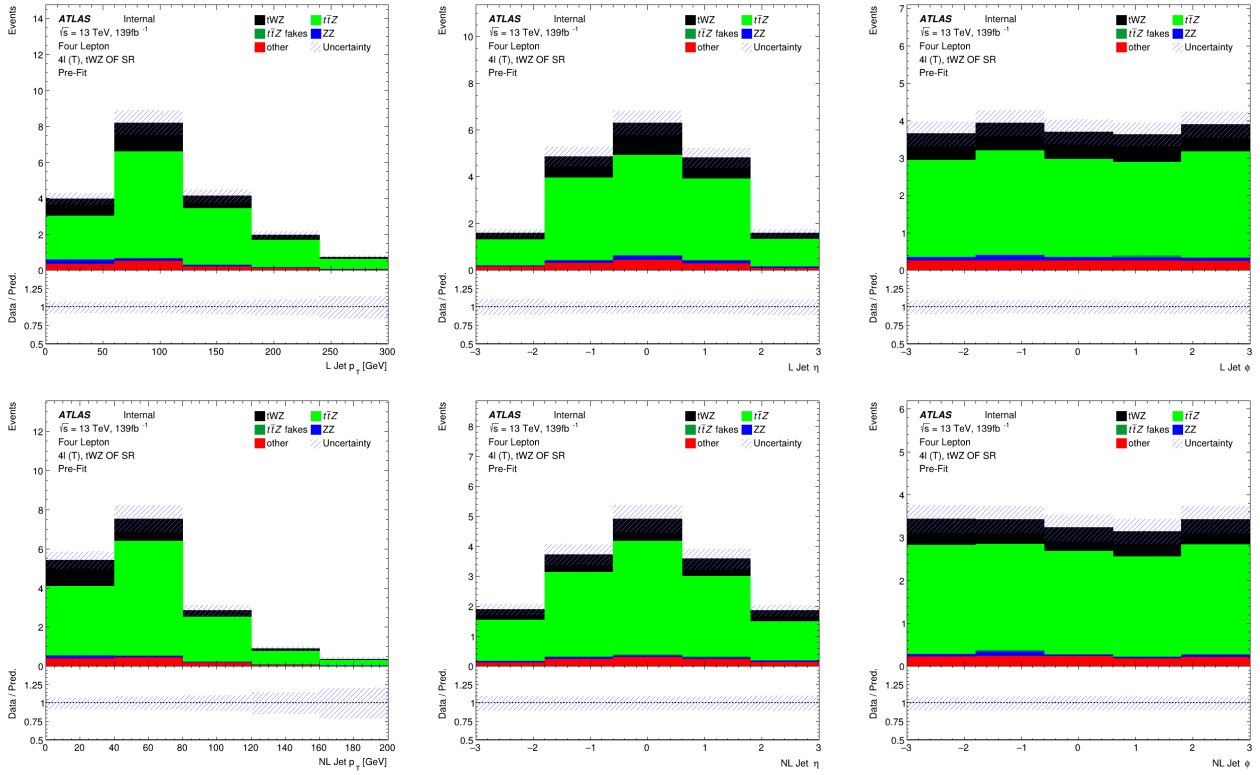


Figure 4.6: MC predictions for p_T , η and ϕ for leading (L) jets (top row) and next-to-leading (NL) jets (bottom row) in the tWZ OF SR region is shown.

- 696 In Figure 4.11 MC predictions for p_T , η and ϕ of the next-to-next-to-leading (NNL) jets, H_T (scalar sum of Jet p_T)
697 and the Number of jets in the tWZ SF SR region is shown.
698 In Figure 4.12 MC predictions for p_T , η and ϕ of the leading b-tagged jets, the scalar sum of b-tagged jet p_T and
699 the Number of b-tagged jets in the tWZ SF SR region is shown.

700 4.5.3 $t\bar{t}Z$ CR

- 701 In this section, pre-fit distributions of variables in the $t\bar{t}Z$ CR are shown. More pre-fit distributions for the $t\bar{t}Z$ CR
702 are shown in the appendix (Section A.1.3).
703
704 In Figure A.27 MC predictions for p_T , η and ϕ for leading (L) leptons and next-to-leading (NL) leptons in the $t\bar{t}Z$
705 CR region is shown.
706 In Figure 4.14 MC predictions for p_T , η and ϕ for leading (L) jets and next-to-leading (NL) jets in the $t\bar{t}Z$ CR
707 region is shown.
708 In Figure 4.15 MC predictions for p_T , η and ϕ of the next-to-next-to-leading (NNL) jets, H_T (scalar sum of Jet p_T)
709 and the Number of jets in the $t\bar{t}Z$ CR region is shown.
710 In Figure 4.16 MC predictions for p_T , η and ϕ of the leading b-tagged jets, the scalar sum of b-tagged jet p_T and
711 the Number of b-tagged jets in the $t\bar{t}Z$ CR region is shown.

712 4.5.4 ZZb CR

- 713 In this section, pre-fit distributions of variables in the ZZb CR are shown. More pre-fit distributions for the ZZb
714 CR are shown in the appendix (Section A.1.4).
715
716 In Figure A.41 MC predictions for p_T , η and ϕ for leading (L) leptons and next-to-leading (NL) leptons in the ZZb
717 CR region is shown.
718 In Figure 4.18 MC predictions for p_T , η and ϕ for leading (L) jets and next-to-leading (NL) jets in the ZZb CR

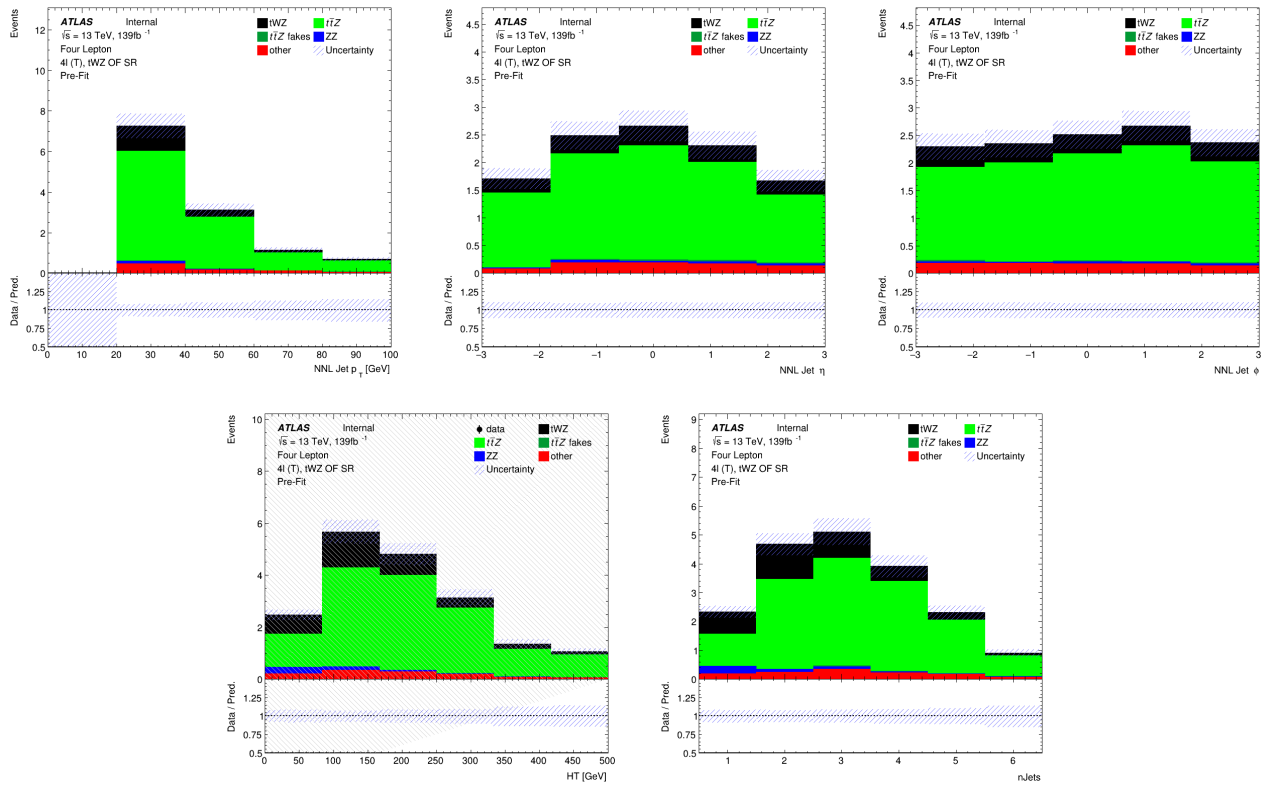


Figure 4.7: Top row: MC predictions for p_T , η and ϕ for next-to-next-to-leading (NNL) jets in the tWZ OF SR region is shown. **Bottom row:** MC predictions for H_T (scalar sum of Jet p_T) (left) and the Number of jets (right) in the tWZ OF SR region is shown.

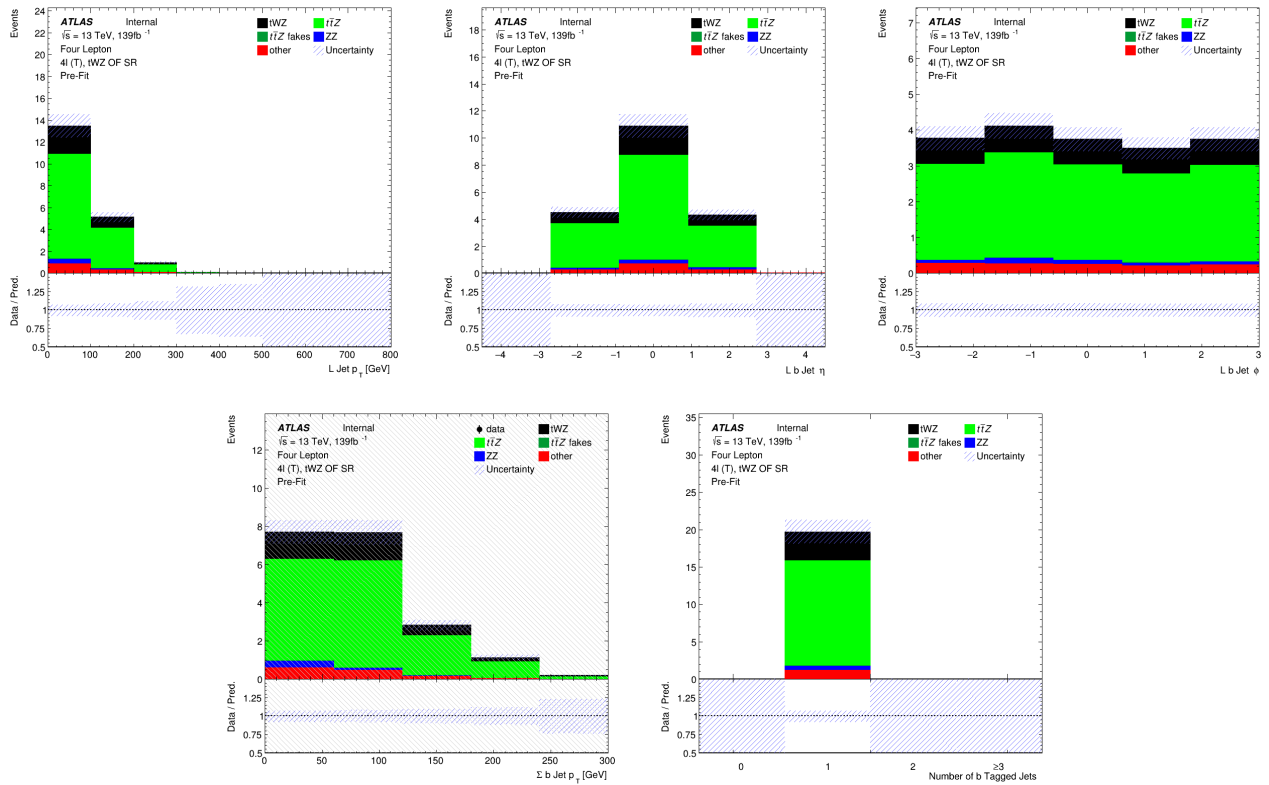


Figure 4.8: **Top row:** MC predictions for p_T , η and ϕ for leading b-tagged jets in the tWZ OF SR region is shown. **Bottom row:** MC predictions for the scalar sum of b-tagged jet p_T (left) and the Number of b-tagged jets (right) in the tWZ OF SR region is shown.

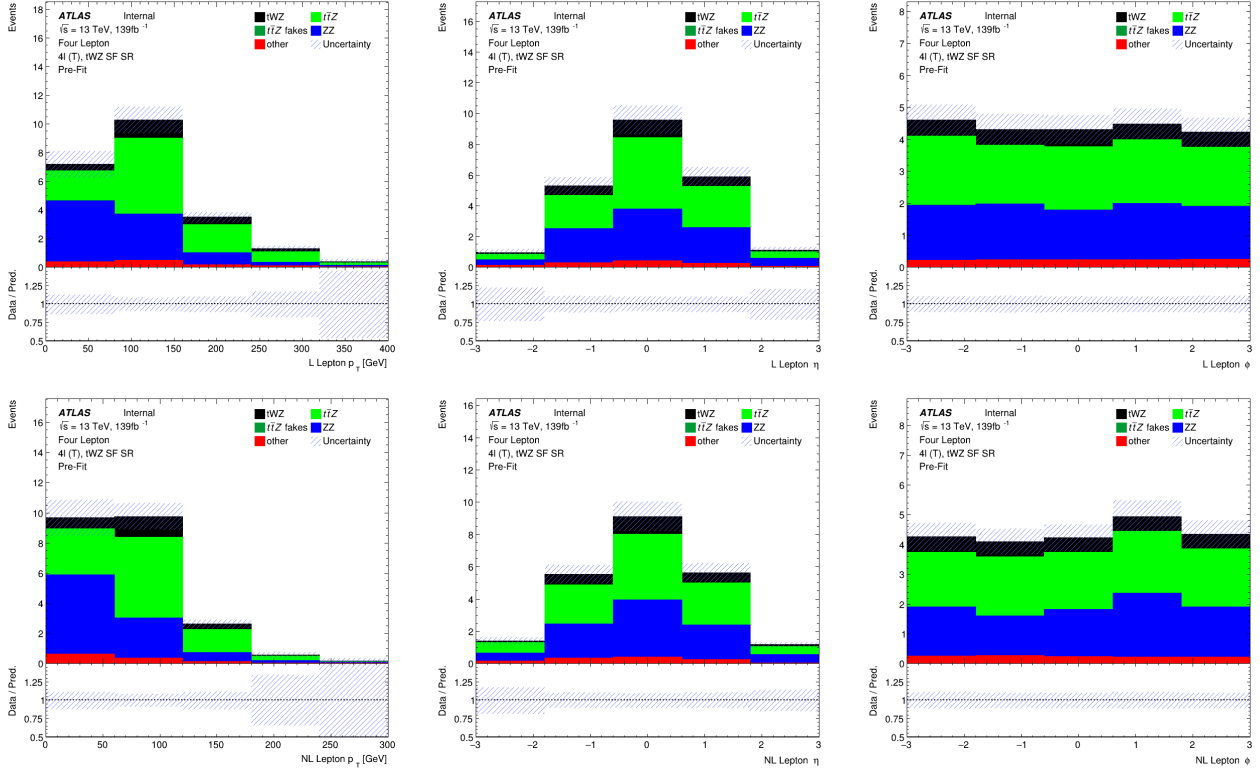


Figure 4.9: MC predictions for p_T , η and ϕ for leading (L) leptons (top row) and next-to-leading (NL) leptons (bottom row) in the tWZ SF SR region is shown.

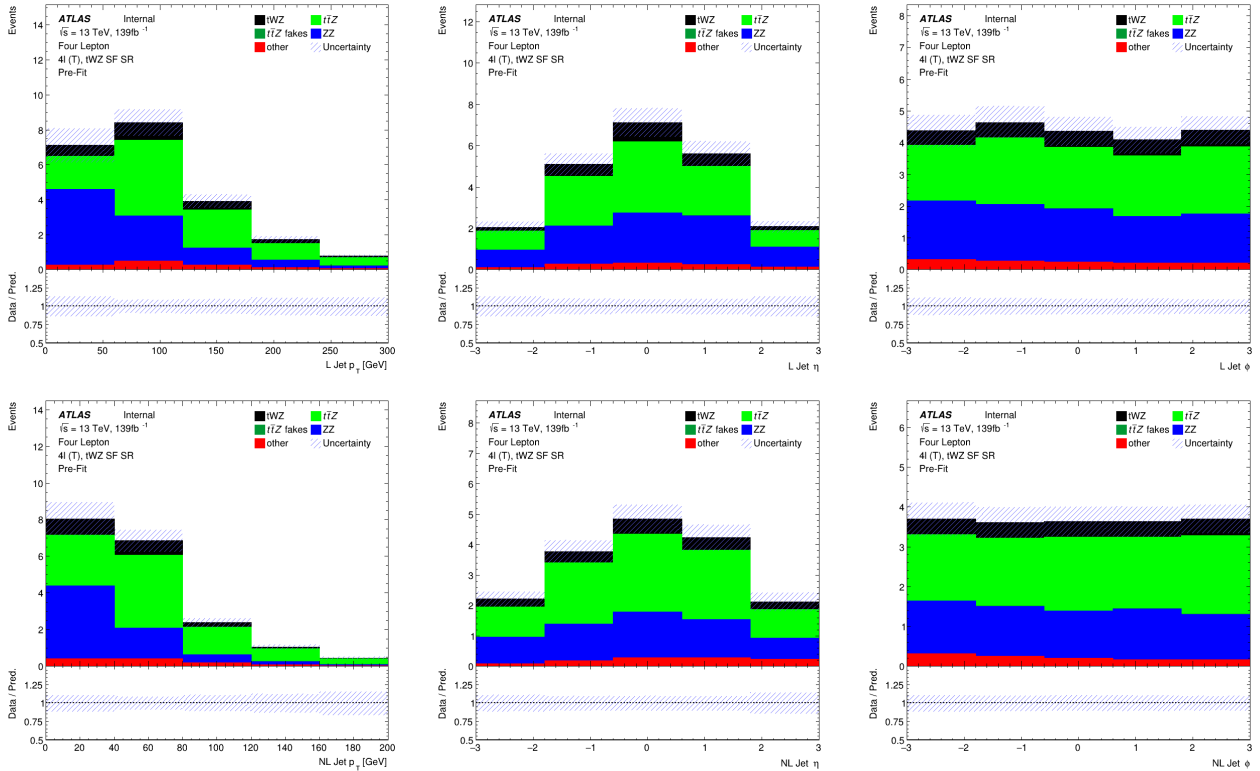


Figure 4.10: MC predictions for p_T , η and ϕ for leading (L) jets (top row) and next-to-leading (NL) jets (bottom row) in the tWZ SF SR region is shown.

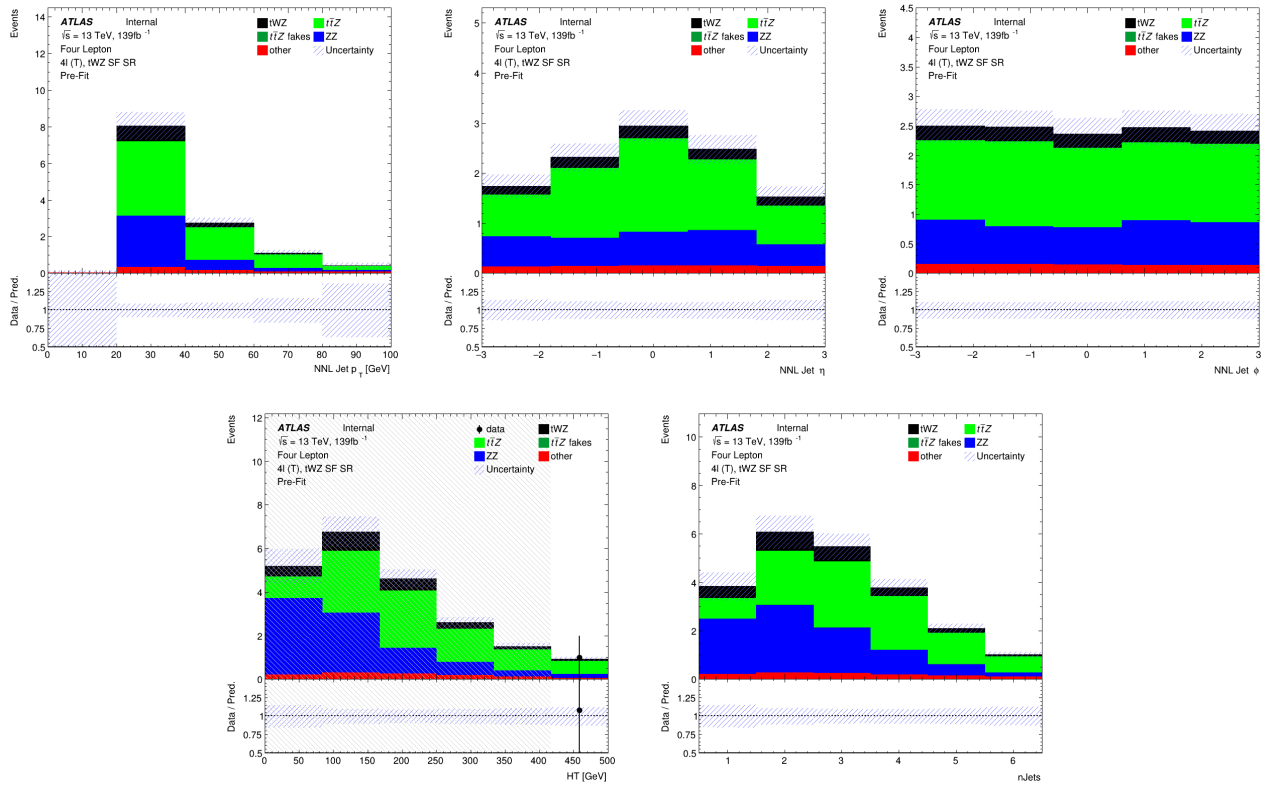


Figure 4.11: **Top row:** MC predictions for p_T , η and ϕ for next-to-next-to-leading (NNL) jets in the tWZ SF SR region is shown. **Bottom row:** MC predictions for H_T (scalar sum of Jet p_T) (left) and the Number of jets (right) in the tWZ SF SR region is shown.

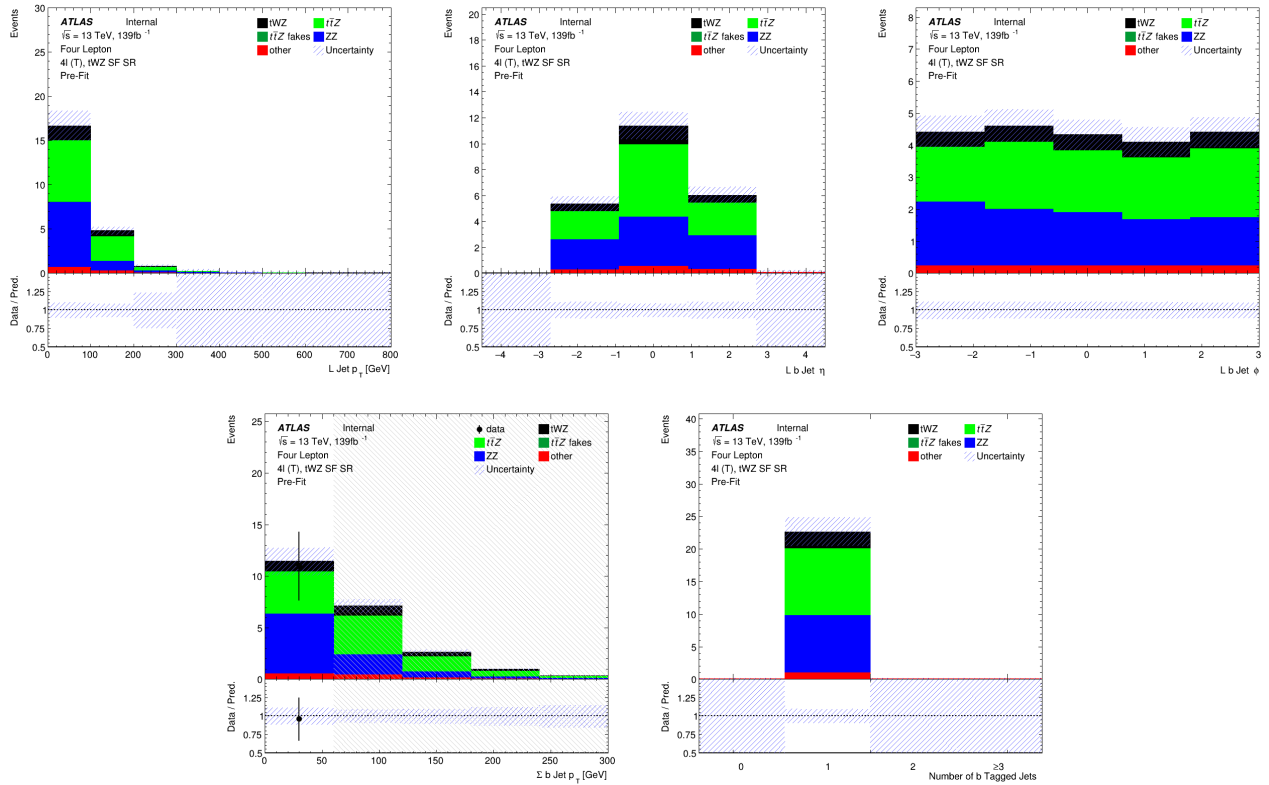


Figure 4.12: **Top row:** MC predictions for p_T , η and ϕ for leading b-tagged jets in the tWZ SF SR region is shown. **Bottom row:** MC predictions for the scalar sum of b-tagged jet p_T (left) and the Number of b-tagged jets (right) in the tWZ SF SR region is shown.

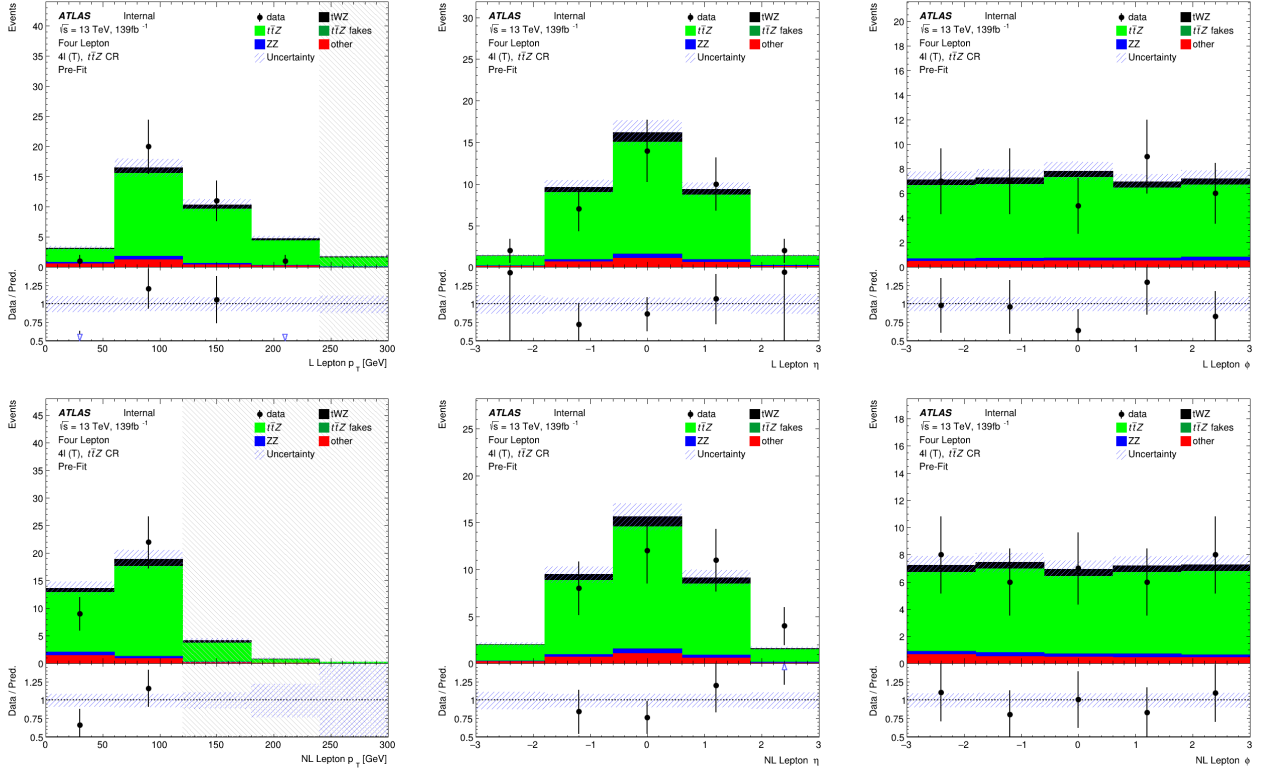


Figure 4.13: MC predictions for p_T , η and ϕ for leading (L) leptons (top row) and next-to-leading (NL) leptons (bottom row) in the $t\bar{t}Z$ CR region is shown.

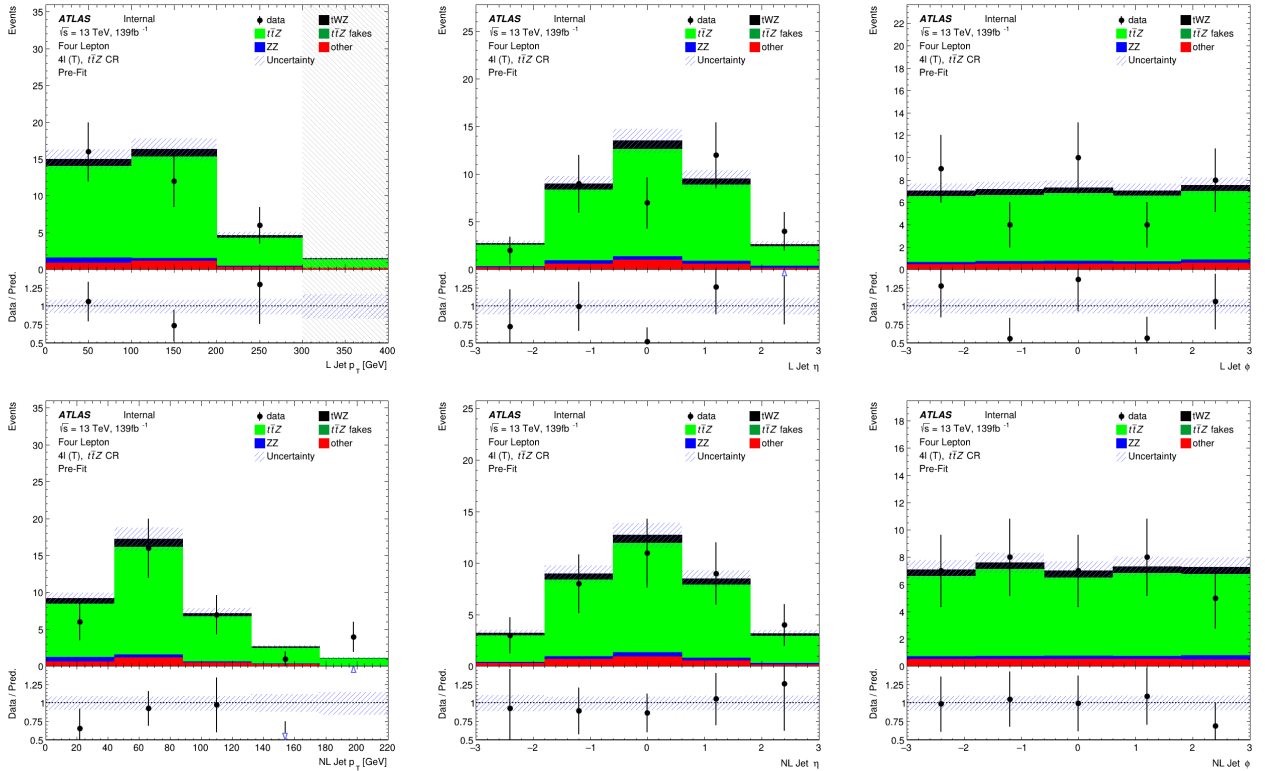


Figure 4.14: MC predictions for p_T , η and ϕ for leading (L) jets (top row) and next-to-leading (NL) jets (bottom row) in the $t\bar{t}Z$ CR region is shown.

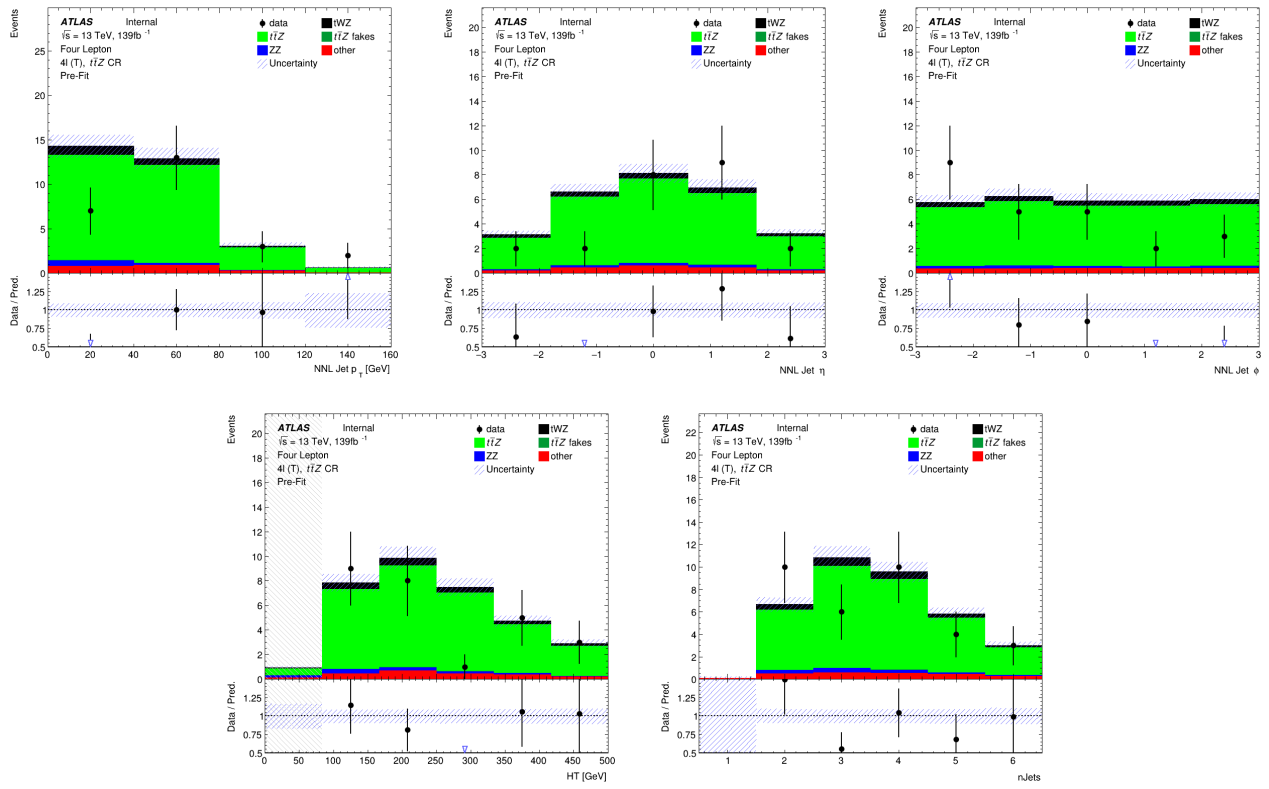


Figure 4.15: **Top row:** MC predictions for p_T , η and ϕ for next-to-next-to-leading (NNL) jets in the $t\bar{t}Z$ CR region is shown. **Bottom row:** MC predictions for H_T (scalar sum of Jet p_T) (left) and the Number of jets (right) in the $t\bar{t}Z$ CR region is shown.

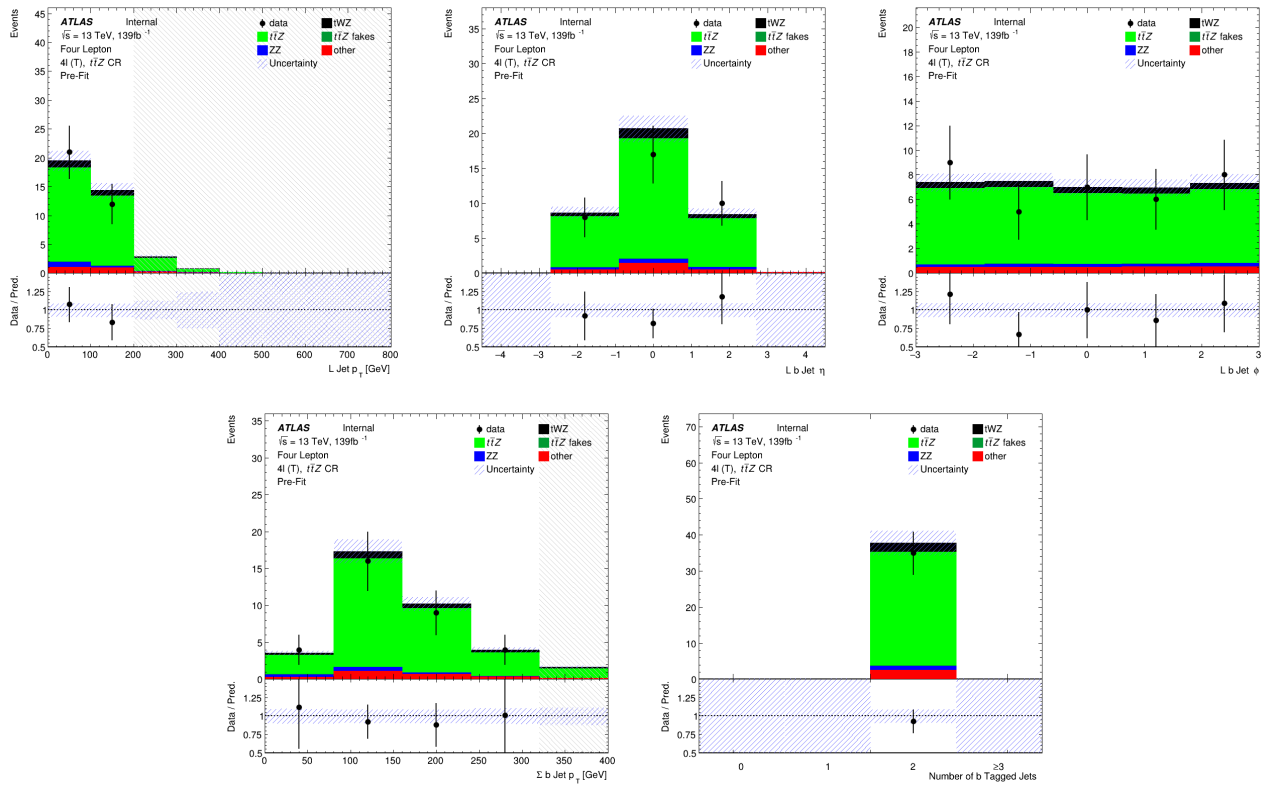


Figure 4.16: **Top row:** MC predictions for p_T , η and ϕ for leading b-tagged jets in the $t\bar{t}Z$ CR region is shown. **Bottom row:** MC predictions for the scalar sum of b-tagged jet p_T (left) and the Number of b-tagged jets (right) in the $t\bar{t}Z$ CR region is shown.

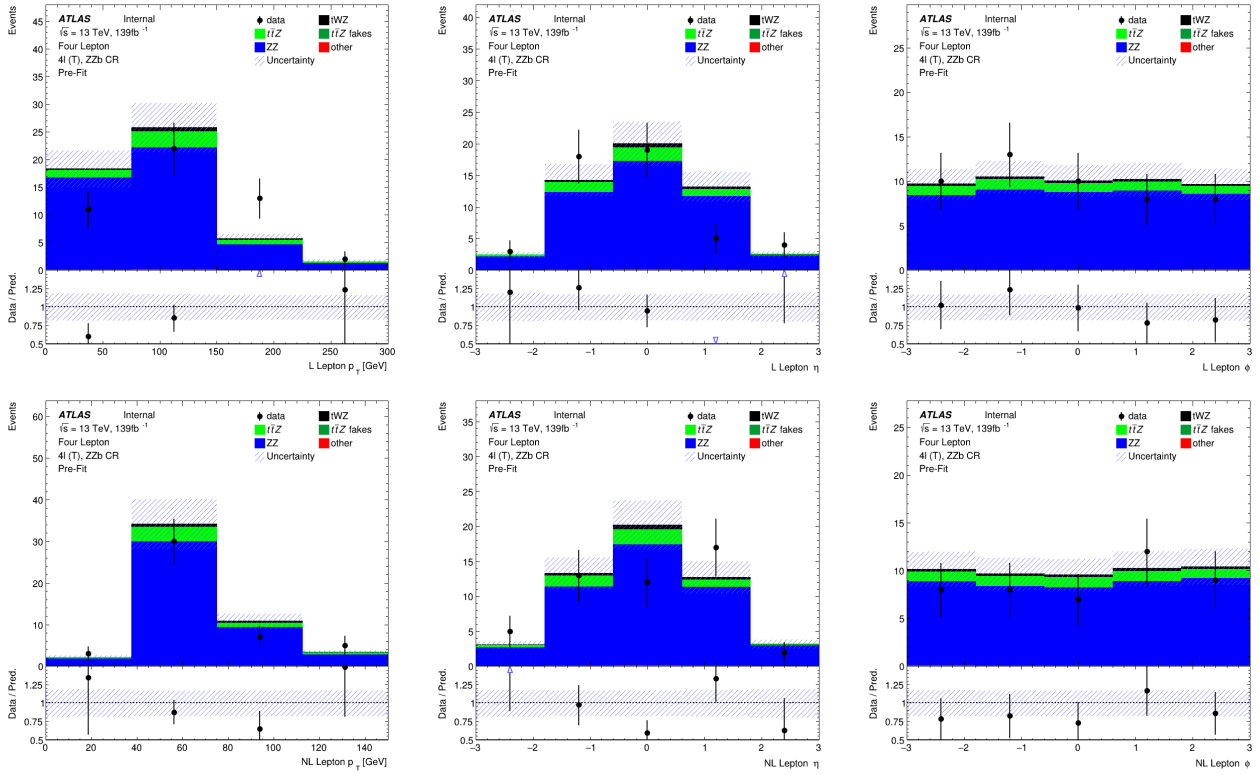


Figure 4.17: MC predictions for p_T , η and ϕ for leading (L) leptons (top row) and next-to-leading (NL) leptons (bottom row) in the ZZb CR region is shown.

region is shown.

In Figure 4.19 MC predictions for p_T , η and ϕ of the next-to-next-to-leading (NNL) jets, H_T (scalar sum of Jet p_T) and the Number of jets in the ZZb CR region is shown.

In Figure 4.20 MC predictions for p_T , η and ϕ of the leading b-tagged jets, the scalar sum of b-tagged jet p_T and the Number of b-tagged jets in the ZZb CR region is shown.

4.5.5 $(tWZ)_{\text{fake}}$ CR

In this section, pre-fit distributions of variables in the $(tWZ)_{\text{fake}}$ CR are shown. More pre-fit distributions for the $(tWZ)_{\text{fake}}$ CR are shown in the appendix (Section ??).

In Figure 4.21 MC predictions for p_T , η and ϕ for leading (L) leptons and next-to-leading (NL) leptons in the $(tWZ)_{\text{fake}}$ CR region is shown.

In Figure 4.22 MC predictions for p_T , η and ϕ for leading (L) jets and next-to-leading (NL) jets in the $(tWZ)_{\text{fake}}$ CR region is shown.

In Figure 4.23 MC predictions for p_T , η and ϕ of the next-to-next-to-leading (NNL) jets, H_T (scalar sum of Jet p_T) and the Number of jets in the $(tWZ)_{\text{fake}}$ CR region is shown.

In Figure 4.24 MC predictions for p_T , η and ϕ of the leading b-tagged jets, the scalar sum of b-tagged jet p_T and the Number of b-tagged jets in the $(tWZ)_{\text{fake}}$ CR region is shown.

Given the limited statistics which we are presented with in the tetralepton channel, we nevertheless observe relatively good agreement overall between data and MC.

4.6 Fake Lepton Estimation

Fake leptons are objects reconstructed as leptons, but do not correspond to the leptons which we are interested in our analysis. Fake leptons can be split up into two main categories, irreducible (prompt) fakes and reducible (non-prompt) fakes. Irreducible fakes are true leptons which do not come from the process of interest. Reducible

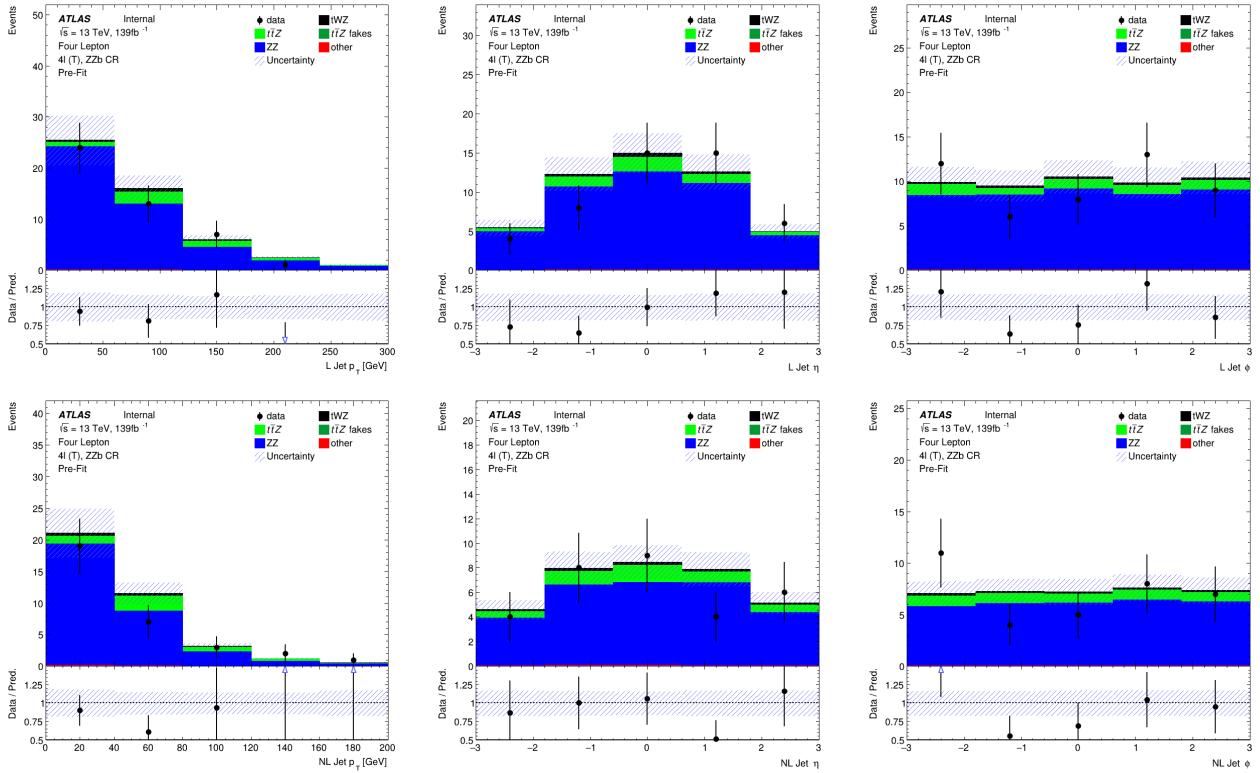


Figure 4.18: MC predictions for p_T , η and ϕ for leading (L) jets (top row) and next-to-leading (NL) jets (bottom row) in the ZZb CR region is shown.

fakes are objects which are mis-identified or incorrectly reconstructed as leptons. In the ATLAS detector, the probability for a fake to occur is very low.

We aim to estimate the fake lepton contribution in this analysis. We start off by noticing that $t\bar{t}Z$ is our most dominant background ($\sim 75\%$ of the total background contribution) and will therefore have the largest fake component compared to all other samples considered in the analysis. The fake lepton efficiency, ϵ , can be written as $\epsilon = \frac{N_{\text{fake}}^{\text{tight}}}{N_{\text{fake}}^{\text{loose}}}$, where $N_{\text{fake}}^{\text{tight}}$ is the number of fake leptons which pass the tight lepton selection (See Section 4.2.1) and $N_{\text{fake}}^{\text{loose}}$ is the number of fake leptons which pass the loose lepton selection (See Section 4.2.1). The probability of one fake lepton to occur, $P(\text{one fake } \ell)$, is proportional to ϵ and the probability for two fakes to occur is simply, $P(\text{two fake } \ell) = (P(\text{one fake } \ell))^2 \propto \epsilon^2$. Since $\epsilon < 1$, we have $P(\text{one fake } \ell) \ll P(\text{two fake } \ell)$. For this analysis we shall investigate the fake lepton component to the highest order and therefore we will consider the case where at least one fake lepton occurs in a $t\bar{t}Z$ event.

Firstly, we split up the dominant $t\bar{t}Z$ background into $t\bar{t}Z$ and $(t\bar{t}Z)_{\text{fake}}$ components. Secondly, we define a $(tWZ)_{\text{fake}}$ CR (See Section 4.4) which is enhanced in fakes and aims to constrain the $(t\bar{t}Z)_{\text{fake}}$ background in the SR.

All events which contribute to the $(t\bar{t}Z)_{\text{fake}}$ background are determined by the IFF Truth Classifier [44]. The IFF Truth Classifier is a tool which aims to classify leptons based off their truth information. It uses the more general MCTruthClassifier [51] tool's output as input and returns one of the following lepton categories: Unknown, KnownUnknown (leptons which can (in principle) be classified, but the MCTruthClassifier fails to classify the lepton's truth type or origin), IsoElectron, ChargeFlipIsoElectron, PromptMuon, PromptPhotonConversion, ElectronFromMuon, TauDecay, BHadronDecay, CHadronDecay or LightFlavorDecay (More details [45]). Given these categories, we consider leptons classified as PromptPhotonConversion, BHadronDecay, CHadronDecay or LightFlavorDecay (i.e. a lepton originating from the decay of a b -Hadron, c -Hadron or light-flavour jet) to be fakes. We require that events which contribute to the $(t\bar{t}Z)_{\text{fake}}$ background are those where at least one lep-

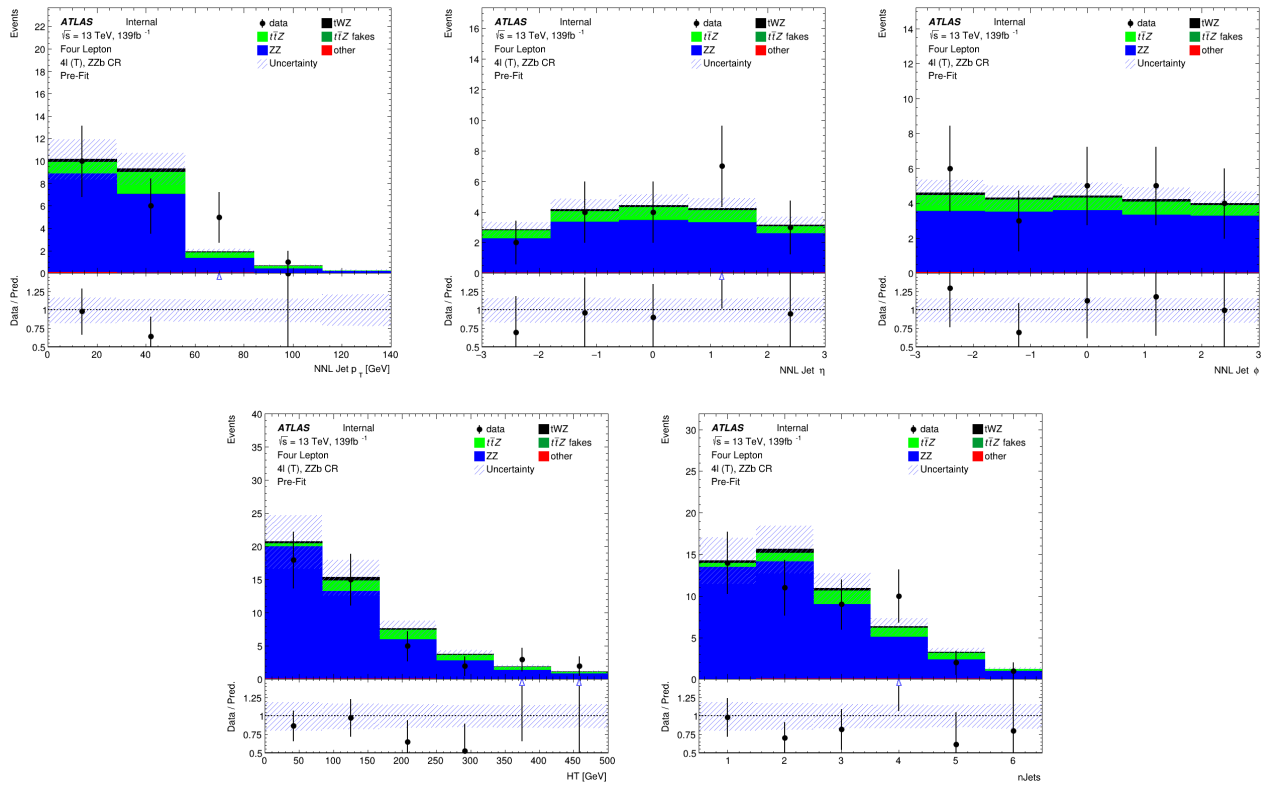


Figure 4.19: **Top row:** MC predictions for p_T , η and ϕ for next-to-next-to-leading (NNL) jets in the ZZb CR region is shown. **Bottom row:** MC predictions for H_T (scalar sum of Jet p_T) (left) and the Number of jets (right) in the ZZb CR region is shown.

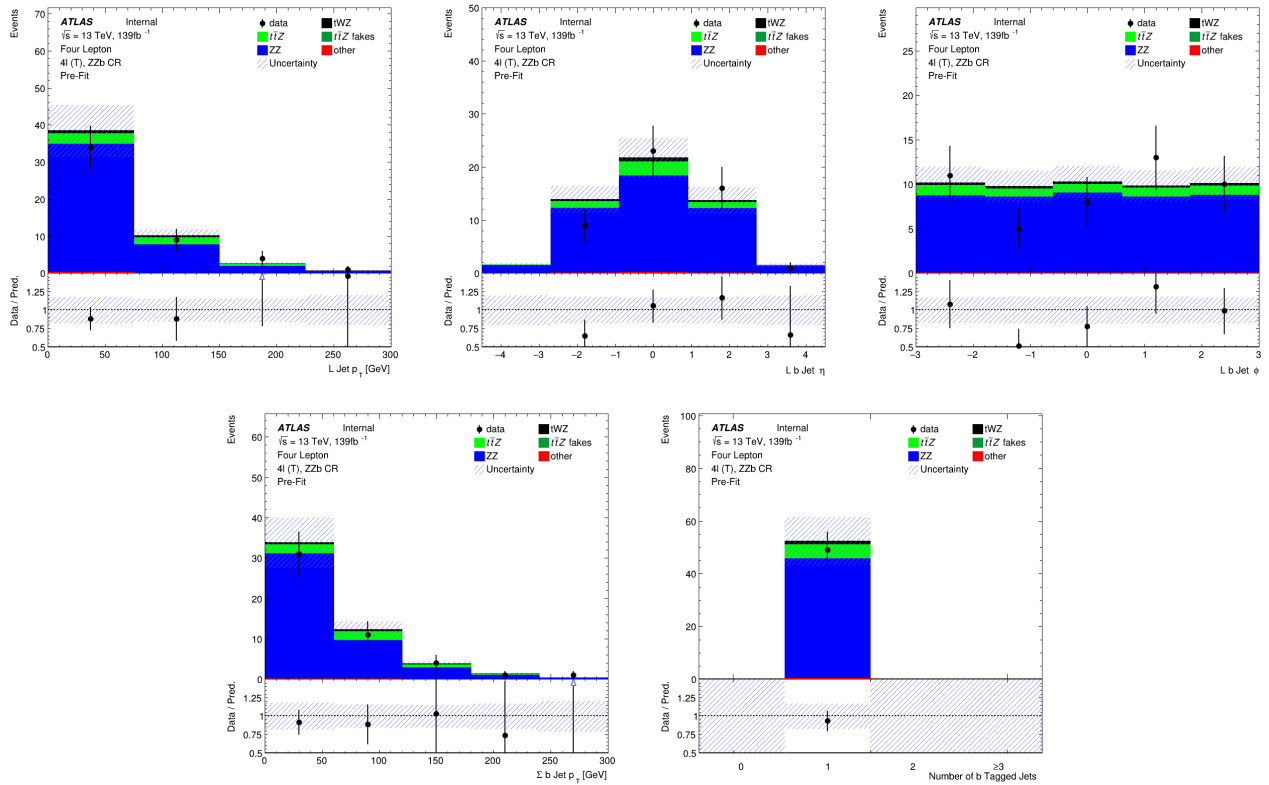


Figure 4.20: **Top row:** MC predictions for p_T , η and ϕ for leading b-tagged jets in the ZZb CR region is shown. **Bottom row:** MC predictions for the scalar sum of b-tagged jet p_T (left) and the Number of b-tagged jets (right) in the ZZb CR region is shown.

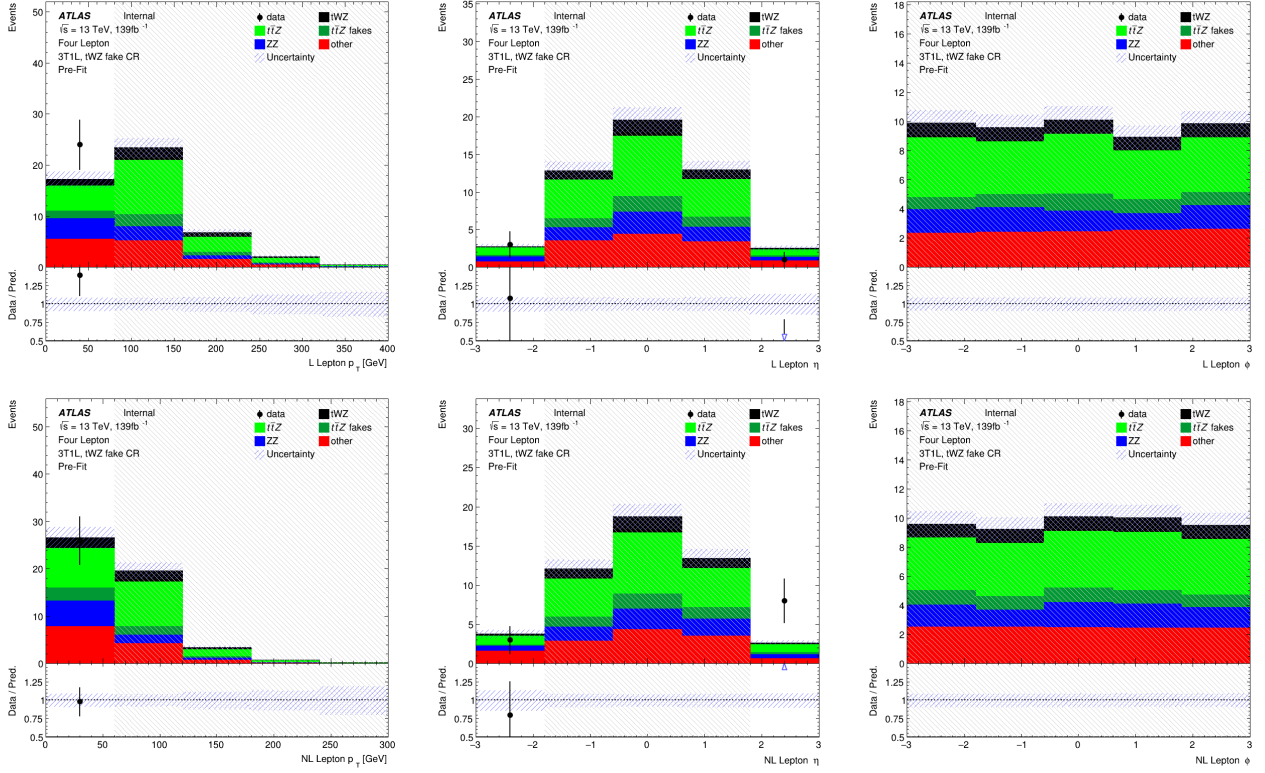


Figure 4.21: MC predictions for p_T , η and ϕ for leading (L) leptons (top row) and next-to-leading (NL) leptons (bottom row) in the (tWZ) fake CR region is shown.

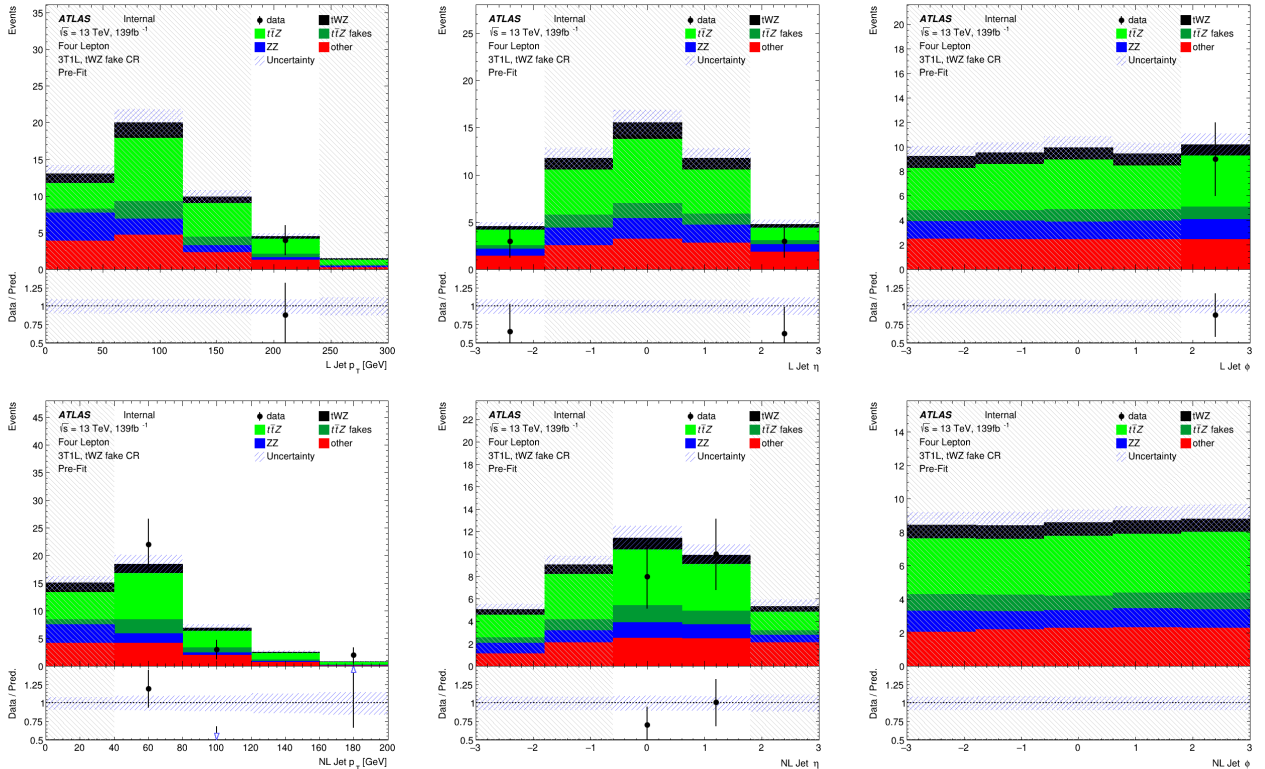


Figure 4.22: MC predictions for p_T , η and ϕ for leading (L) jets (top row) and next-to-leading (NL) jets (bottom row) in the (tWZ) fake CR region is shown.

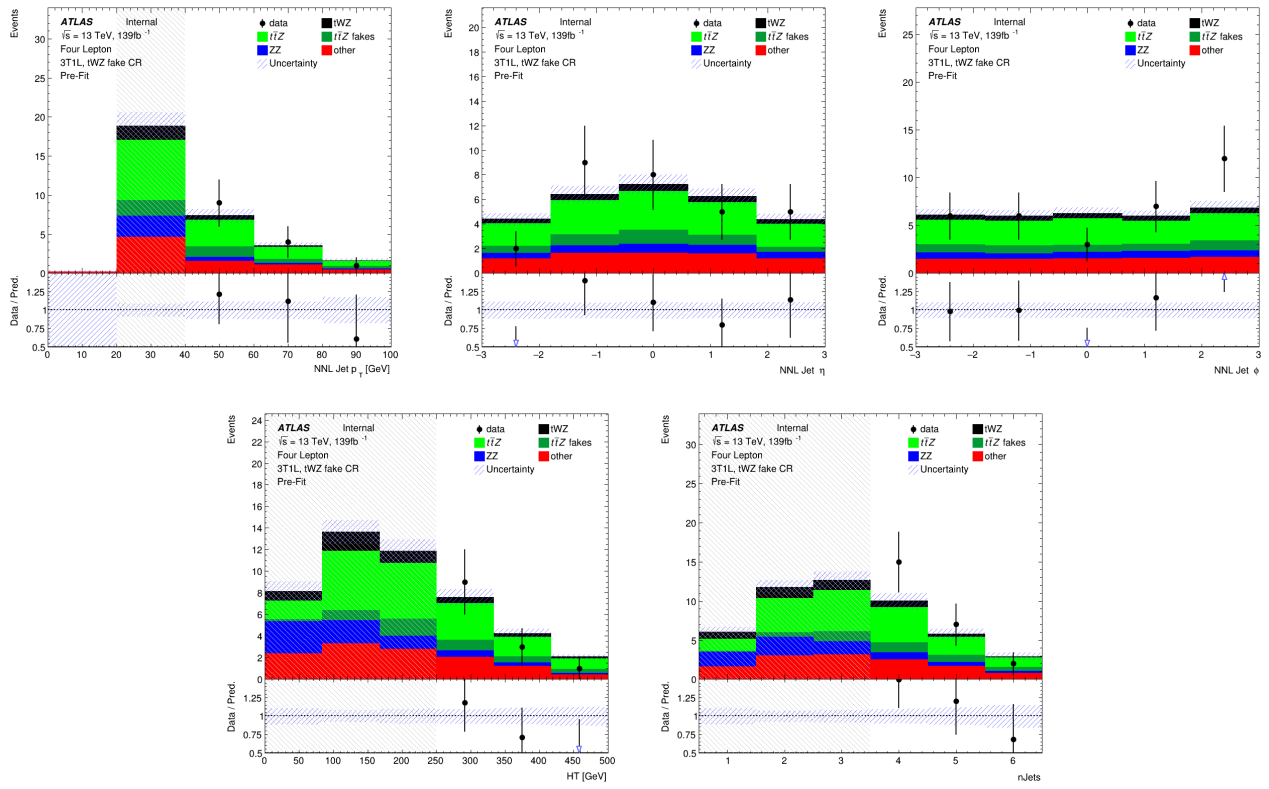


Figure 4.23: **Top row:** MC predictions for p_T , η and ϕ for next-to-next-to-leading (NNL) jets in the $(tWZ)_{\text{fake}}$ CR region is shown. **Bottom row:** MC predictions for H_T (scalar sum of Jet p_T) (left) and the Number of jets (right) in the $(tWZ)_{\text{fake}}$ CR region is shown.

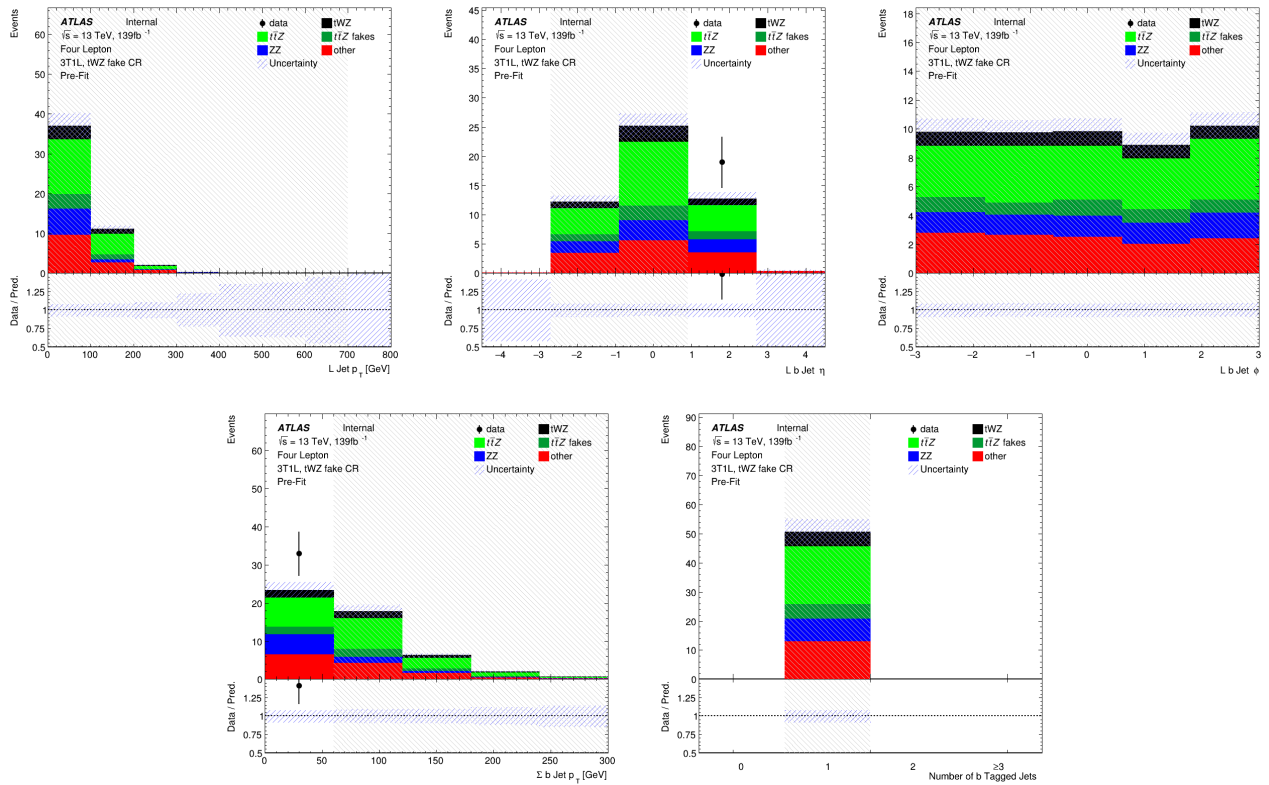


Figure 4.24: **Top row:** MC predictions for p_T , η and ϕ for leading b-tagged jets in the $(tWZ)_{\text{fake}}$ CR region is shown. **Bottom row:** MC predictions for the scalar sum of b-tagged jet p_T (left) and the Number of b-tagged jets (right) in the $(tWZ)_{\text{fake}}$ CR region is shown.

ton from the $t\bar{t}Z$ sample are classified by the IFF Truth Classifier with one of the four aforementioned categories.

The $(tWZ)_{\text{fake}}$ CR aims to be as similar as possible to the tWZ SRs, but enhanced in fakes. This CR can then be used to constrain the normalisation of the $(t\bar{t}Z)_{\text{fake}}$ template. To ensure that this region is enhanced in fakes, we require that it contains 3 tight leptons and 1 loose lepton, since loose leptons are more likely to be fakes. By using the p_T of the loose lepton ($p_T(\text{Loose Lepton})$) in this region as the variable used in the fit, the shape (and normalisation) of the $(t\bar{t}Z)_{\text{fake}}$ template can be constrained.

In Figure 4.25, the number of leptons classified as fake, split up by their IFF Truth classification, in each region is shown.

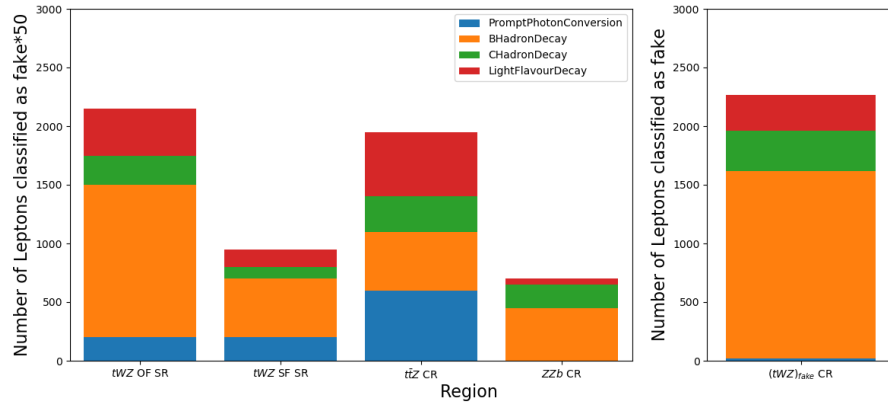


Figure 4.25: The number of leptons classified as fake, split up by their IFF Truth classification, in each region is shown. The left panel shows the number of leptons classified as fakes, scaled by a factor of 50, on the y-axis. The right panel shows the number of leptons classified as fakes (unscaled), on the y-axis. The different signal and control regions are shown on the x-axes of the left and right panels. The IFF truth classification of the leptons are shown in the legend and correspond to the different coloured stacked histograms.

Around 50 times more fake leptons pass our selection criteria for the $(tWZ)_{\text{fake}}$ CR, compared to remaining four regions. This relative abundance of fake leptons present in the $(tWZ)_{\text{fake}}$ CR further justifies our use of this region to constrain the fake lepton component.

In Figure 4.26, the relative dominance of the different classifications for fake leptons (classified by the IFF truth classifier) in each region, is shown.

The majority of fake leptons which pass our selection criteria originate from the decay of b -hadrons, in all regions but the $t\bar{t}Z$ CR. The smaller proportion of fake leptons originating from b -hadron decays in the $t\bar{t}Z$ CR could possibly be due to statistical fluctuations resulting from the low number of fake leptons which pass our selection criteria in this region (~ 40 fake leptons).

In Figure 4.27, the amount of fake and real $t\bar{t}Z$ events which pass our selection criteria, in each region, is shown. Around 20% of all $t\bar{t}Z$ events are classified as fake events (having one or more of its leptons being classified as fake) in the $(tWZ)_{\text{fake}}$ CR. The tWZ OF SR, tWZ SF SR, $t\bar{t}Z$ CR and ZZb CR have less than 1% of their total $t\bar{t}Z$ events being fake. The non-negligible amount of fake $t\bar{t}Z$ events present in the $(tWZ)_{\text{fake}}$ CR, allows the $t\bar{t}Z$ fake background to be constrained by the $(tWZ)_{\text{fake}}$ CR.

4.7 Machine Learning Techniques

Now that we have our baseline selections applied and our regions defined, we implement two Boosted Decision Trees (BDT) in order to discriminate between tWZ and our most prominent background process, $t\bar{t}Z$ and ZZ . We chose to use a BDT, as opposed to another ML algorithm, since they are very stable and perform well with minimal/no optimisation or tweaking of the hyper parameters. A multi-layered sequential neural network was tried, however, it was out-performed by a BDT. More specifically, Scikit-Learn’s `GradientBoostingClassifier` [60] was used.

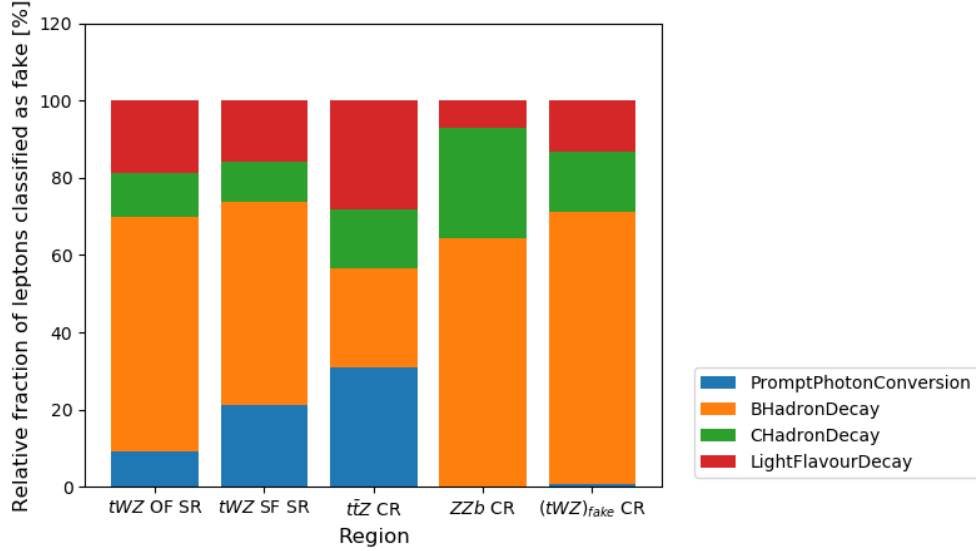


Figure 4.26: The relative dominance of the different classifications for fake leptons (classified by the IFF truth classified) in each region, is shown. The relative dominance of leptons classified as fakes, as a fraction of the total number of fake leptons (in each region), is shown on the y-axis. The different signal and control regions are shown on the x-axis. The IFF truth classification of the leptons are shown in the legend and correspond to the different coloured stacked histograms.

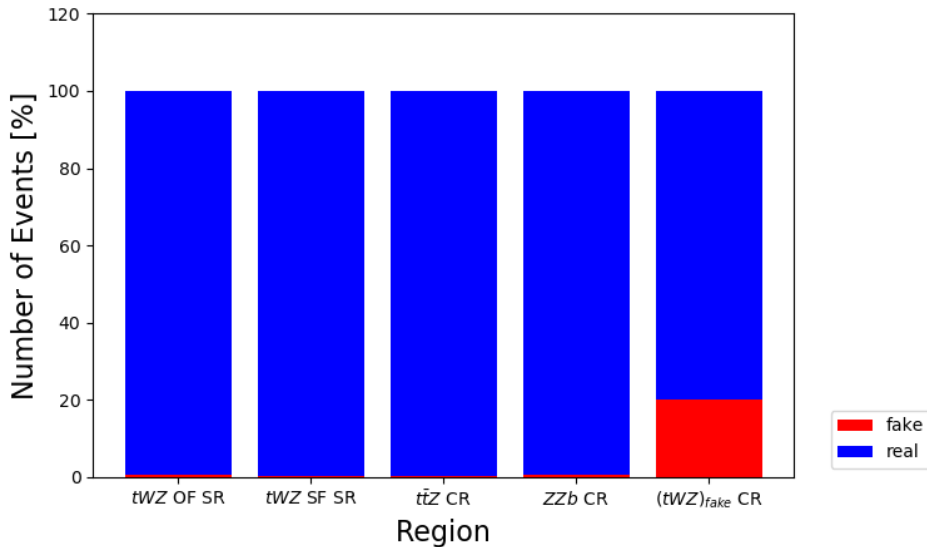


Figure 4.27: The percentage of fake and real $t\bar{t}Z$ events which pass our selection criteria, in each region, is shown. The relative number of fake and real events (in % of the total number of events in the nominal and fake $t\bar{t}Z$ background samples) is shown on the y-axis. The different signal and control regions are shown on the x-axis. The blue and red histograms represent the percentage of real and fake events (out of the total number of events in the nominal and fake $t\bar{t}Z$ background samples), respectively.

800
 801 Two different BDTs were used, the first aims to discriminate between tWZ events and its major backgrounds,
 802 $t\bar{t}Z$ and ZZ . The second aims to discriminate between ℓb systems which originate from the decay of a top quark
 803 ($t \rightarrow W(\rightarrow \ell\nu)b$) and those which do not. We refer to these two BDTs as an **event-level** and an **object-level**
 804 classifier respectively. The discriminator output from the object-level BDT can be converted to a variable which
 805 can then be used as input to the event-level BDT.

806 4.7.1 Object-level BDT

807 The object-level BDT was trained on a $t\bar{t}$ sample with a baseline selection of exactly 1 tight lepton with $p_T > 28$
 808 GeV. Additionally, jets in this sample are required to have $p_T > 20$ GeV. b -tagged jets are identified by the
 809 77% DL1r working point. These baseline selections were chosen to mimic those used in the event selection of
 810 the analysis (outlined in Table 4.3). We opted to use this disjoint $t\bar{t}$ sample as to avoid resorting to use our MC
 811 samples used in the rest of the analysis which is heavily limited on statistics, therefore maximizing the amount of
 812 MC statistics used in the fitting procedure and the training of the event-level BDT.
 813

814 The signal class is defined to consist of reconstructed ℓb systems (defined as the sum of the 4-vectors of the
 815 lepton and b -jet) coming from top quarks which are well matched to their truth counterparts. In particular, we
 816 require that ΔR between the reconstructed and truth ℓb system is less than 0.05. We additionally require that the
 817 reconstructed lepton and the truth top have charges with the same sign (since $t \rightarrow b\ell^+\bar{\nu}_\ell$ and $\bar{t} \rightarrow \bar{b}\ell^-\nu_\ell$). The
 818 background class is defined to consist of all reconstructed ℓb systems which fail to pass the criteria for ℓb systems
 819 which are labelled as signal. These definitions for the signal and background classes ensure that the signal class
 820 consists of mostly ℓb systems originating from tops and the background class consists of mostly ℓb systems which
 821 do not originate from a top decay.
 822

823 Different observables corresponding to an ℓb system were used as input to training. The optimum values
 824 for the hyper-parameters used were determined by training the BDT with a range of different values for the
 825 hyper-parameters and choosing the set of values which maximized the mean accuracy (based off 5 fold kfold
 826 cross-validation). This method is more commonly referred to as hyper-parameter optimisation or tuning. After
 827 hyper-parameter optimisation, the mean accuracy of each fold increased from 0.76 to 0.77 ($\sim 1\%$ increase). Input
 828 features can be assigned a score called *variable importance*, based on their usefulness on predicting a target
 829 variable (in this case, a signal or background event). The variable importance for any given variable was obtained
 830 by computing the mean accuracy of the model, removing the variable from training, retraining the model and
 831 computing the mean accuracy of this new model. The difference between mean accuracies of the unaltered model
 832 and the retrained model (after removal of the variable) gives us the variable importance of the variable of interest.
 833 This method returns positive values for variables which increase the mean accuracy of the model and negative
 834 values for variables which decrease the mean accuracy of the model. Variables with negative variable importances
 835 were completely removed from training.

836 In Table 4.6, the variables used in training the object-level BDT are shown.

Observable	Description
$m(\ell b)$	Invariant mass of the ℓb system
$p_T(\ell b)$	p_T of the ℓb system
$\Delta\eta(\ell, b)$	$\Delta\eta$ between the ℓ and b -tagged jet
$\Delta\phi(\ell, b)$	$\Delta\phi$ between the ℓ and b -tagged jet
$\Delta R(\ell, b)$	ΔR between the ℓ and b -tagged jet

Table 4.6: A list of the observables used in the object-level BDT, ordered by importance (descending, top to bottom) is shown.

837
 838 In Figure 4.28, normalised distributions of the signal and background classes for the training set of all variables
 839 used in the object-level BDT are show.
 840 Overall the BDT input variables show a large amount of discrimination.

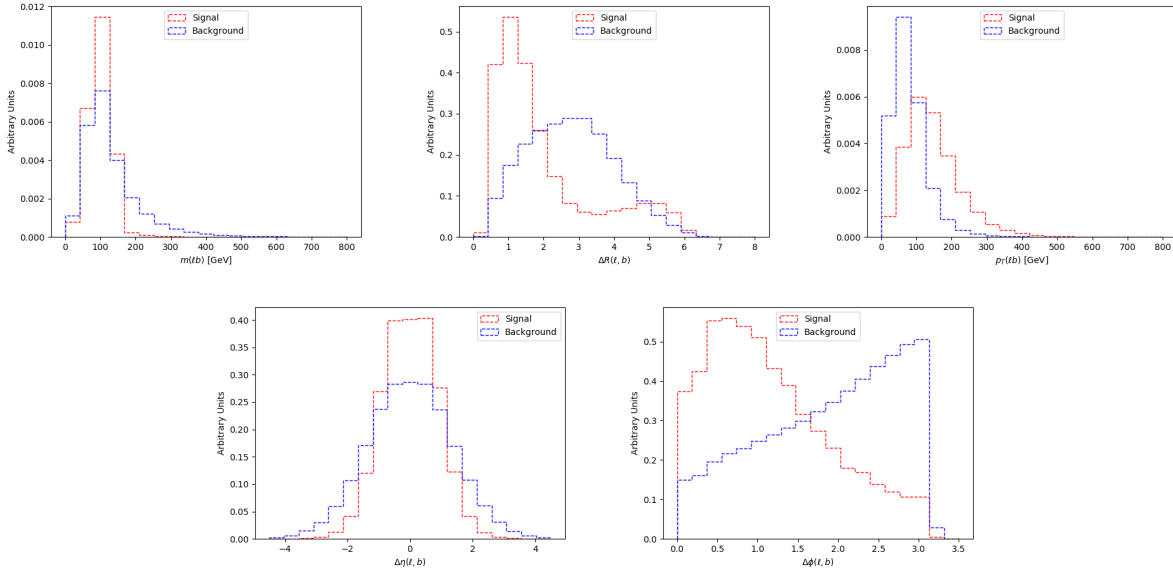


Figure 4.28: Normalised distributions of the signal and background classes for the training set of all variables used in the object-level BDT (ordered from top left to bottom right via decreasing importance) are shown. The red and blue dotted lined histograms represent the signal and background classes events (normalised to an area of 1), respectively. The variable used in training is shown on the x-axis. The y-axis shows the relative number of events for the signal and background classes (in arbitrary units). **From top left to bottom right:** Invariant mass of the lb system. ΔR between the l and b -tagged jet. The p_T of the lb system. $\Delta\eta$ between the l and b -tagged jet. $\Delta\phi$ between the l and b -tagged jet.

841
842 We can check the modelling of the input variables to the object-level BDT by studying the agreement between data
843 and simulation in the $t\bar{t}Z$ CR. In Figure 4.29, MC predictions for the input variables to the object-level BDT in
844 the $t\bar{t}Z$ CR are shown.

845 Overall, there is good agreement between data and simulation for the input variables to the object-level BDT in
846 the $t\bar{t}Z$ CR. This suggests that the input variables to the object-level BDT are well-modelled and are reasonable
847 to include as inputs to the object-level BDT.

848 A final check can be done to study the similarity of the lb systems present in the alternative $t\bar{t}$ sample which we use
849 for training the object-level BDT, and the lb systems which we aim to identify using the object-level BDT. More
850 specifically, we want to ensure that the lb systems in the alternative $t\bar{t}$ sample are similar enough to those in the
851 tWZ and $t\bar{t}Z$ samples (see Table 4.1). In Figure 4.30, normalised distributions of input variables to the object-level
852 BDT in the alternative $t\bar{t}$, tWZ and $t\bar{t}Z$ samples, are shown.

853 The distributions of the input variables to the object-level classifier, for the three samples, are similar and show no
854 large deviations between one another. This tells us that the lb systems which we use in training are similar enough
855 to those we aim to identify using the classifier. The use of the alternative $t\bar{t}$ sample for training the object-level
856 classifier is therefore sufficient for this analysis.

858
859 In Table 4.7, the hyper-parameters used in the object-level BDT is shown.
860 The number of events used in training for the signal and background classes were 49871 and 384152 respectively.
861 Imbalanced datasets can cause ML classifiers to ignore small classes while concentrating on classifying large classes
862 more accurately, which may result in the trained classifier performing sub-optimally. In order to correct this dataset
863 imbalance, we ensure that the relative weighting of each event is such that the sum of the signal weights is equal
864 to the sum of the background weights. In Figure 4.31 the normalised histograms of the training and test sets
865 (extracted from fold 5 from a 5 fold kfold cross validation) for signal and background is shown.

866 We can see that the shapes of the training and test sets for both signal and background are very similar. This
867 is a good indicator that no over-training occurred. Another over-training check is performed using 5 fold kfold
868 cross validation. We ensure that the variance of the mean accuracy of each folds' test set in cross validation is

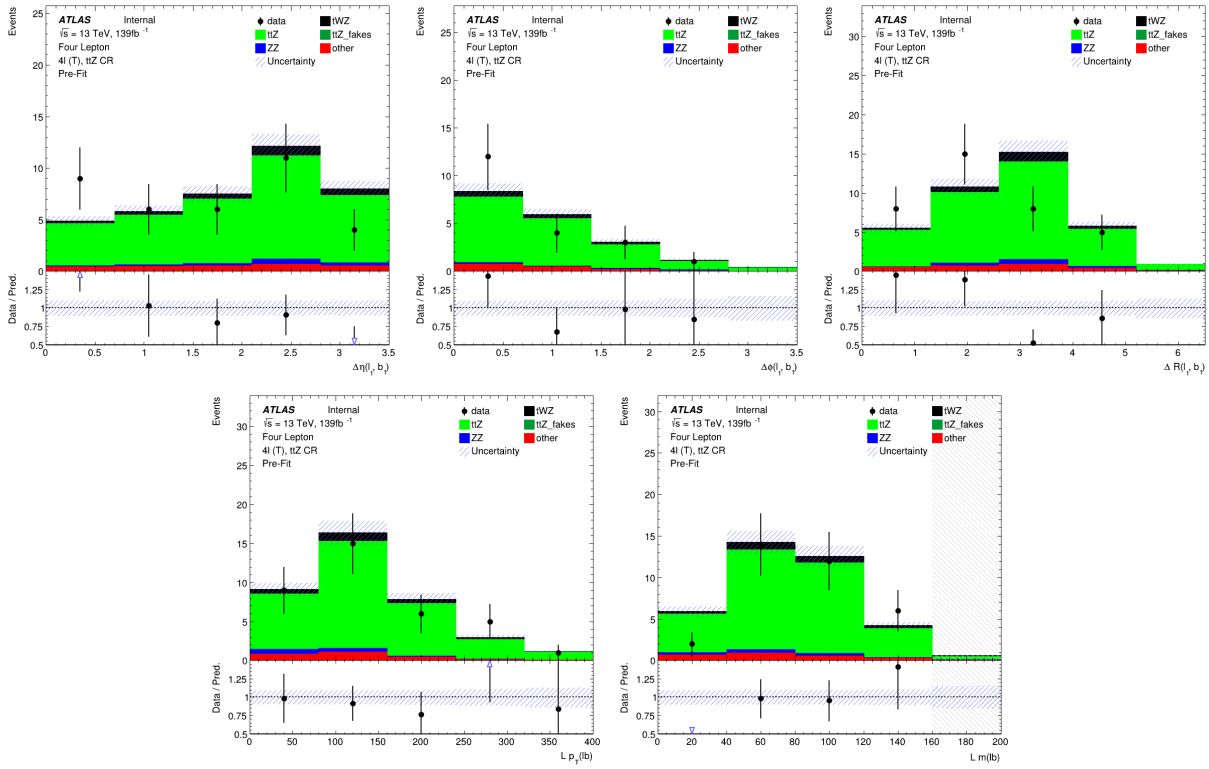


Figure 4.29: Pre-fit distributions of variables used as input to the object-level BDT (ordered from top left to bottom right via decreasing importance), in the $t\bar{t}Z$ CR, are shown. The data is given by the black points and the MC predictions for each process are given by the histograms. The vertical lines on the data points represent the total uncertainty in the data and the blue diagonal lined bands represent the total MC uncertainty. The lower panel in each plot shows the ratios of the data to the theoretical predictions. Bins with a $\frac{\text{signal}}{\text{background}}$ yield greater than 0.1 are kept blinded. Blinded bins are shaded with black diagonal lines and their data points are omitted. **From top left to bottom right:** $\Delta\eta$ between the lepton and b -jet of the leading ℓb system. $\Delta\phi$ between the lepton and b -jet of the leading ℓb system. ΔR between the lepton and b -jet of the leading ℓb system. p_T of the leading ℓb system. Mass of the leading ℓb system.

Hyper-parameter	Value	Description
loss	deviance	The loss function to be optimised
criterion	friedman_mse	The function used to measure the quality of a split
n_estimators	200	The number of boosting stages to perform
learning_rate	0.1	The step size at each iteration during optimisation
max_depth	6	The maximum depth of the individual regression estimators
min_samples_split	2	The minimum number of samples (events) required to split an internal node
min_samples_leaf	1	The minimum number of samples (events) required to be at a leaf node
validation_fraction	0.1	The proportion of training data to set aside as validation set for early stopping
n_iter_no_change	20	Training terminates when the validation score (determined by the validation set) does not improve in all of the previous

Table 4.7: A list of the hyper-parameters used in the object-level BDT is shown. Hyperparameters not listed in this table use the default values as stated in the Scikit-learn Documentation[61].

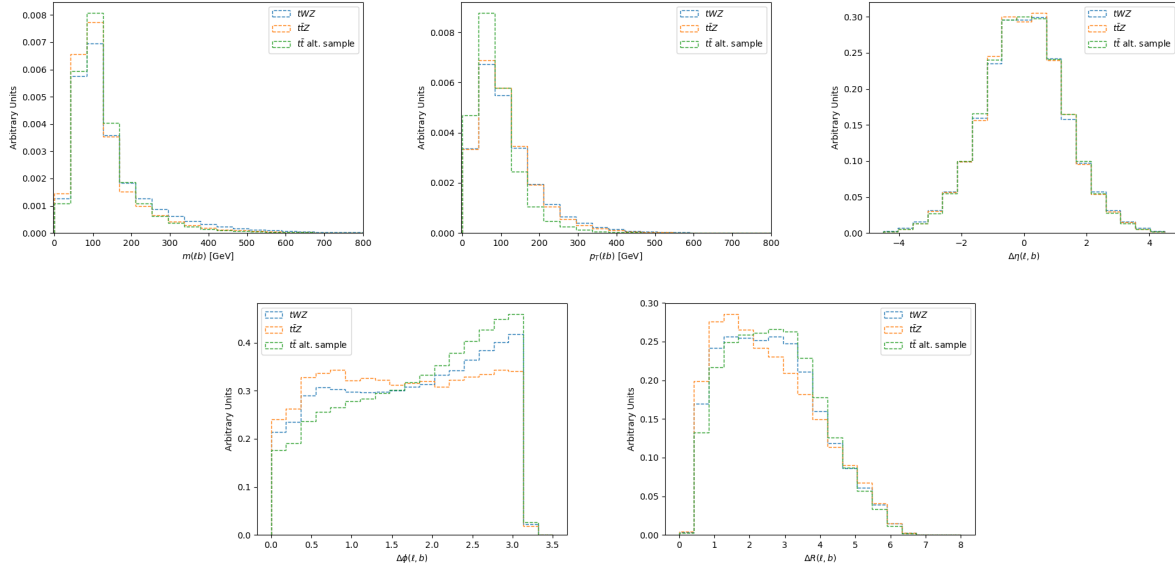


Figure 4.30: Normalised distributions of input variables (ordered from top left to bottom right via decreasing importance) to the object-level BDT in the alternative $t\bar{t}$, tWZ and $t\bar{t}Z$ samples, are shown. The green, blue and orange dotted lined histograms represent events from the alternative $t\bar{t}$, tWZ and $t\bar{t}Z$ samples (normalised to an area of 1), respectively. The variable used in training is shown on the x-axis. The y-axis shows the relative number of events (in arbitrary units). **From top left to bottom right:** Invariant mass of the ℓb system. ΔR between the ℓ and b -tagged jet. The p_T of the ℓb system. $\Delta\eta$ between the ℓ and b -tagged jet. $\Delta\phi$ between the ℓ and b -tagged jet.

substantially small. This indicates that fluctuations in features from different training sets are not learnt by the classifier. For the object-level classifier, a variance of 3.24×10^{-7} was calculated for the mean accuracies of each folds' test set in cross validation, providing further evidence that no over-training occurred.

The output from the object-level BDT was used to construct a variable to be used as input to the event-level BDT. The event-level BDT aims to discriminate between tWZ and our most prominent background, $t\bar{t}Z$. We therefore aim to construct a variable from the output of the object-level BDT which discriminates well between tWZ and $t\bar{t}Z$. Since tWZ events contain one top quark and $t\bar{t}Z$ events contain two top quarks, we expect that tWZ events have one ℓb combination which scores well and we expect that $t\bar{t}Z$ events have two ℓb combinations which score well. We construct a variable, $BDTScore(\frac{\text{Best}}{\text{2nd Best}})$, which takes the ratio of the scores of the top scoring ℓb system to the 2nd best scoring ℓb system. We expect this variable to be large for tWZ events and closer to one for $t\bar{t}Z$ events, therefore providing discrimination between tWZ and $t\bar{t}Z$.

In Figure 4.32, normalised distributions of the signal and total background of the $BDTScore(\frac{\text{Best}}{\text{2nd Best}})$ variable in the tWZ OF SR, tWZ SF SR and $t\bar{t}Z$ CR are shown. There doesn't seem to be a large amount of discrimination between signal and background for $BDTScore(\frac{\text{Best}}{\text{2nd Best}})$ in either of the above regions. We do however see some discrimination in bins near a value of 1, where the number of background events exceed the number of signal events, which is what we expect. This effect is slightly more exaggerated in the $t\bar{t}Z$ CR than the tWZ SRs. This can be explained since we expect to have a larger proportion of $t\bar{t}Z$ events (events with two ℓb systems) in the $t\bar{t}Z$ CR. An excess of signal events (compared to background) are observed at larger values. This is to be expected, since these events correspond to a lower score by the ℓb classifier on the 2nd best scoring ℓb system in the event. The 2nd best scoring ℓb system in a tWZ event is expected to be low, since there is only one ℓb system originating from a top. Despite the apparent lack of discrimination between signal and background events from this variable, when used as input to training in the event-level BDT (see Section 4.7.2), improves the mean accuracy of the classifier. The tells us that the event-level BDT is taking advantage of the discrimination between signal and background present in the $BDTScore(\frac{\text{Best}}{\text{2nd Best}})$ variable.

In an attempt to optimise the performance of the object-level BDT, we aim to train on signal events which are as

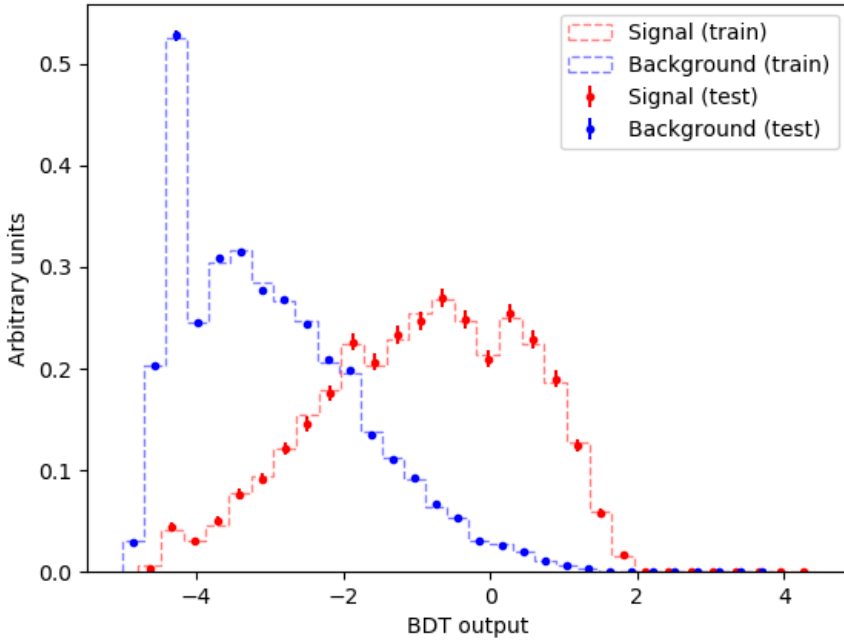


Figure 4.31: Normalised histograms of the object-level BDT discriminator output from the signal and background classes for the training and test sets from the 5th fold in a 5 fold kfold cross validation is shown. The output of the object-level BDT is shown on the x-axis and the relative number of events (in arbitrary units) is shown on the y-axis. The training set for the signal class is shown by the red dotted histogram. The test set for the signal class is shown by the red points, with the total uncertainty represented by the vertical error bars. The training set for the background class is shown by the blue dotted histogram. The test set for the background class is shown by the blue points, with the total uncertainty represented by the vertical error bars.

pure in ℓb systems originating from top quarks, as possible. Similarly, we aim to train on background events which are as pure in ℓb systems not originating from top quarks, as possible. This is done by studying the distribution of ΔR between the reconstructed ℓb system and the truth ℓb system ($\Delta R((lb)_{reco}, (lb)_{truth})$), and excluding ℓb systems from training which are moderately matched in ΔR to their truth counterparts, leaving well matched ℓb systems being labelled as signal and badly matched ℓb systems labelled as background. We call the ΔR range where ℓb systems are excluded from training, the exclusion region. In Figure 4.33, the distribution of ΔR between the reconstructed ℓb system and the truth ℓb system ($\Delta R((lb)_{reco}, (lb)_{truth})$) in the alternative $t\bar{t}$ sample, along with the exclusion region, is shown.

A large number of reconstructed ℓb systems have $\Delta R((lb)_{reco}, (lb)_{truth})$ at values near 0. These are matched (in ΔR) extremely well to truth ℓb systems originating from top quarks. We therefore define our exclusion region to be between $0.05 < \Delta R((lb)_{reco}, (lb)_{truth}) < 3.0$, such that all reconstructed ℓb systems with $\Delta R((lb)_{reco}, (lb)_{truth}) \leq 0.05$ are labelled as signal and reconstructed ℓb systems with $\Delta R((lb)_{reco}, (lb)_{truth}) \geq 3.0$ are labelled as background. All reconstructed ℓb systems with $0.05 < \Delta R((lb)_{reco}, (lb)_{truth}) < 3.0$ are excluded from training.

The performance of the object-level BDT with and without the exclusion region can be compared by studying the discrimination between signal and background events in the $BDTScore(\frac{\text{Best}}{\text{2nd Best}})$ variable (object-level output converted to an event-level variable to be used in the event-level BDT) for both object-level BDTs. In Figure 4.34, normalised distributions of $BDTScore(\frac{\text{Best}}{\text{2nd Best}})$ using the object-level BDT without the exclusion region (see Figure 4.33) for the tWZ OF SR, tWZ SF SR and $t\bar{t}Z$ CR are shown.

The amount of discrimination can be quantified by the separation metric, which gives the percentage of the total area of the distributions which do not overlap. A value of 1 indicates that the distributions are fully separated (no overlap) and a value of 0 indicates that the distributions have no separation (fully overlapped). We can compare the separation metrics between the $BDTScore(\frac{\text{Best}}{\text{2nd Best}})$ variable in the tWZ OF SR, tWZ SF SR and $t\bar{t}Z$ CR for the ℓb classifier with (Figure 4.32) and without (Figure 4.34) the exclusion region by taking the absolute difference

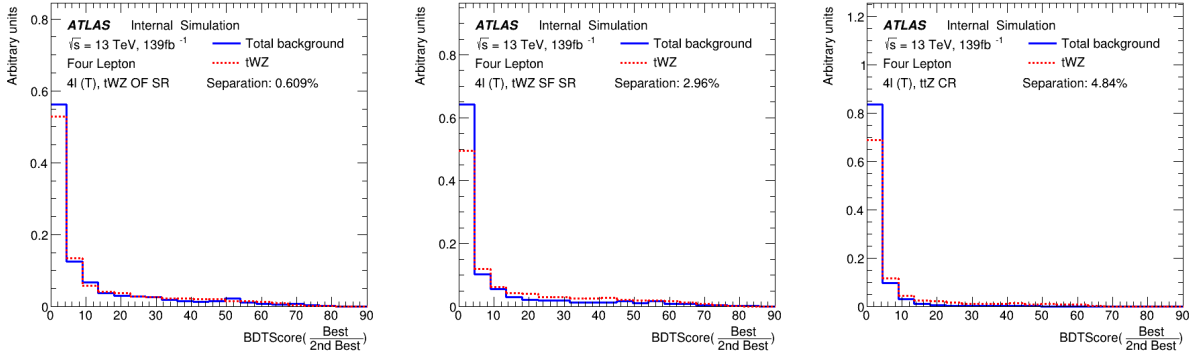


Figure 4.32: Normalised distributions of the signal and total background of the $\text{BDTScore}(\frac{\text{Best}}{\text{2nd Best}})$ variable in the tWZ OF SR, tWZ SF SR and $t\bar{t}Z$ CR are shown (left to right). The dotted red and solid blue lines represent the distributions (normalised to an area of 1) of the signal and total background events respectively. The x-axis shows the $\text{BDTScore}(\frac{\text{Best}}{\text{2nd Best}})$ and the y-axis show the relative number of events (in arbitrary units).

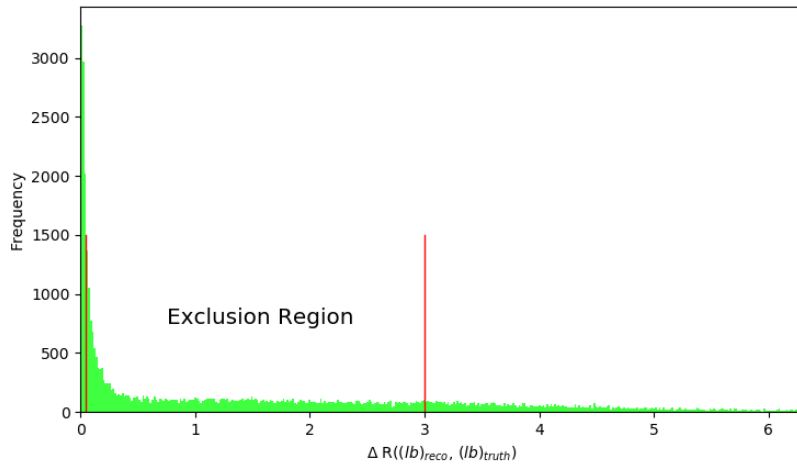


Figure 4.33: The distribution of ΔR between the reconstructed ℓb system and the truth ℓb system ($\Delta R((lb)_{reco}, (lb)_{truth})$) in the alternative $t\bar{t}$ sample, along with the exclusion region, is shown. The ΔR distribution is shown in green. ΔR between the reconstructed ℓb system and the truth ℓb system ($\Delta R((lb)_{reco}, (lb)_{truth})$) is shown on the x-axis. The bin frequency is shown on the y-axis. The exclusion region is shown between the vertical red lines situated at $\Delta R((lb)_{reco}, (lb)_{truth}) = 0.05$ and $\Delta R((lb)_{reco}, (lb)_{truth}) = 3.0$. Reconstructed ℓb systems with $\Delta R((lb)_{reco}, (lb)_{truth}) \leq 0.05$ are labelled as signal and reconstructed ℓb systems with $\Delta R((lb)_{reco}, (lb)_{truth}) \geq 3.0$ are labelled as background.

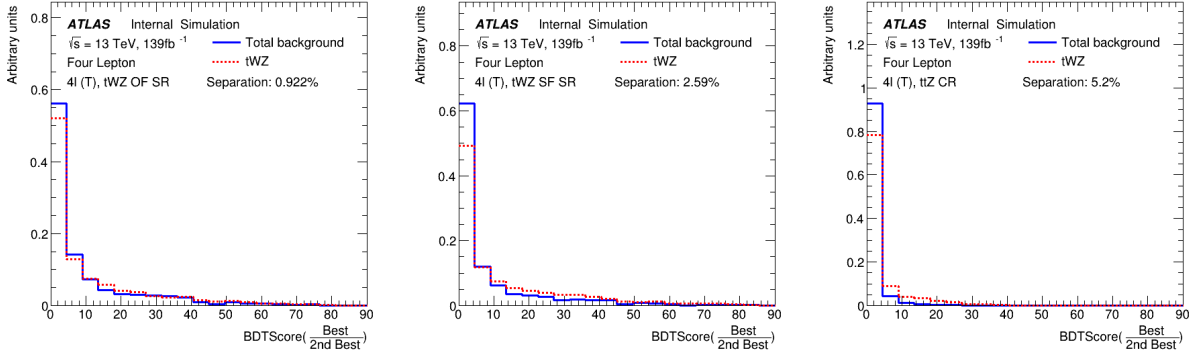


Figure 4.34: Normalised distributions of $\text{BDTScore}(\frac{\text{Best}}{\text{2nd Best}})$ using the object-level BDT without the exclusion region (see Figure 4.33) for the tWZ OF SR, tWZ SF SR and $t\bar{Z}$ CR are shown (left to right). The dotted red and solid blue lines represent the distributions (normalised to an area of 1) of the signal and total background events respectively. The x-axis shows the $\text{BDTScore}(\frac{\text{Best}}{\text{2nd Best}})$ and the y-axis show the relative number of events (in arbitrary units).

between the two values in each region. The differences are 0.31%, 0.37% and 0.36% for the tWZ OF SR, tWZ SF SR and $t\bar{Z}$ CR, respectively. These differences are minimal and the object-level BDT with the exclusion region outperforms the object-level BDT without the exclusion region in the tWZ SF SR. Due to the small differences in performance between the two BDTs, for simplicity, we ultimately chose to keep the BDT with the exclusion region.

4.7.2 Event-level BDT

The event-level BDT was trained on 50% of the tWZ MC sample's events for the signal class and similarly, 50% of the $t\bar{Z}$ and ZZ MC sample's events were used for the background class. The samples we train on are individual events, with the features being carefully chosen observables. These observables are chosen on the basis that they are somewhat uncorrelated from one another and show a relatively large amount of separation power between tWZ and $t\bar{Z}$. Similarly to the object-level BDT, the optimum values for the hyper-parameters used were determined via hyper-parameter optimisation. After hyperparameter optimisation, the mean accuracy of each fold (determined from 5 fold kfold cross validation) increased from 0.72 to 0.74 ($\sim 3\%$ increase). The variable importance of each variable was computed in the same way as described for the object-level BDT (See Section 4.7.1).

In Table 4.8, the variables used in training the event-level BDT are shown.

Observable	Description
$2\nu\text{SM}$	Maximum weight from the $2\nu\text{SM}$ algorithm (See Section 4.8)
HT	Scalar sum of jet p_T
LT	Scalar sum of lepton p_T
$\sum p_T(b-jet)$	Scalar sum of b-tagged jet p_T
$\text{BDTScore}(\frac{\text{Best}}{\text{2nd Best}})$	Ratio of the top scoring ℓb system to the 2nd best scoring ℓb system from the output of the object-level BDT (ℓb classifier)
$\Delta\eta(\ell_{1,\text{Non-}Z}, \ell_{2,\text{Non-}Z})$	$\Delta\eta$ between the two leptons, not coming from a Z candidate

Table 4.8: A list of the observables used in the event-level BDT, ordered by importance (descending, top to bottom) is shown.

In Figure 4.35, normalised distributions of the signal and background classes for the training set of all variables used in the event-level BDT are shown.

Overall the BDT input variables show a reasonable amount of discrimination. In particular the output weight from the $2\nu\text{SM}$ algorithm shows the most discrimination. When determining which variables to use in training the event-level BDT, the output weight from $2\nu\text{SM}$ was shown to provide the most sizeable boost in performance of the BDT. Surprisingly, the least important variable, $\Delta\phi$ between the non- Z lepton system (leptons not originating from a Z -candidate) and the leading b -tagged jet, seem to discriminate well between signal and background. A possible explanation for its low ranking importance is due to it being relatively highly correlated with many of the other input variables.

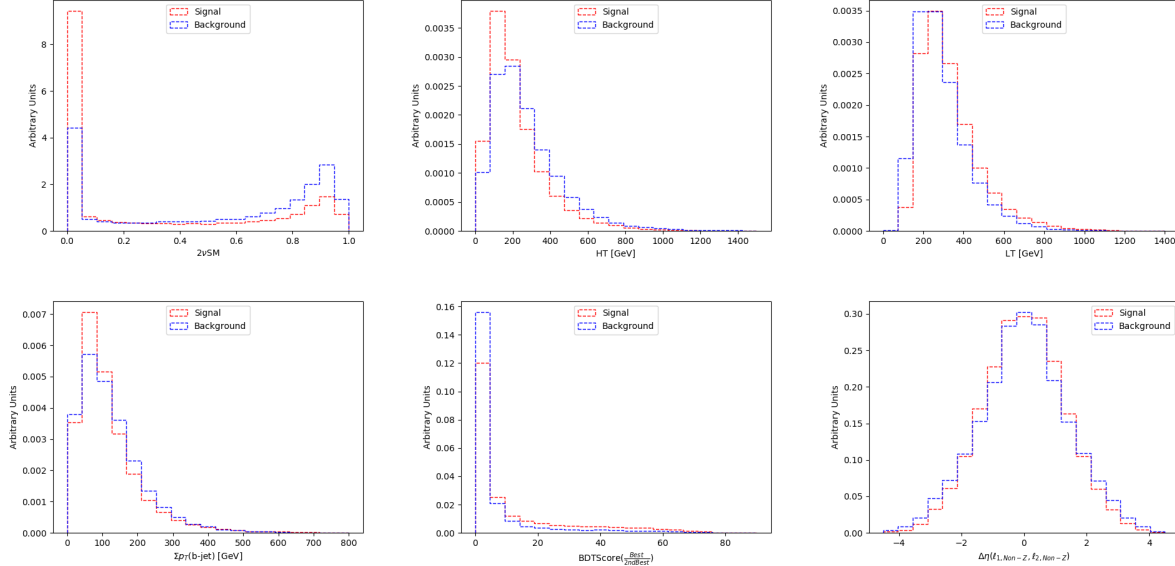


Figure 4.35: Normalised distributions of the signal and background classes for the training set of all variables used in the event-level BDT (ordered from top left to bottom right via decreasing importance) are shown. The red and blue dotted lined histograms represent the signal and background classes events (normalised to an area of 1), respectively. The variable used in training is shown on the x-axis. The y-axis shows the relative number of events for the signal and background classes (in arbitrary units). **From top left to bottom right:** Output weight from the $2\nu\text{SM}$ algorithm (See Section 4.8). Scalar sum of jet p_T . Scalar sum of lepton p_T . Sum of b -tagged jet p_T . Ratio of the top scoring ℓb system to the 2nd best scoring ℓb system from the output of the object-level BDT (See Section 4.7.1). $\Delta\eta$ between the two leptons, not coming from a Z candidate.

946 We can check the modelling of the input variables to the event-level BDT by referring to the pre-fit distributions
 947 of data and simulation in the control regions. Note that certain variables which are ill-defined in certain regions
 948 (e.g. $\Delta\eta(\ell_{1,\text{Non}-Z}, \ell_{2,\text{Non}-Z})$ in the ZZb CR, as all leptons originate from a b -jet in this region) will not be shown.
 949

950 In Figure 4.36, MC predictions for the input variables to the event-level BDT in the $t\bar{t}Z$ CR are shown.
 951 In Figure 4.37, MC predictions for the input variables to the event-level BDT in the ZZb CR are shown.
 952 In Figure 4.38, MC predictions for the input variables to the event-level BDT in the $(tWZ)_{\text{fake}}$ CR are shown.
 953 Overall, the agreement between data and simulation for the input variables to the event-level BDT is good.
 954 Therefore, these variables are well-modelled and reasonable to include as inputs to the event-level BDT.
 955

In Table 4.9, the hyper-parameters used in the event-level BDT are shown.

Hyper-parameter	Value	Description
loss	deviance	The loss function to be optimised
criterion	friedman_mse	The function used to measure the quality of a split
n_estimators	200	The number of boosting stages to perform
learning_rate	0.1	The step size at each iteration during optimisation
max_depth	6	The maximum depth of the individual regression estimators
min_samples_split	2	The minimum number of samples (events) required to split an internal node
min_samples_leaf	1	The minimum number of samples (events) required to be at a leaf node
validation_fraction	0.1	The proportion of training data to set aside as validation set for early stopping
n_iter_no_change	20	Training terminates when the validation score (determined by the validation set) does not improve in all of the previous

Table 4.9: A list of the hyper-parameters used in the event-level BDT is shown. Hyperparameters not listed in this table use the default values as stated in the Scikit-learn Documentation[61].

956 Since we are training on $t\bar{t}Z$ and ZZ events for the background class, we ensure that the relative weighting of these
 957 events are such that they mimic the amount of $t\bar{t}Z$ and ZZ expected to be present in the regions where we aim to
 958 use the BDT discriminator (tWZ SRs and $t\bar{t}Z$ CR). This is done by applying normalization weights to each event,
 959

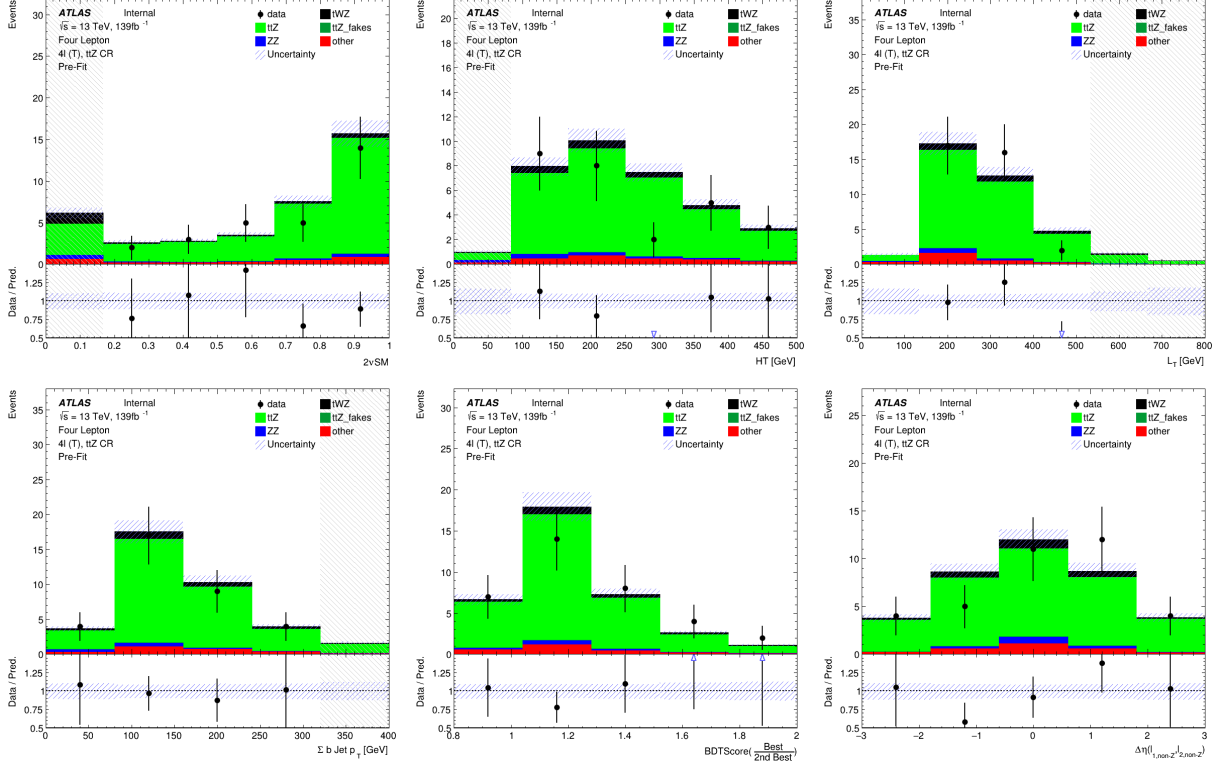


Figure 4.36: Pre-fit distributions of variables used as input to the event-level BDT (ordered from top left to bottom right via decreasing importance), in the $t\bar{t}Z$ CR, are shown. The data is given by the black points and the MC predictions for each process are given by the histograms. The vertical lines on the data points represent the total uncertainty in the data and the blue diagonal lined bands represent the total MC uncertainty. The lower panel in each plot shows the ratios of the data to the theoretical predictions. Bins with a $\frac{\text{signal}}{\text{background}}$ yield greater than 0.1 are kept blinded. Blinded bins are shaded with black diagonal lines and their data points are omitted. **From top left to bottom right:** Output weight from the 2 ν SM algorithm (See Section 4.8). Scalar sum of jet p_T . Scalar sum of lepton p_T . Sum of b -tagged jet p_T . Ratio of the top scoring ℓb system to the 2nd best scoring ℓb system from the output of the object-level BDT (See Section 4.7.1). $\Delta\eta$ between the two leptons, not coming from a Z candidate.

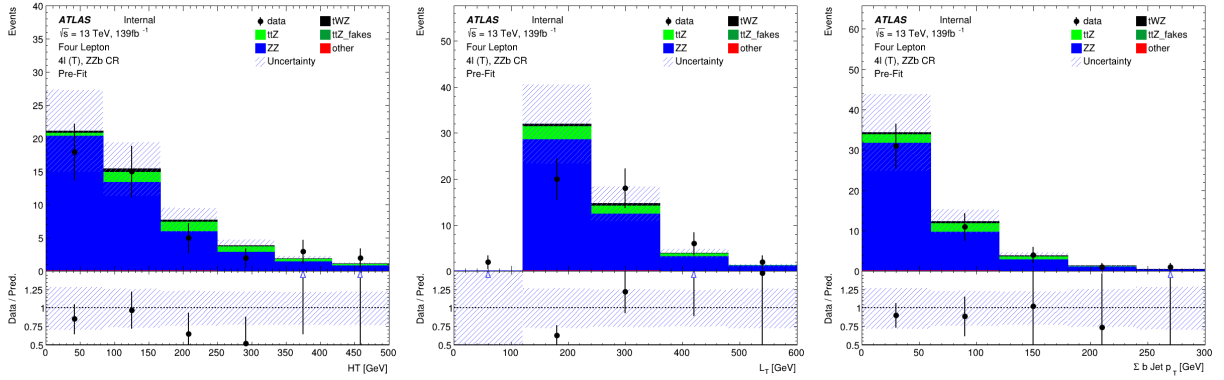


Figure 4.37: Pre-fit distributions of variables used as input to the event-level BDT (ordered from top left to bottom right via decreasing importance), in the ZZb CR, are shown. The data is given by the black points and the MC predictions for each process are given by the histograms. The vertical lines on the data points represent the total uncertainty in the data and the blue diagonal lined bands represent the total MC uncertainty. The lower panel in each plot shows the ratios of the data to the theoretical predictions. Bins with a $\frac{\text{signal}}{\text{background}}$ yield greater than 0.1 are kept blinded. Blinded bins are shaded with black diagonal lines and their data points are omitted. **From left to right:** Scalar sum of jet p_T . Scalar sum of lepton p_T . Sum of b -tagged jet p_T .

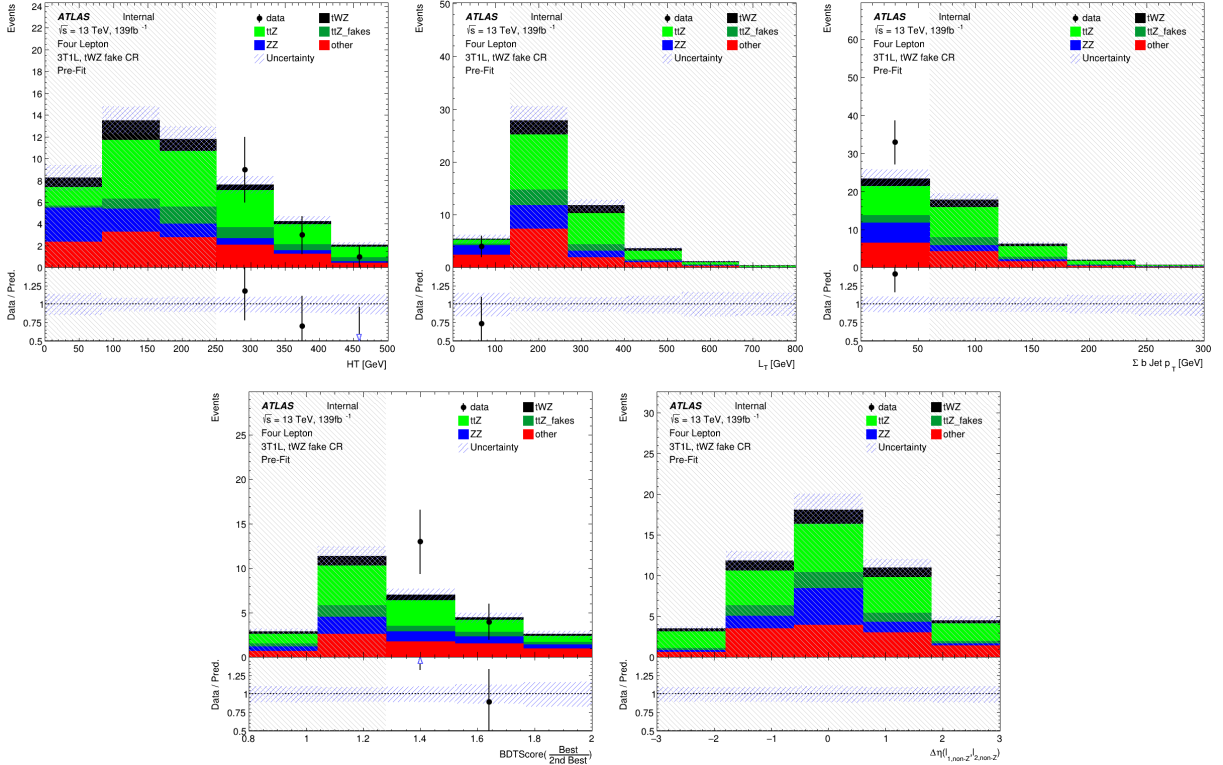


Figure 4.38: Pre-fit distributions of variables used as input to the event-level BDT (ordered from top left to bottom right via decreasing importance), in the $(tWZ)_{\text{fake}}$ CR, are shown. The data is given by the black points and the MC predictions for each process are given by the histograms. The vertical lines on the data points represent the total uncertainty in the data and the blue diagonal lined bands represent the total MC uncertainty. The lower panel in each plot shows the ratios of the data to the theoretical predictions. Bins with a $\frac{\text{signal}}{\text{background}}$ yield greater than 0.1 are kept blinded. Blinded bins are shaded with black diagonal lines and their data points are omitted. **From top left to bottom right:** Output weight from the $2\nu\text{SM}$ algorithm (See Section 4.8). Scalar sum of jet p_T . Scalar sum of lepton p_T . Sum of b -tagged jet p_T . Ratio of the top scoring ℓb system to the 2nd best scoring ℓb system from the output of the object-level BDT (See Section 4.7.1). $\Delta\eta$ between the two leptons, not coming from a Z candidate.

960 defined as,

$$W = \frac{\sigma \mathcal{L} \text{weight(MC)}}{\text{totalWeight(MC)}} \quad (4.2)$$

961 where σ is the cross section of the process, \mathcal{L} is the integrated luminosity, weight(MC) is the weight assigned to
962 the event by the MC generator and totalWeight(MC) is the sum of those weights for all the generated events.

963 The number of events used in training for the signal and background classes were 41066 and 22608 respectively.
964 Similarly to the object-level BDT, there is a dataset imbalance. We correct this imbalance (in the same way as
965 before with the object-level BDT) by ensuring that the relative weighting of each event is such that the sum of the
966 signal weights is equal to the sum of the background weights.

967 In Figure 4.40 the normalised histograms of the training and test sets (extracted from fold 5 from a 5 fold kfold
968 cross validation) for signal and background is shown.

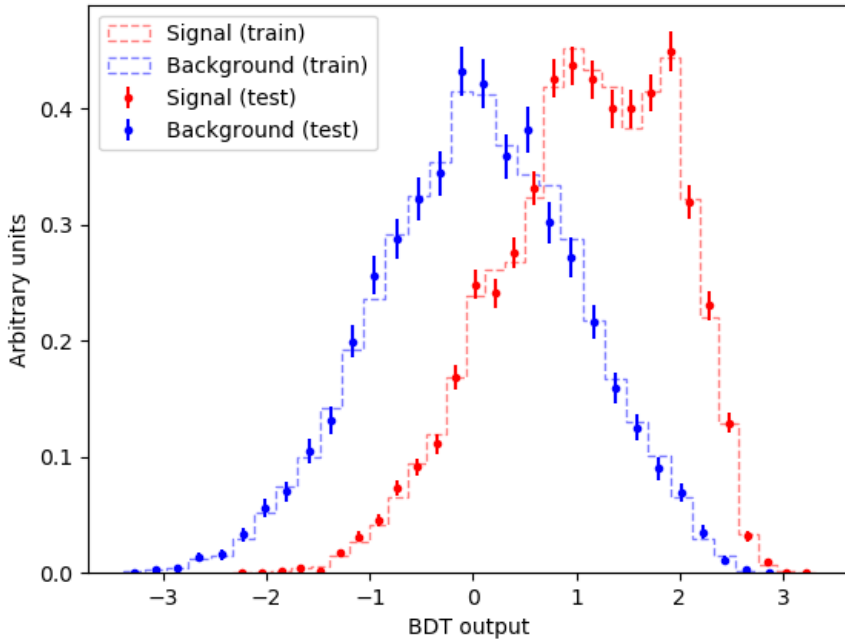


Figure 4.39: Normalised histograms of the event-level BDT discriminator output from the signal and background classes for the training and test sets from the 5th fold in a 5 fold kfold cross validation are shown. The output of the event-level BDT is shown on the x-axis and the relative number of events (normalised to have an area of 1, in arbitrary units) is shown on the y-axis. The training set for the signal class is shown by the red dotted histogram. The test set for the signal class is shown by the red points, with the total uncertainty represented by the vertical error bars. The training set for the background class is shown by the blue dotted histogram. The test set for the background class is shown by the blue points, with the total uncertainty represented by the vertical error bars.

970 We can see that the shapes of the training and test sets for both signal and background are very similar. This is
971 a good indicator that no over-training occurred. As with the object-level BDT, we perform another over-training
972 check, by ensuring that the variance of the mean accuracy of each folds' test set in a 5 fold kfold cross validation
973 is substantially small. This indicates that fluctuations in features from different training sets are not learnt by the
974 classifier. For the event-level classifier, a variance of 0.00026 was calculated for the mean accuracies of each folds'
975 test set in cross validation, providing further evidence that no over-training occurred.

977 In Figure ??, normalised distributions of the signal and total background of the event-level BDT discriminator
978 output in the tWZ OF SR, tWZ SF SR and $t\bar{t}Z$ CR, are shown.

979 The event-level BDT discriminates well between signal and background events in the tWZ OF SR, tWZ SF SR
980 and $t\bar{t}Z$ CR, with separations of 8.98%, 10.6% and 20.6%, respectively.

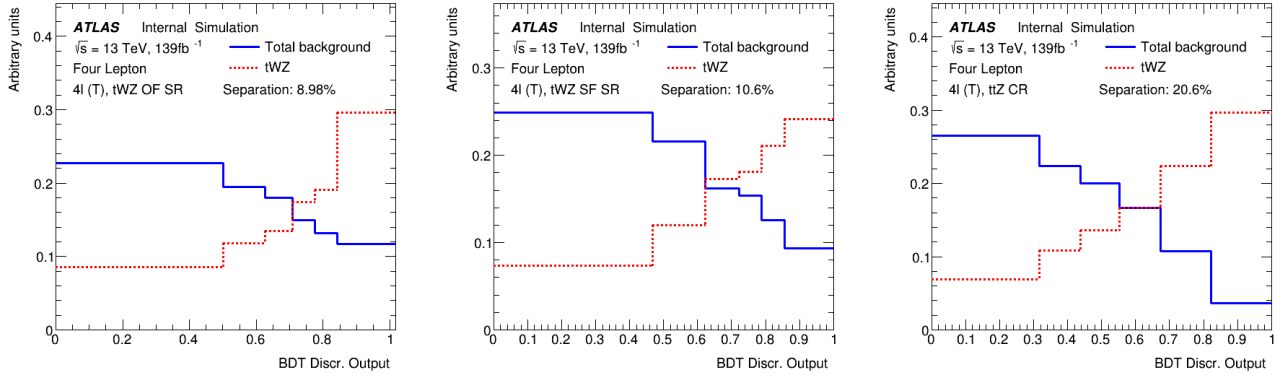


Figure 4.40: Normalised distributions of the signal and total background of the event-level BDT discriminator output in the tWZ OF SR, tWZ SF SR and $t\bar{t}Z$ CR are shown (left to right). The dotted red and solid blue lines represent the distributions (normalised to an area of 1) of the signal and total background events respectively. The x-axis shows the event-level BDT discriminator output and the y-axis shows the relative number of events (in arbitrary units).

4.8 Two Neutrino Scanning Method (2ν SM) Algorithm

The Two Neutrino Scanning Method (2ν SM) algorithm¹ [50, 49] aims to reconstruct $t\bar{t}$ systems in the 2ℓ , 3ℓ and 4ℓ final states (e.g. 2ℓ case: $t\bar{t} \rightarrow \ell^+ \nu_\ell b \ell^- \bar{\nu}_\ell \bar{b}$). This was initially designed to suppress the $t\bar{t}$ background in the $t\bar{t}Z$ analysis. We can re-purpose this algorithm to distinguish between tWZ and $t\bar{t}Z$ by removing the easily-identifiable Z boson.

The 2ν SM algorithm reconstructs a $t\bar{t}$ system by scanning through the components of two possible neutrino 4-vectors (ν_1 and ν_2). It then aims to determine which ν_1 and ν_2 correspond to the two neutrinos which originate from the decay of a $t\bar{t}$ system the best (quantified by an output weight, $w_{2\nu SM}$). $w_{2\nu SM}$ is the likelihood under the $t\bar{t}$ dilipeton final state hypothesis. We are able to use this algorithm in our analysis to discriminate between tWZ and $t\bar{t}Z$ since we can easily reconstruct the OSSF leptons which decay from the Z boson and remove it before inputting the event into the algorithm. We would then expect that the 2ν SM algorithm returns a higher score from a $t\bar{t}Z$ event (~ 1 , i.e. it looks like a $t\bar{t}$ event after removal of the Z boson) and a lower score from a tWZ event (~ 0 , i.e. it does not look like a $t\bar{t}$ event after removal of the Z boson).

4.8.1 The algorithm

The 2ν SM algorithm starts off by writing down four equations which correspond to the invariant masses of the top quark ($m(t)$) and W boson ($m(W)$) for the two top decays (i.e. $t \rightarrow W^+ b \rightarrow \ell^+ \nu_\ell$) in a dileptonic $t\bar{t}$ event. These can be written as,

$$(\ell_1 + \nu_1)^2 = m(W)^2 = (80.385 \text{ GeV})^2 \quad (4.3)$$

$$(\ell_1 + \nu_1 + b_{1,2})^2 = m(t)^2 = (172.5 \text{ GeV})^2 \quad (4.4)$$

$$(\ell_2 + \nu_2)^2 = m(W)^2 = (80.385 \text{ GeV})^2 \quad (4.5)$$

$$(\ell_2 + \nu_2 + b_{2,1})^2 = m(t)^2 = (172.5 \text{ GeV})^2 \quad (4.6)$$

where the subscripts indicate that these particles originate from the decay of two different top quarks in a $t\bar{t}$ system. We assume that the mass of the neutrinos (ν_1 and ν_2) are close to zero, which leaves us with 6 unknowns, p_{T,ν_1} , ϕ_{ν_1} , η_{ν_1} , p_{T,ν_2} , ϕ_{ν_2} and η_{ν_2} (components of the two neutrino's 4-vectors).

The 2ν SM algorithm takes the 4-vectors of the two reconstructed leptons (not from the Z boson) and the two jets with the highest DL1r b -tagger score as input. For each neutrino (ν_1 and ν_2), we scan over a range of possible η and

¹software tool and weights provided by Thomas McCarthy ($t\bar{t}Z$ analysis group - Max Planck Institute)

1005 ϕ values. These values were chosen to be $\phi_{\nu_1}, \phi_{\nu_2} \in [-\pi, \pi]$ with a step size of ≈ 0.25 and $\eta_{\nu_1}, \eta_{\nu_2} \in [-5, 5]$ with a
1006 step size of ≈ 0.31 . These ranges were chosen to maximize accuracy and minimize computation time. For each of
1007 these possible η and ϕ values, we calculate the corresponding p_T for each neutrino. The transverse momentum of
1008 a neutrino, $p_{T,\nu}$, can be calculated via (*****referecne somewhere here*****),

$$p_{T,\nu} = \frac{\frac{1}{2}(m(W)^2 - m(\ell)^2)}{E_\ell \cosh \eta_\nu - p_{\ell,z} \sinh \eta_\nu - p_{\ell,x} \cos \phi_\nu - p_{\ell,y} \sin \phi_\nu} \quad (4.7)$$

1009 where E_ℓ is the energy of the lepton and $p_{\ell,z}, p_{\ell,x}, p_{\ell,y}$ are the z, x and y components of lepton's momentum. At
1010 this stage, we have possible 4-vectors for ν_1 and ν_2 . Using these possible neutrino 4-vectors, we reconstruct the two
1011 possible $t\bar{t}$ systems,

$$t_1 = \ell_1 + b_1 + \nu_1 \text{ and } t_2 = \ell_2 + b_2 + \nu_2 \quad (4.8)$$

OR

$$t_1 = \ell_1 + b_2 + \nu_1 \text{ and } t_2 = \ell_2 + b_1 + \nu_2 \quad (4.9)$$

1012 These reconstructed $t\bar{t}$ systems are then used to calculate a weight, $w_{2\nu SM}$. The $w_{2\nu SM}$ weight (a value ranging
1013 from 0 to 1) is defined as a product of four probabilities (described below) and can be written as,

$$w_{2\nu SM} = P_{m_{t_1}} \times P_{m_{t_2}} \times P_{\Delta E_x} \times P_{\Delta E_y} \quad (4.10)$$

1014 The $w_{2\nu SM}$ is calculated for each pair of reconstructed neutrinos (or reconstructed $t\bar{t}$ systems), with the maximum
1015 value being chosen as the final value for the event.

1016 4.8.2 Calculating $w_{2\nu SM}$

1017 We use distributions of well modelled observables ($m_{b\ell\nu}$ and ΔE_x) from simulated $t\bar{t}$ events in order to determine
1018 how well our reconstructed neutrinos (and in turn top quarks) resemble neutrinos (and top quarks) present in a $t\bar{t}$
1019 event.

1020 4.8.2.1 $P_{m_{t_1}}$ and $P_{m_{t_2}}$

1021 A normalised distribution of the mass of reconstructed top quarks ($m_{b\ell\nu}$) from a $t\bar{t}$ sample is generated to
1022 determine the probabilities $P_{m_{t_1}}$ and $P_{m_{t_2}}$. The distribution is generated from reco-level leptons, generator-level
1023 neutrinos and reoc-level jets matched in ΔR to generator-level b -quarks, therefore only filling the distribution with
1024 correct detector-level objects. We then use the distribution to interpolate our two reconstructed top quarks, which
1025 returns a weight value from 0 to 1, with higher values corresponding to a reconstructed top quark which has a
1026 mass close to that of a top quark from a $t\bar{t}$ system. This interpolation is done for both reconstructed tops, t_1 and
1027 t_2 , corresponding to probabilities $P_{m_{t_1}}$ and $P_{m_{t_2}}$. The distribution used is shown in Figure 4.41.

1028 In Figure 4.41, the $m_{b\ell\nu}$ distribution (generated from simulated $t\bar{t}$ events), used to calculate $P_{m_{t_1}}$ and $P_{m_{t_2}}$ is
1029 shown.

1031 4.8.2.2 $P_{\Delta E_x}$ and $P_{\Delta E_y}$

1032 A similar method is used to determine $P_{\Delta E_x}$ and $P_{\Delta E_y}$. In this case we generate a weight distribution of $\Delta E_x =$
1033 $(p_{T,\nu_1})_x + (p_{T,\nu_2})_x - (E_T^{\text{miss}})_x$ based off simulated $t\bar{t}$ events. In particular, this distribution is generated using reco-
1034 level E_T^{miss} and generator-level neutrinos. The use of this distribution lies under the assumption that neutrinos are
1035 the dominant source of E_T^{miss} , and therefore, $(E_T^{\text{miss}})_x \approx (p_{T,\nu_1})_x + (p_{T,\nu_2})_x$ and $(E_T^{\text{miss}})_y \approx (p_{T,\nu_1})_y + (p_{T,\nu_2})_y$. We
1036 then use the distribution to interpolate the value of ΔE_x and ΔE_y from our reconstructed neutrinos. This returns
1037 a weight value from 0 to 1, with higher values corresponding to ΔE_x and ΔE_y (and in turn our reconstructed
1038 neutrino's p_T) closer to those observed in a $t\bar{t}$ event. We expect the ΔE_x and ΔE_y distributions to have the
1039 same shapes, therefore we only need to generate one (we have chosen ΔE_x). In Figure 4.42, the $m_{b\ell\nu}$ distribution
1040 (generated from simulated $t\bar{t}$ events), used to calculate $P_{m_{t_1}}$ and $P_{m_{t_2}}$ is shown.

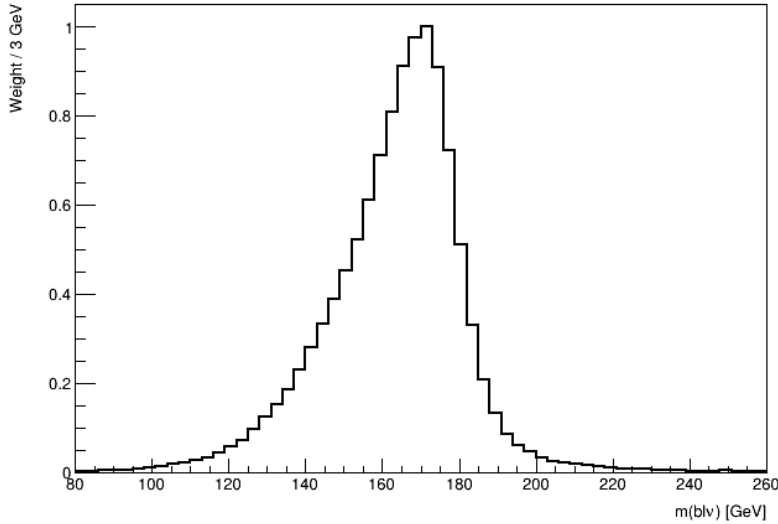


Figure 4.41: $m_{b\ell\nu}$ distribution generated from simulated $t\bar{t}$ events, used to calculate $P_{m_{t_1}}$ and $P_{m_{t_2}}$ is shown. The $m_{b\ell\nu}$ distribution is shown by the black lined histogram. The mass of the $b\ell\nu$ system is shown on the x-axis. The corresponding weight of the $m_{b\ell\nu}$ distribution is shown on the y-axis.

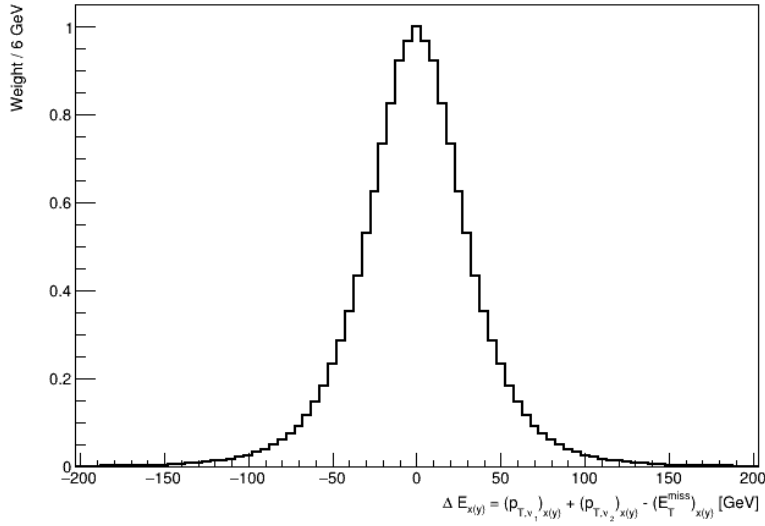


Figure 4.42: ΔE_x distribution generated from simulated $t\bar{t}$ events, used to calculate $P_{\Delta E_x}$ and $P_{\Delta E_y}$ is shown. The ΔE_x distribution is shown by the black lined histogram. ΔE_x is shown on the x-axis. The corresponding weight of ΔE_x distribution is shown on the y-axis.

1041 4.8.3 Kinematic Veto

1042 The 2ν SM algorithm is extremely computationally intensive. The computation time depends on the number step
 1043 size of the ϕ and η ranges which we scan over to reconstruct the neutrinos. For example, consider the step sizes
 1044 chosen in this analysis, $\Delta\eta \approx 0.31$ and $\Delta\phi \approx 0.25$ which corresponds to 32 values for η and 25 values for ϕ . There
 1045 will be $(32)(32)(25) = 640\,000$ possible pairs of neutrinos (ν_1 and ν_2) to consider **per event**. Since we have to
 1046 consider two possible $t\bar{t}$ systems (See Equations 4.8 and 4.9), this number effectively increases to $(2)(640000) = 128$
 1047 000 0 iterations **per event**. In order to reduce the number of $t\bar{t}$ systems we need to consider, therefore decreasing
 1048 computation time, we look at distributions of well modelled observables from $t\bar{t}$ events and veto (discard) a possible
 1049 reconstructed $t\bar{t}$ system if the observable in question is improbable or unlikely to be observed in a $t\bar{t}$ event. To
 1050 achieve this, we define a threshold range for these observables (See Figure 4.45 and Figure 4.47), and if the possible
 1051 reconstructed $t\bar{t}$ system's corresponding value for this observable lies outside this range, it is vetoed and the algorithm
 1052 continues with the next iteration.

1053 **4.8.3.1 $\Delta\langle m(\ell b) \rangle$**

1054 The first observable which we consider is the difference between average mass of the two possible ℓb system combi-
1055 nations, $\Delta\langle m(\ell b) \rangle$. The two possible ℓb system combinations are,

$$(\ell b)_1 = \ell_1 + b_1 \text{ and } (\ell b)_2 = \ell_2 + b_2 \quad (4.11)$$

OR

$$(\ell b)_1 = \ell_1 + b_2 \text{ and } (\ell b)_2 = \ell_2 + b_1 \quad (4.12)$$

$$(4.13)$$

1056 $\Delta\langle m(\ell b) \rangle$ is therefore defined as,

$$\Delta\langle m(\ell b) \rangle = \frac{1}{2} |[(m(\ell_1 b_1) + m(\ell_1 b_1)) - (m(\ell_1 b_2) + m(\ell_2 b_1))]| \quad (4.14)$$

1057 The idea here is that, if $\Delta\langle m(\ell b) \rangle$ is large, it's more likely that we can simply select the ℓb combination with the
1058 smaller (minimum) average mass. To illustrate this, we look at the distribution (constructed from $t\bar{t}$ events) of
1059 $P(\text{Correct combination of } \ell b \text{ systems} | \text{minimum}\langle m(\ell b) \rangle)$ vs $\Delta\langle m(\ell b) \rangle$ for b -tagged jets in the same ($\eta(b_1) \times \eta(b_2) \geq 0$)
1060 and opposite hemispheres ($\eta(b_1) \times \eta(b_2) < 0$).

1061 In Figure 4.43 the $P(\text{Correct combination of } \ell b \text{ systems} | \text{minimum}\langle m(\ell b) \rangle)$ vs $\Delta\langle m(\ell b) \rangle$, for b -tagged jets in the
same and opposite hemispheres, constructed from $t\bar{t}$ events is shown.

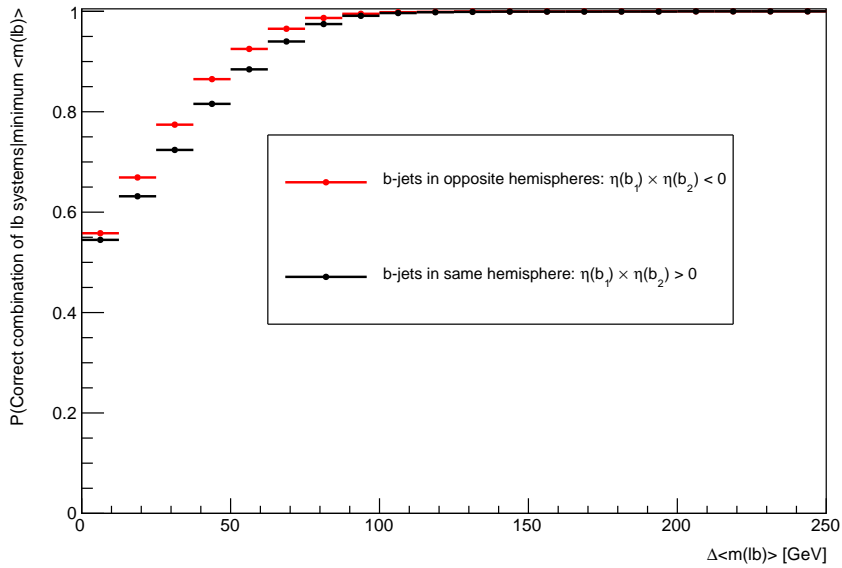


Figure 4.43: $P(\text{Correct combination of } \ell b \text{ systems} | \text{minimum}\langle m(\ell b) \rangle)$ vs $\Delta\langle m(\ell b) \rangle$, for b -tagged jets in the same and opposite hemispheres, constructed from $t\bar{t}$ events is shown. The horizontal red lines represent the distribution in the case when the two b -jets are in opposite hemispheres. The dot in the middle of the line represents the midpoint of the line. The horizontal black lines represent the distribution in the case when the two b -jets are in the same hemispheres. The dot in the middle of the line represents the midpoint of the line. The average $m(\ell b)$ is shown on the x-axis. The $P(\text{Correct combination of } \ell b \text{ systems} | \text{minimum}\langle m(\ell b) \rangle)$ is shown on the y-axis.

1062 From Figure 4.43, for both cases where the b -tagged jets are in the same and opposite hemispheres, the
1063 probability for a correct ℓb system being chosen given that we are considering the ℓb system with mini-
1064 mum average mass is an increasing function which plateaus to 1 at ~ 90 GeV. We use these two distribu-
1065 tions to interpolate the $P(\text{Correct combination of } \ell b \text{ systems} | \text{minimum}\langle m(\ell b) \rangle)$ from $\Delta\langle m(\ell b) \rangle$. We require that
1066 $P(\text{Correct combination of } \ell b \text{ systems} | \text{minimum}\langle m(\ell b) \rangle) > 0.8$, before vetoing any ℓb combination, such that we
1067 have are at least 80% certain that we know the correct ℓb combination. In this case, the ℓb combination with the
1068 maximum $\Delta\langle m(\ell b) \rangle$ is vetoed. If $P(\text{Correct combination of } \ell b \text{ systems} | \text{minimum}\langle m(\ell b) \rangle) < 0.8$ we need to consider
1069 both possible ℓb system combinations.
1070

1071 **4.8.3.2 $\eta(b\bar{b}\ell\ell)$**

1072 We consider η of the $b\bar{b}\ell\ell$ system, $\eta(b\bar{b}\ell\ell)$ to veto improbable $\eta(\nu_1)$ and $\eta(\nu_2)$ values.

1073
1074 In the same way as for $\Delta\langle m(\ell b)\rangle$, we generate a distribution to determine values $\eta(\nu)$ which are improbable for a $t\bar{t}$ event. In this case, we generate a 2D histogram from simulated $t\bar{t}$ events (dileptonic final state) at generator-level of $\eta(\nu)$ vs $\eta(b\bar{b}\ell\ell)$.

1075
1076
1077 In Figure 4.44, a heatmap of occupancy for $\eta(\nu)$ vs $\eta(b\bar{b}\ell\ell)$ (produced from simulated $t\bar{t}$ events) is shown.

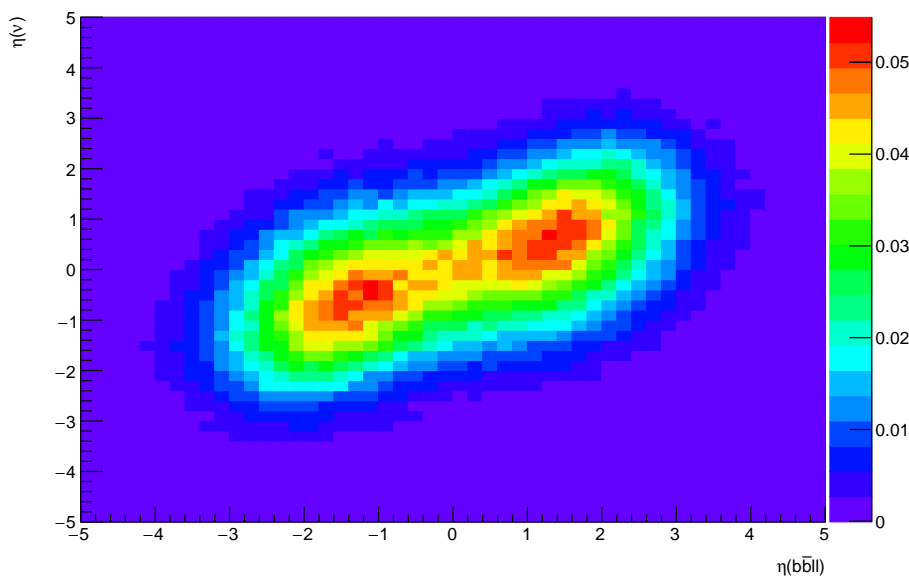


Figure 4.44: Heatmap of occupancy for $\eta(\nu)$ vs $\eta(b\bar{b}\ell\ell)$ produced from simulated $t\bar{t}$ events (dileptonic final state) at generator-level is shown. η of the $b\bar{b}\ell\ell$ system is shown on the x-axis. η of the neutrino is shown on the y-axis. The colorbar on the right represents the occupancy (normalised) in the phase space.

1079 Using the above heatmap, we define a veto region (where a $t\bar{t}$ event is extremely unlikely to occur) based off
1080 double-sided 95% limits (**something here on confidence limit??**). We apply a veto if either possible neutrino
1081 lies within this region. The veto region is shown in Figure 4.45.

1082
1083 In Figure 4.45, the veto region (extracted from Figure 4.44) for vetoing improbable neutrinos is shown.

1084 **4.8.3.3 L_T**

1085 The final kinematic constraint which we consider is the scalar sum of lepton p_T , $L_T = p_T(\ell_1) + p_T(\ell_2)$ which we
1086 use to veto certain possible neutrinos, ν_1 and ν_2 .

1087
1088 Again, we generate a distribution to determine (and veto) improbable possible neutrinos in simulated $t\bar{t}$ events
(dilepton final state).

1089
1090 In Figure 4.46, a heatmap of occupancy for $\Delta R(\ell, \nu)$ vs L_T (produced from simulated $t\bar{t}$ events) is shown.

1091 Using the same method as described in Section 4.8.3.2, we define a veto region where a veto is applied if either
1092 possible neutrino lies within this region. In Figure 4.45, the veto region (extracted from Figure 4.46) for vetoing
1093 improbable neutrinos values is shown.

1094 **4.9 Systematics**

1095 The systematic uncertainties can be separated into experimental (detector) systematics, which are related to the
1096 reconstruction of physics objects in the detector and theoretical uncertainties related to the modelling of the different

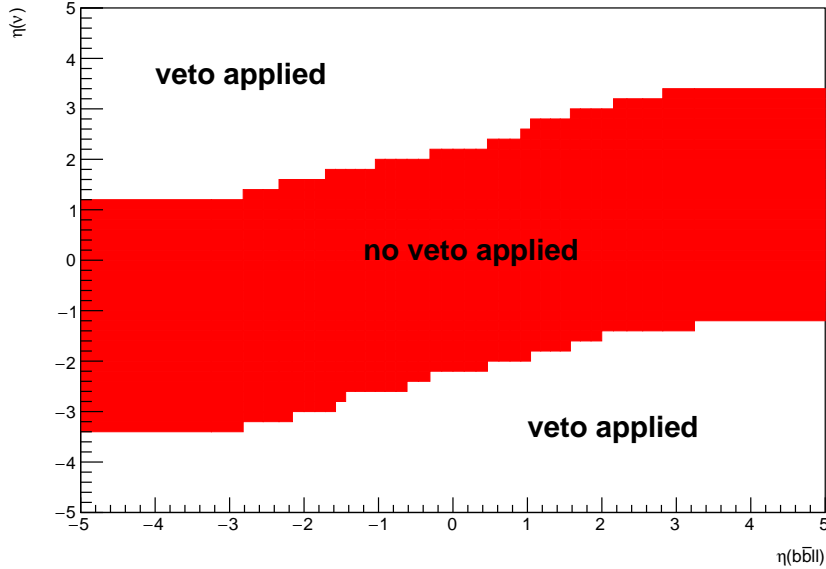


Figure 4.45: The regions where vetoes are applied for the $\eta(b_1 b_2 \ell_1 \ell_2)$ constraint is shown. η of the $b\bar{b}\ell\ell$ system is shown on the x-axis. η of the neutrino is shown on the y-axis. The red band shows the region where the neutrino would not be vetoed. The white areas (above and below the red band) are regions where the neutrino is vetoed.

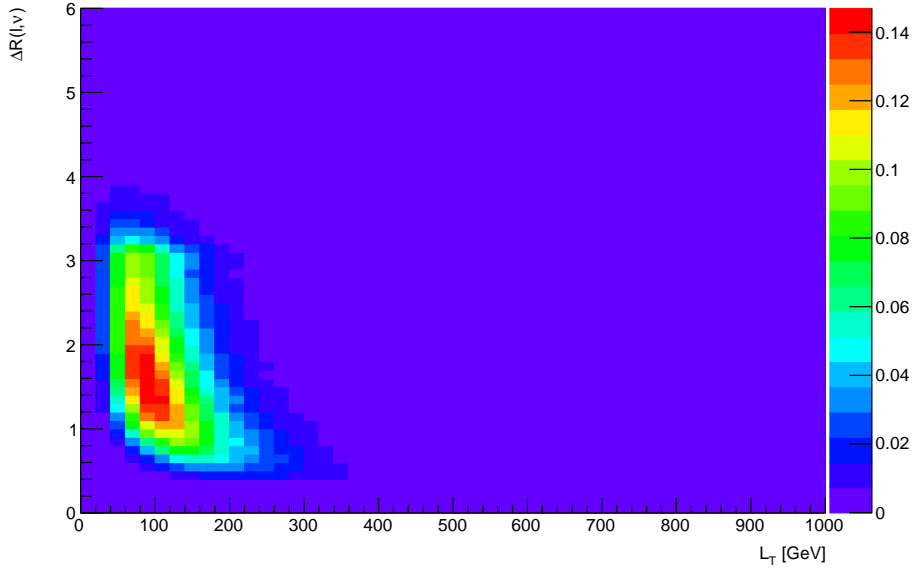


Figure 4.46: A heatmap of occupancy for $\Delta R(\ell, \nu)$ vs L_T produced from simulated $t\bar{t}$ events (dileptonic final state) at generator-level is shown. ΔR between leptons and neutrinos is shown on the x-axis. L_T (scalar sum of lepton p_T) is shown on the y-axis. The colorbar on the right represents the occupancy (normalised) in the phase space.

¹⁰⁹⁷ processes background.

¹⁰⁹⁸ 4.9.1 Experimental uncertainties

¹⁰⁹⁹ In this section, the experimental systematics are outlined.

- ¹¹⁰⁰ • Luminosity:

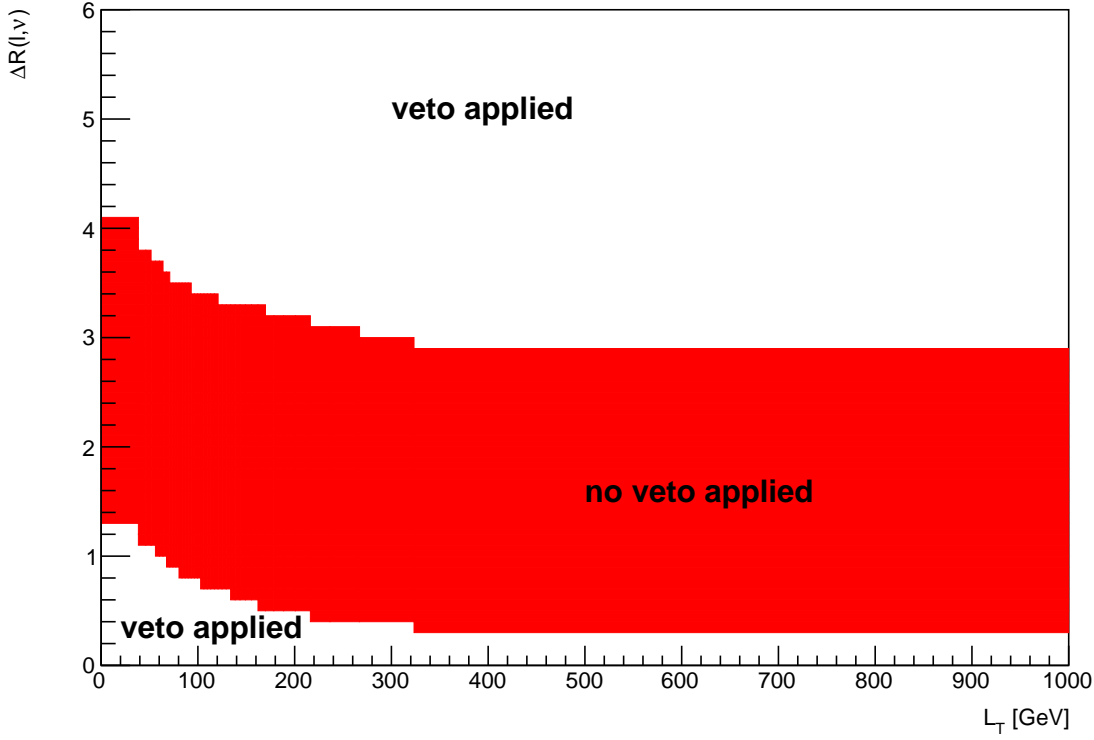


Figure 4.47: The regions where vetoes are applied for the L_T constraint is shown. ΔR between leptons and neutrinos is shown on the x-axis. L_T (scalar sum of lepton p_T) is shown on the y-axis. The red band shows the region where the neutrino would not be vetoed. The white areas (above and below the red band) are regions where the neutrino is vetoed.

1101 The 2015–2018 luminosity estimate of 139fb^{-1} has a relative uncertainty of 3%. This uncertainty is obtained
 1102 using the LUCID-2 detector [22] for the primary luminosity measurements. This systematic uncertainty affects
 1103 all processes modelled using MC simulations.

- 1104 • **Pile-up reweighting:**

1105 An uncertainty related to the SFs used for MC to account for differences in pile-up distributions between
 1106 MC and data is applied. This uncertainty is obtained by re-scaling the $\langle \mu \rangle$ value in data by 1.00 and 1/1.18
 1107 corrections are only applied to MC.

- 1108 • **Jet vertex tagger:**

1109 Uncertainties associated to the JVT are applied via the `JetJvtEfficiency` package [20] which account for
 1110 the residual contamination from pile-up jets after pile-up suppression and the MC generator choice [13].

- 1111 • **Heavy- and light-flavor tagging:**

1112 The efficiency of the flavour-tagging algorithm is measured for each jet flavour using control samples in data
 1113 and in simulation. From these measurements, correction factors are derived to correct the tagging rates in the
 1114 simulation. In the case of b -tagged jets, the correction factors and their uncertainties are estimated from data
 1115 using dileptonic $t\bar{t}$ events [15, 10]. In the case of c -jets, they are derived from jets arising from W boson decays
 1116 in $t\bar{t}$ events [14]. In the case of light-flavour jets, the correction factors are derived using dijet events [11].
 1117 Sources of uncertainty affecting the b - and c -tagging efficiencies are evaluated as a function of jet p_T , including
 1118 bin-to-bin correlations. The uncertainties in the efficiency for tagging light-flavour jets depend on the jet p_T
 1119 and on η . An additional uncertainty is assigned to account for the extrapolation of the b -tagging efficiency
 1120 measurement from the p_T region used to determine the correction factors to regions with higher p_T .

- 1121 • **Electron efficiency:**

Uncertainties associated with the electron efficiency SFs are provided by the egamma CP group [18] and arise from the reconstruction, ID, isolation and trigger efficiencies. They correct for the efficiency difference between data and MC [12] and are measured with a ‘‘tag-and-probe’’ method in $Z \rightarrow e^+e^-$ and $J/\psi \rightarrow e^+e^-$ events. The information on the correlation of the different components of the systematic uncertainties are provided for all efficiency measurements. The default correlation model for the uncertainties is used, which provides one up/down variation for each of the SF components separately [18, 19].

- **Muon efficiency:**

As for electrons, SFs obtained from $Z \rightarrow \mu^+\mu^-$ and $J/\psi \rightarrow \mu^+\mu^-$ events are applied to correct for the differences between data and MC in the muon ID, isolation and trigger efficiencies [16]. Uncertainties on these SFs are provided by the muon CP group [21] and applied as up/down variations of the nominal SFs for each component.

4.9.2 Theoretical uncertainties

In this section, the theoretical systematics are outlined.

- **$t\bar{t}Z$ background:**

An overall normalization uncertainty of 10% is considered for the $t\bar{t}Z$ background. Two generic shape systematics are considered for the $t\bar{t}Z$ background. They are constructed (see Section 4.9.3) by either applying a linear or triangular interpolation to up and down variations which are defined to be $\pm 20\%$ from the nominal $t\bar{t}Z$ background.

- **ZZ background:**

An overall normalization uncertainty of 30% is considered for the ZZ background.

- **$t\bar{t}H$ background:**

An overall normalization uncertainty of 20% is considered for the $t\bar{t}H$ background.

- **tZq background:**

An overall normalization uncertainty of 14% is considered for the tZq background.

- **$t\bar{t}Z$ fake background:**

An overall normalization uncertainty of 50% is considered for the $t\bar{t}Z$ fake background.

- **other background processes:**

The ‘other’ background consists of many processes which have minimal but non-negligible contribution in the signal regions (See Table 4.4). An overall normalization uncertainty of 30% is considered for the ‘other’ background processes.

- **tWZ :** A modelling uncertainty on tWZ is considered by comparing the nominal sample (using the DR1 scheme) and a minimal DR2 sample.

Two generic shape systematics are considered for the tWZ background. They are constructed (see Section 4.9.3) by either applying a linear or triangular interpolation to up and down variations which are defined to be $\pm 20\%$ from the nominal tWZ background.

4.9.3 Generic shape systematics

It is evident that the tetralepton channel is statistically limited. We therefore expect that the uncertainty on u_{tWZ} is dominated by statistical uncertainty and that the impact of shape systematics will be negligible in comparison.

In order to include shape uncertainties related to the modelling of our samples, we construct generic shape systematics for any given sample process. Given that we choose a sufficiently large set of values for which the systematics can take in the fit, the constructed systematics could represent many shape systematics which we have not yet considered to include in the fitting procedure.

We start by constructing an envelope (error bars) consisting of two MC templates. One with the nominal MC template increased by 20% on its normalisation and the other with the nominal MC template decreased by 20% on its normalisation. The templates are then modified from their original shape either by doing linear interpolation (from the leftmost-up variation to the rightmost-down variation) or triangular interpolation (shape is set to zero at the rightmost and leftmost parts and reaches the envelope in the middle). The linear and triangular interpolation is done using TRF's `ForceShape` option [57], which alters the original templates (as described above). This envelope now represents the bounds which the systematic can vary in the fit.

In Figure 4.48 the envelope before and after the shape change, for both the linear and triangular interpolations, for the $t\bar{t}Z$ background in the $t\bar{t}Z$ CR is shown.

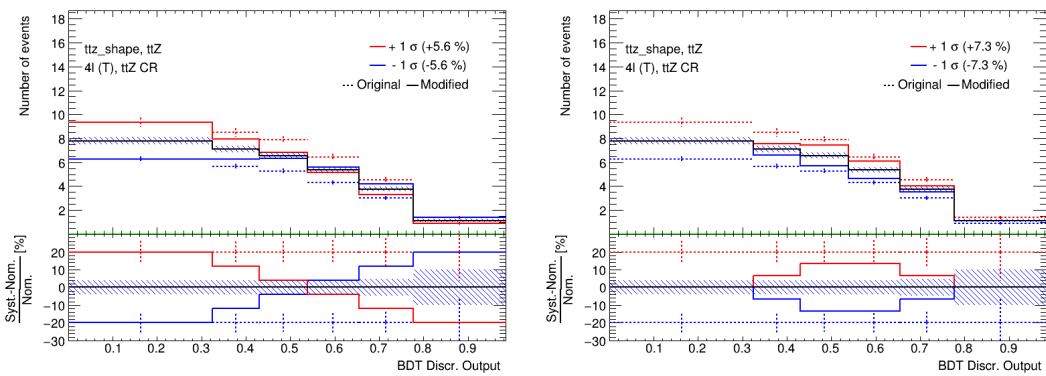


Figure 4.48: $t\bar{t}Z$ generic shape systematic before (original) and after (modified) linear (left) and triangular (right) interpolation in the $t\bar{t}Z$ CR is shown. The output from the event-level BDT shown on the x-axis. In the upper panel, the number of events is shown on the y-axis. In the lower panel, the difference between the systematic variation (the envelope's templates) and the nominal template, divided by the nominal template, is shown on the y-axis. The nominal $t\bar{t}Z$ template is shown by the solid black lined histogram, with the diagonal lined bands representing its total uncertainty. The templates of the upper and lower envelopes (before modification) is given by the dotted red and blue lined histograms respectively. The templates of the upper and lower envelopes (after modification) is given by the solid red and blue lined histograms respectively, with the vertical dotted lines representing its total uncertainty.

We consider two shape systematics (linear and triangular shapes) for tWZ and the most dominant background processes across both channels. In particular, we consider these shape systematics for $t\bar{t}Z$ for both the tri- and tetralepton channels. Additionally, we consider these shape systematics for the $WZ + b$ and $WZ + c$ backgrounds in the trilepton channel.

4.10 Analysis Pipeline and TRexFitter

We make use of industry standard `ROOT`² wrappers in this analysis, namely, `PyROOT` and `TRexFitter`.

`Python` is used extensively in many fields of science (not limited to physics and data science) due to its simplicity and ongoing support by the communities which utilize it. `PyROOT` allows users to access the full `ROOT` functionality within `Python`. More specifically, `PyROOT` provides `Python` bindings for `ROOT`.

`TRexFitter` is a framework for binned template profile likelihood fits[64]. In this analysis, we used `TRexFitter` (tag: `TRexFitter-00-04-13`) to produce all pre-fit and post-fit plots (including fit statistics, e.g. limit, significance, $\mu_{best-fit}$).

The analysis pipeline starts with sample derivations (derived dataset) being submitted to the grid for ntuple production. This applies cuts and selections to the already reduced derivations and produces ntuples with trees containing variables (e.g. scale factors, observables, MC truth flags) that will be used at future stages in the analysis. These ntuples are then read by `PyROOT` where the events are looped over, before being written to `ROOT` files as input

²CERN's HEP data analysis framework (written in C++)

to **TRExFitter**. The Python scripts are used to define the different regions and apply the final cuts and selections outlined in Table 4.3. In addition to this purpose, they are used to train the two BDTs and to produce the output from these trained BDTs. As each event is looped over, the cuts and selection criteria are checked for the given event and is either thrown away (if the event does not pass the selection criteria), or gets written to a ROOT file (if the event passes the selection criteria) corresponding to the MC sample and Run 2 data-set (mc16a, mc16d, mc16e) which it belongs to. These ROOT files contain all observables, weights and scale factors (corresponding to an event) which we wish to use in **TRExFitter**. **TRExFitter** then takes these files as input, runs a maximum likelihood fit and produces relevant plots (e.g. pre-fit, post-fit, pull plots) and statistical parameters (e.g. limit, significance, $\mu_{best-fit}$).

4.10.1 Fitting Procedure

Using the **TRExFitter** framework, binned profile-likelihood fits are performed to determine the signal strength, $\mu_{tWZ} = \frac{\sigma_{obs}(tWZ)}{\sigma_{SM}(tWZ)}$, of tWZ production. A fit across all regions in the tetralepton channel is performed to determine the sensitivity tWZ in this channel. In Section 4.11.2, a combined fit is performed across all regions in the trilepton and tetralepton channels to take advantage of the sensitivity of tWZ in both channels in order to further boost the sensitivity of tWZ .

To characterise the sensitivity and associated uncertainty of our measurement of $\mu(tWZ)$, we compute two metrics: the expected significance (Z_μ^{exp}) and the expected upper limit (μ_{up}^{exp}). In this context, the expected significance can be interpreted as, the probability that the measured signal is due to a background fluctuation. Larger values indicate lower probabilities and smaller values indicate higher probabilities. Particle physicists have adopted a standard to define the sensitivity necessary for evidence and discovery of a particular particle or phenomena. A 3σ (corresponding to a background fluctuation probability of $\approx 10^{-3}$) significance is considered to be evidence for observation and a 5σ (corresponding to a background fluctuation probability of $\approx 10^{-7}$) is considered to be a discovery. The expected upper limit is a single-sided interval test statistic, associated with the POI in the maximum-likelihood fit ($\mu(tWZ)$, in our case). In this context, the expected upper limit can be understood in the following way: consider running an ensemble of MC toy experiments, each with their own confidence interval (a range of possible values for $\mu(tWZ)$). An expected upper limit, at some fixed percentage $x\%$ (or *confidence level*), can be determined from this ensemble. The expected upper limit tells us that, $x\%$ of the toy MC experiment's confidence intervals will contain the true value of $\mu(tWZ)$. A commonly used percentage in particle physics is 95%, which we adopt for this analysis. In particle physics, this is referred to as the *CLs Method* [33]. The CLs test statistic can be calculated 'brute force' by running these MC toy experiments, however this is very CPU intensive. Asymptotic formulae are able to describe the underlining CLs test statistic distributions under certain approximations [8]. Instead of running toy MC experiments, we use asymptotic formulae to perform the CLs method, which reduces computation time from several millions of CPU hours to several CPU minutes. The significance and upper limits which are calculated in this analysis are given a prefix of 'expected' to indicate that these are results from a blinded analysis.

In the separate and combined fits, the *mixed data and MC* fit setup [65] is used. This is done to obtain the most accurate prediction of the expected results while keeping the signal regions blinded. For this setup, first a background-only fit to the control regions using real data is done to determine estimates of the nuisance parameters. Then these estimates are used to construct a modified ASIMOV dataset in the signal regions. Finally, the fit is performed using real data in the control regions and the aforementioned modified ASIMOV data-set in the signal regions.

In these fits, the parameter of interest (POI) is μ_{tWZ} . The POI is ultimately the quantity which we wish to measure and is set as a free parameter (unconstrained; can take any value in the fit). The nuisance parameters are assigned to the systematic uncertainties outlined in Section 4.9. Furthermore, a gamma (γ) nuisance parameter for a bin is added to the likelihood function if the statistical uncertainty in the bin exceeds 0.1% of its nominal value.

Pruning is done per sample and per region on the shape and normalisation uncertainties for samples. A sample's shape and normalisation nuisance parameter is pruned (removed from the limit/fit) if the fraction of signal yield to the total yield (signal + background) is less than 0.01.

An auto-binning algorithm, **TransfoD** [26], was used to define the binning. This aims to maximise $\frac{signal}{background}$ in

1249 each bin. Furthermore, it aims to avoid defining bins with a low number of events.

1250 4.11 Results

1251 In the section, an expected upper limit and an expected significance are set on the cross section of tWZ . This is
 1252 performed for the current analysis in the tetralepton channel as well as for a combined analysis across the trilepton
 1253 and tetralepton channels. The trilepton analysis was performed as an independent study by Benjamin Warren
 1254 (UCT) [66]. Note that throughout this section, all signal regions remain blinded.

1255 4.11.1 Tetralepton Channel

1256 In Figure 4.49 pre-fit distributions for the variables used in the likelihood fit in each region are shown.

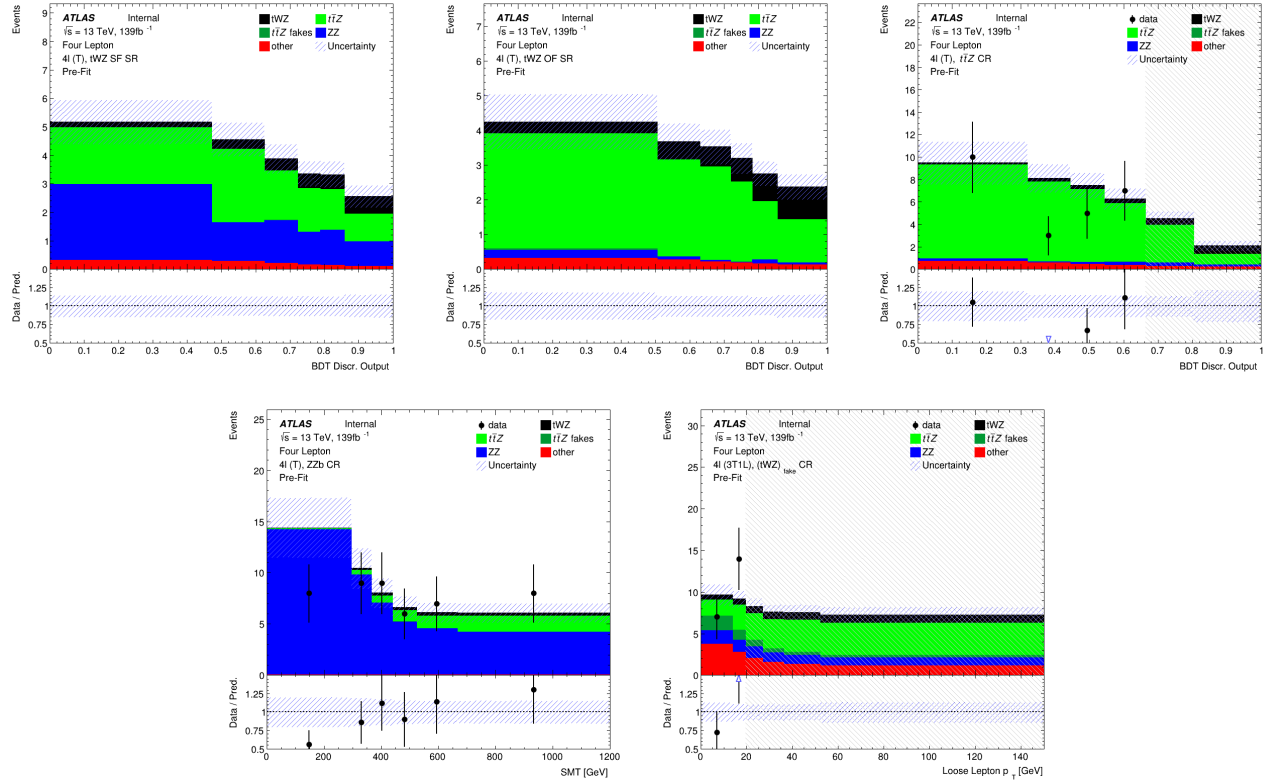


Figure 4.49: Pre-fit distributions (blinded) of variables used in the fit are shown. The data is given by the black points and the MC predictions for each process are given by the histograms. The vertical lines on the data points represent the total uncertainty in the data and the diagonal lined bands represent the total MC uncertainty. The lower panel in each plot shows the ratios of the data to the theoretical predictions. The plots in the tWZ OF SR and tWZ SF SR are kept blinded by omitting the data points. **Top left:** The event-level BDT Disc. Output in the tWZ SF (4T) SR region is shown. **Middle Top:** The event-level BDT Disc. Output in the tWZ SF (4T) SR region is shown. **Top right:** The event-level BDT Disc. Output in the $t\bar{Z}$ CR region is shown. **Bottom left:** $SMT = \sum p_T(\ell) + \sum p_T(jet) + E_T^{\text{miss}}$ in the ZZb CR is shown. **Bottom right:** p_T (loose lepton) in the $(tWZ)_{\text{fake}}$ (3T1L) CR is shown.

1257 In Figure 4.50 pre-fit distributions for the variables used in the likelihood fit in each region are shown.

1258 In Table 4.10, the post-fit yields for each sample in each region is shown.

1259 The expected upper limit of tWZ in the tetralepton channel is measured as,

$$\mu_{up}^{\exp} = 1.61^{+2.35}_{-1.16} \quad (4.15)$$

1260 The expected significance of tWZ in the tetralepton channel is measured as,

$$Z_{\mu}^{\exp} = 1.44\sigma \quad (4.16)$$

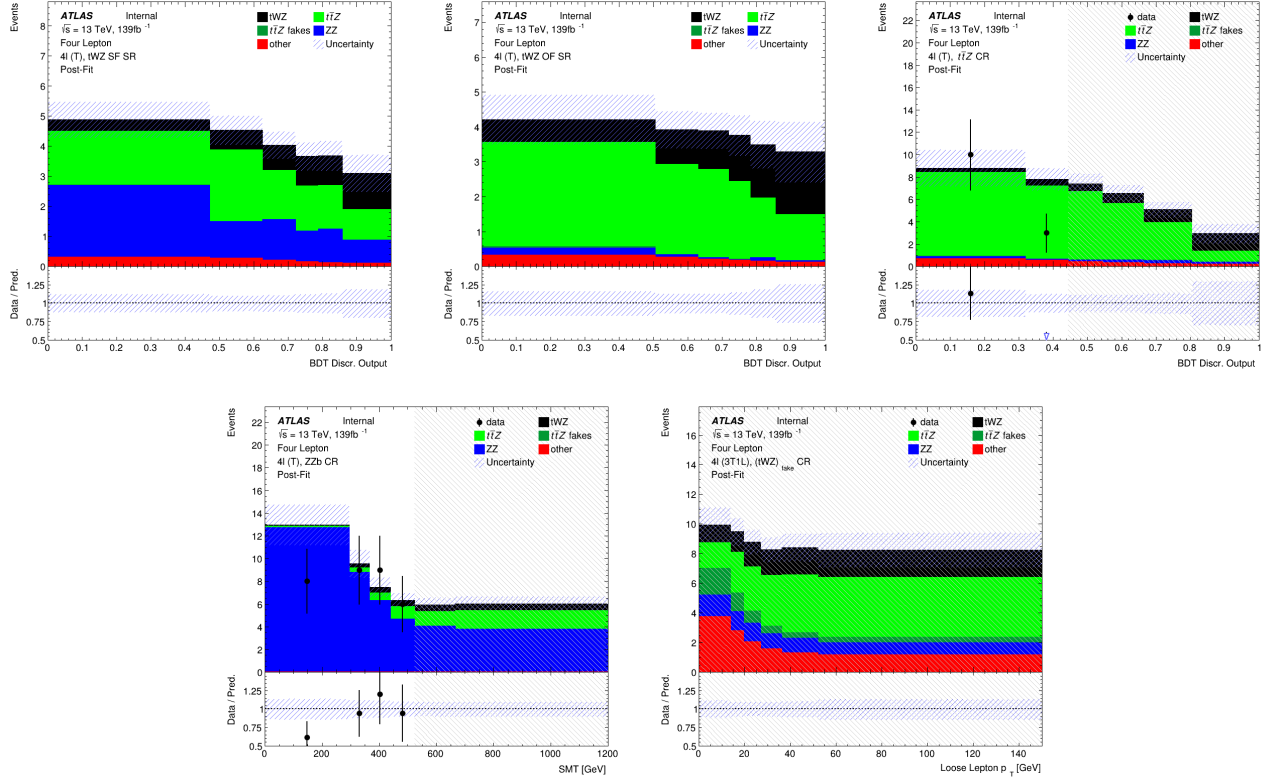


Figure 4.50: Post-fit distributions (blinded) of variables used in the fit are shown. The data is given by the black points and the MC predictions for each process are given by the histograms. The vertical lines on the data points represent the total uncertainty in the data and the diagonal lined bands represent the total MC uncertainty. The lower panel in each plot shows the ratios of the data to the theoretical predictions. The plots in the tWZ OF SR and tWZ SF SR are kept blinded by omitting the data points. **Top left:** The event-level BDT Disc. Output in the tWZ SF (4T) SR region is shown. **Middle Top:** The event-level BDT Disc. Output in the tWZ SF (4T) SR region is shown. **Top right:** The event-level BDT Disc. Output in the $t\bar{t}Z$ CR region is shown. **Bottom left:** $SMT = \sum p_T(\ell) + \sum p_T(jet) + E_T^{\text{miss}}$ in the ZZb CR is shown. **Bottom right:** p_T (loose lepton) in the $(tWZ)_{\text{fake}}$ (3T1L) CR is shown.

	tWZ OF SR	tWZ SF SR	$t\bar{t}Z$ CR	ZZb CR	$(tWZ)_{fake}$ CR	
$t\bar{t}Z$	13.2379 ± 1.52295	9.62061 ± 1.12291	29.9054 ± 3.60908	5.08899 ± 0.620121	18.5393 ± 2.23036	
$t\bar{t}Z$ fakes	0.0702522 ± 0.0468691	0.0334067 ± 0.0256903	0.0723509 ± 0.0418526	0.0485273 ± 0.029133	5.04378 ± 2.34732	
tWZ	7.83414 ± 3.31679	5.33547 ± 2.24801	5.69373 ± 2.58041	2.89889 ± 1.23837	10.278 ± 4.3345	
ZZ	0.481776 ± 0.119774	7.72372 ± 1.2351	1.07955 ± 0.182461	40.6067 ± 6.26078	6.86097 ± 1.11443	
other	tt tZq $t\bar{t}W$ WZ $t\bar{t}t$ $t\bar{t}\bar{t}$ $t\bar{t}WW$ $VVV(V = W/Z)$ $t\bar{t}H$	$6.00553e-06 \pm 3.02819e-06$ 0.0827905 ± 0.0398773 $0.00668643 \pm 0.00792217$ 0.0442934 ± 0.024156 $0.000987164 \pm 0.000766266$ 0.00934035 ± 0.0080554 0.0294618 ± 0.0263174 0.280643 ± 0.0853411 0.846054 ± 0.175495	0.252557 ± 0.442116 0.0756107 ± 0.0354584 $0.00279748 \pm 0.00287361$ 0.0396511 ± 0.0154282 $0.00247481 \pm 0.00136945$ 0.0107458 ± 0.00849984 0.029771 ± 0.0195582 0.191433 ± 0.0586778 0.669375 ± 0.140107	0.273507 ± 0.223201 0.063585 ± 0.0293325 $6.00553e-06 \pm 3.02819e-06$ 0.0133471 ± 0.0128199 0.0140869 ± 0.00479496 0.0571373 ± 0.0204011 0.264364 ± 0.0926252 0.0697266 ± 0.0225059 1.96662 ± 0.401199	$6.00553e-06 \pm 3.02819e-06$ 0.055884 ± 0.0244084 0.002306 ± 0.00564349 0.0472562 ± 0.0330315 $6.00553e-06 \pm 3.02819e-06$ $6.00553e-06 \pm 3.02819e-06$ 0.0129431 ± 0.0323803 0.171142 ± 0.0518102 0.150025 ± 0.0353826	2.35427 ± 0.917112 4.90963 ± 0.745354 0.943182 ± 0.292148 1.83567 ± 0.392459 0.0100558 ± 0.00363157 0.0216809 ± 0.00992819 0.152448 ± 0.058965 0.266502 ± 0.0810194 2.21264 ± 0.451623
Total	22.9243 ± 2.96284	23.9876 ± 2.11249	39.4734 ± 3.44937	49.0856 ± 6.04162	53.4282 ± 4.31683	
data	-	-	36	49	57	

Table 4.10: The post-fit yields for each sample in each region is shown.

1261 The best-fit value of the signal strength, $\mu(tWZ) = \frac{\sigma(tWZ)}{\sigma(tWZ)_{SM}}$, from the likelihood fit is measured as,

$$\mu(tWZ) = 1.91^{+0.95}_{-0.82} \quad (4.17)$$

1262 The expected upper limit is in agreement with the extracted best-fit value on the signal strength, therefore no
1263 deviations from the SM cross section of tWZ is observed. Neither the 3σ evidence nor the 5σ discovery standards
1264 are reached for the expected significance. This is not surprising, given the low amount of events present in the
1265 tetralepton channel.

1266 In Figure 4.51, a ranking plot showing the impact of the systematic uncertainties on the POI, $\mu(tWZ)$ is shown.
1267 The most important systematics are the cross sections of $t\bar{t}Z$ and ZZ , and shape modelling on $t\bar{t}Z$ ($t\bar{t}Z$ triangular
1268 shape) and tWZ (tWZ -DR2 and tWZ triangular shape). The cross section of ZZ is significantly shifted down
1269 in the fit from its nominal value. The $t\bar{t}Z$ cross section, tWZ -DR2 and $t\bar{t}Z$ triangular shape nuisance parameters
1270 are similarly shifted down in the fit from their nominal values, but to a much lesser degree than the cross section
1271 of ZZ . These pulls are all within 1σ uncertainty and are thus relatively small. It is expected that the modelling
1272 uncertainties (shape and normalisations) of the most dominant backgrounds (e.g. $t\bar{t}Z$, ZZ) have relatively large
1273 impacts on $\mu(tWZ)$, since the uncertainty of the analysis is dominated by statistical uncertainty.

1275 4.11.2 Trilepton and Tetralepton Channels

1276 In the section, an expected upper limit and an expected significance are set on the cross section of tWZ from the
1277 combined fit across all regions of tWZ in the tetralepton and trilepton channels.

1278 The trilepton analysis follows a similar analysis strategy to that of the tetralepton analysis. It includes an
1279 event-level BDT which aims to discriminate between the tWZ and all background as well as an object-level
1280 BDT which aims to identify hadronically decaying W bosons to discriminate between tWZ and the large WZ
1281 background. One tWZ SR is defined and five CRs are defined. WZ and $t\bar{t}Z$ CRs are defined to constrain the
1282 dominant WZ and $t\bar{t}Z$ backgrounds. Three CRs which require that one of the three selected leptons are loose, are
1283 defined for WZ , $t\bar{t}Z$ and tWZ in order to constraint the fake lepton component (using the MC template method -
1284 similar to the method used in Section 4.6 to estimate the fake lepton component).

1285 The expected upper limit of tWZ in the trilepton channel is measured as,

$$\mu_{up}^{exp} = 2.65^{+3.67}_{-1.91} \quad (4.18)$$

1286 The expected significance of tWZ in the trilepton channel is measured as,

$$Z_\mu^{exp} = 0.75\sigma \quad (4.19)$$

1287 The best-fit value of the signal strength, $\mu(tWZ) = \frac{\sigma(tWZ)}{\sigma(tWZ)_{SM}}$, from the likelihood fit is measured as,

$$\mu(tWZ) = 1.16^{+1.33}_{-1.30} \quad (4.20)$$

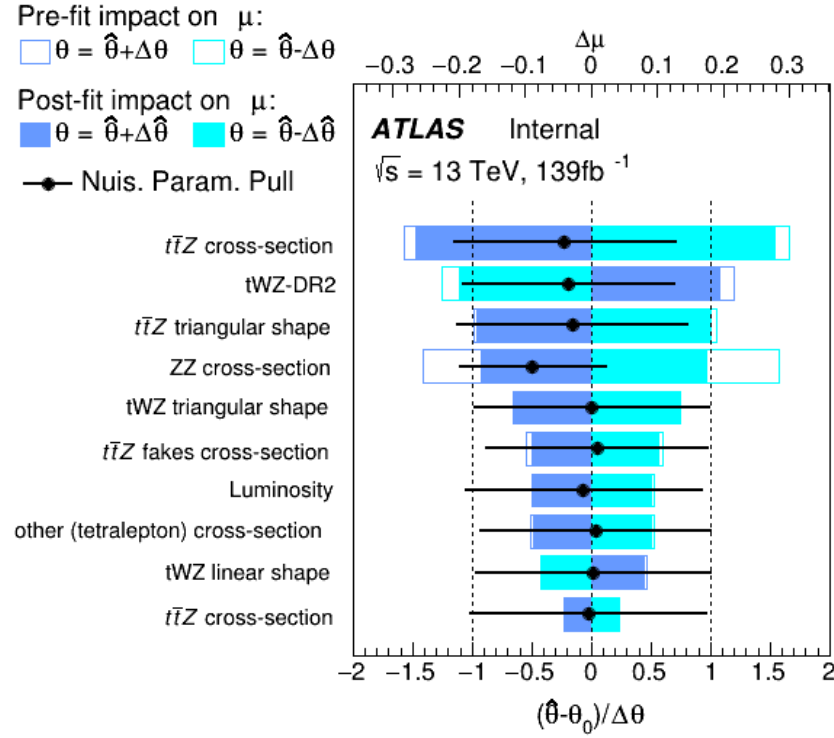


Figure 4.51: A ranking plot showing the impact (ordered from top to bottom via decreasing impact) of the systematic uncertainties (top 10) on the POI, $\mu(tWZ)$, in the tetralepton channel is shown. $\hat{\theta}$ is the best-fit value of the nuisance parameter. $\Delta\hat{\theta}$ and $\Delta\theta$ are the post-fit and pre-fit uncertainties respectively. The post-fit and pre-fit impact of each nuisance parameter on $\mu(tWZ)$ are shown with the solid and lined rectangles respectively. The empty and solid blue rectangles correspond to the pre-fit and post-fit impacts on $\mu(tWZ)$ respectively. These impacts are shown on the upper axis ($\Delta\mu$). On the lower axis, the nuisance parameter pull, $\frac{\hat{\theta} - \theta_0}{\Delta\theta}$, is shown (θ_0 is the nominal pre-fit value of the nuisance parameter). The nuisance parameter pull is indicated by the black points, with their relative post-fit errors ($\frac{\Delta\hat{\theta}}{\Delta\theta}$) shown by the black horizontal error bars.

1290 The expected upper limit is in agreement with the extracted best-fit value on the signal strength, therefore no
 1291 deviations from the SM cross section of tWZ is observed.

1292 In Table 4.11, the nuisance parameters used in the fit, including which channel's regions are affected by each, are
 1293 shown.
 1294

1295 The expected upper limit of tWZ across both channels is measured as,

$$\mu_{up}^{exp} = 1.43^{+2.04}_{-1.03} \quad (4.21)$$

1296 The expected significance of tWZ across both channels is measured as,

$$Z_\mu^{exp} = 1.61\sigma \quad (4.22)$$

1297 The best-fit value of the signal strength, $\mu(tWZ) = \frac{\sigma(tWZ)}{\sigma(tWZ)_{SM}}$, from the likelihood fit is measured as,

$$\mu(tWZ) = 1.80^{+0.70}_{-0.65} \quad (4.23)$$

1298 In Figure 4.52, the expected upper limits of the trilepton channel, tetralepton channel and both channels combined
 1299 are shown.

1300 It can be seen that the sensitivity of tWZ is mostly driven by the tetralepton analysis, with the trilepton analysis
 1301 attributing a small decrease in the expected upper limit of the combined analysis, and its associated uncertainty.

1302 In Figure 4.53, the best-fit values of $\mu(tWZ)$ from the fit for the trilepton channel, tetralepton channel and both
 1303 channels combined are shown.

Nuisance Parameter	Channel Affected	
	trilepton	tetralepton
$\sigma(t\bar{t}H)$	✓	✓
$\sigma(t\bar{t}Z)$	✓	✓
$\sigma(WZ)$	✓	✓
$\sigma(tZq)$	✓	✓
$\sigma(ZZ)$	✓	✓
$\sigma(\text{other(trilepton)})$	✓	✗
$\sigma(\text{other(tetralepton)})$	✗	✓
$\sigma(t\bar{t}Z)_{\text{fakes}}$	✗	✓
$\sigma(t\bar{t})_{\text{fakes}}$	✓	✗
$\sigma(Z + \text{jets})_{\text{fakes}}$	✓	✗
Luminosity	✓	✓
jvt	✓	✓
pileup	✓	✓
DL1r SF (b jets)	✓	✓
DL1r SF (light jets)	✓	✓
$\sigma(tWZ - DR2)$	✗	✓
lepton SF	✓	✓
$t\bar{t}Z$ triangular shape	✓	✓
$t\bar{t}Z$ linear shape	✓	✓
$WZ + b$ triangular shape	✓	✗
$WZ + b$ linear shape	✓	✗
$WZ + c$ triangular shape	✓	✗
$WZ + c$ linear shape	✓	✗

Table 4.11: A summary of the nuisance parameters used in the combined fit is shown. The channels which are affected by each nuisance parameter are indicated with a ✓ (is affected) or a ✗ (is not affected).

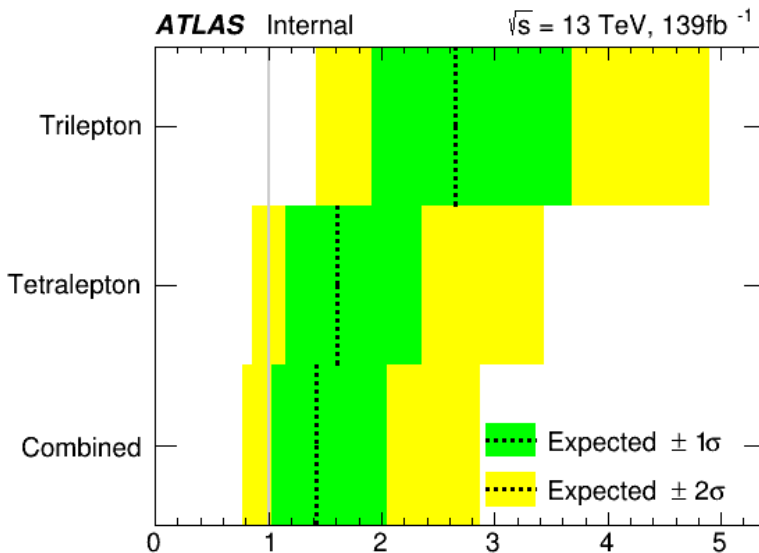


Figure 4.52: The expected upper limits of the trilepton channel, tetralepton channel and both channels combine are shown. The y-axis shows the channels in which the fitting procedure was performed. The expected limits are represented by the vertical dotted line. One- and two- σ uncertainty bands are shown in green and yellow respectively. The vertical grey line indicates when $\mu(tWZ) = 1$.

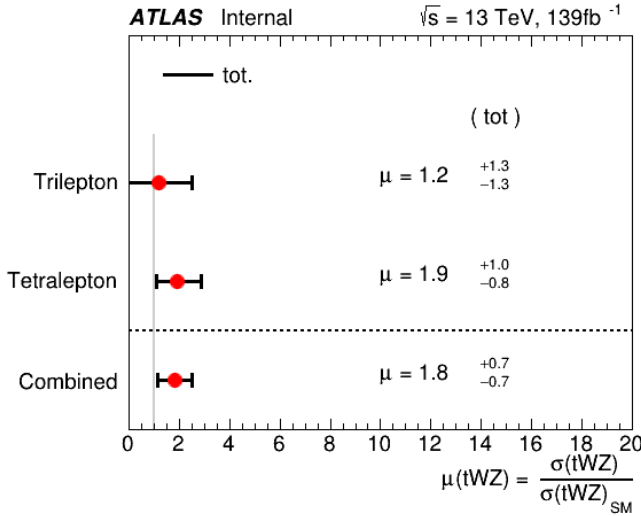


Figure 4.53: The best-fit values of $\mu(tWZ)$ from the fit for the trilepton channel, tetralepton channel and both channels combined are shown. The y-axis shows the channels in which the fitting procedure was performed. The signal strength $\mu(tWZ)$ is shown on the x-axis. The nominal signal strengths are represented by the red dots. The total uncertainty associated with the best-fit $\mu(tWZ)$ value is shown by the black error bars.

1305 It can be seen from Figures 4.52 and 4.53 that the best fit value for the signal strength on tWZ , $\mu(tWZ)$, and the
 1306 expected limits for the tri- and tetralepton channels are consistent with one-another (their uncertainties overlap).
 1307 Therefore it is appropriate to combine these two analyses.

1308 In Figure 4.54, a ranking plot showing the impact of the systematic uncertainties on the POI, $\mu(tWZ)$, in the
 1309 combined fit across both the tri- and tetralepton channels is shown.

1311 Some nuisance parameters are pulled down from their nominal pre-fit values, however these are all within 1σ
 1312 uncertainty and are thus relatively small. It is expected that the modelling uncertainties (shape and normalisa-
 1313 tions) of the most dominant backgrounds (e.g. $t\bar{t}Z$, ZZ , WZ) have relatively large impacts on $\mu(tWZ)$, since the
 1314 uncertainty of the analysis is dominated by statistical uncertainty.

1315 The most important systematics are the cross sections of $t\bar{t}Z$, ZZ and $WZ + b$, and shape modelling on $t\bar{t}Z$
 1316 ($t\bar{t}Z$ triangular shape). The aforementioned nuisance parameters are significantly shifted down in the fit from its
 1317 nominal value. The less important systematics are pulled in the fit from their nominal values, but to a much lesser
 1318 degree than the cross section of those mentioned above. It is expected that the modelling uncertainties (shape and
 1319 normalisations) of the most dominant backgrounds (e.g. $t\bar{t}Z$, ZZ and $WZ + b$) have relatively large impacts on
 1320 $\mu(tWZ)$, since the uncertainty of the analysis is dominated by statistical uncertainty.

1322 4.11.2.1 Projection to Higher Luminosity

1323 In this section we apply a fully blinded fit to the ASIMOV dataset for integrated luminosities larger than the 139 fb^{-1}
 1324 currently available from the ATLAS Full Run 2 dataset. This study gives us insight into the sensitivity of tWZ
 1325 which we could expect if we were to replicate the current analysis, given more data. Given the upgrades planned
 1326 for the LHC and the ATLAS detector, we will soon expect a large increase in available pp collision data (reaching
 1327 $\mathcal{L} = 3000 \text{ fb}^{-1}$ [28]). This study therefore gives us an idea of the sensitivity of tWZ which we can expect in the future.

1328 In Figure 4.55, the expected upper limit and significance for combined fully blinded fits to the ASIMOV dataset
 1329 across both the tri- and tetralepton channels for a range integrated luminosities are shown.
 1330 As we increase the total integrated luminosity, the sensitivity of tWZ increases. The increase in sensitivity is shown
 1331 by the decrease of the expected upper limit and the increase of the expected significance with increasing integrated
 1332 luminosity. It can be noted that a 3σ expected significance is achieved at $\mathcal{L} \sim 400 \text{ fb}^{-1}$, indicating evidence for
 1333 observation of tWZ . The 5σ significance 'discovery' standard is above our 1000 fb^{-1} luminosity range of study.
 1334 Furthermore, these plots show that the sensitivity of tWZ is hindered by the low amount of events we observe,

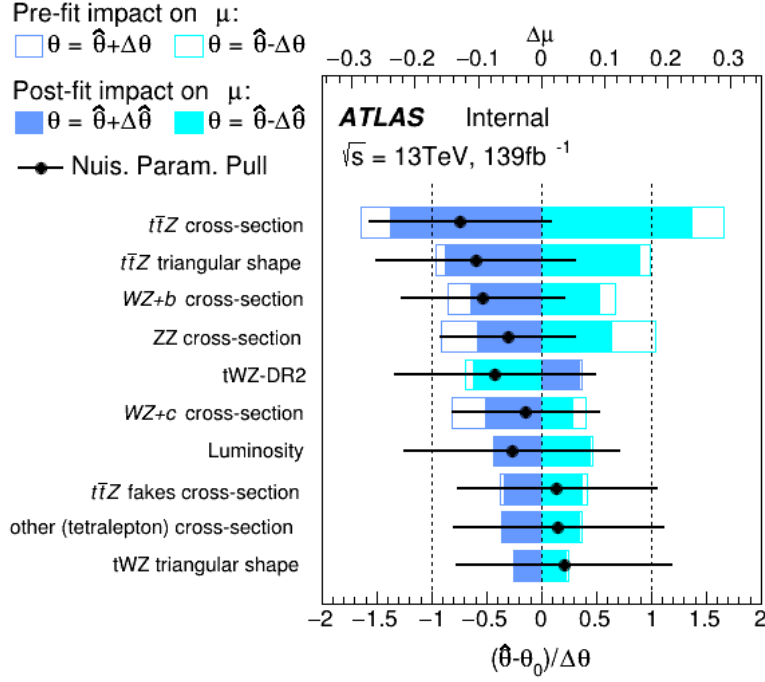


Figure 4.54: A ranking plot showing the impact of the systematic uncertainties (top 10) on the POI, $\mu(tWZ)$, in the combined fit across both the tri- and tetralepton channels is shown. $\hat{\theta}$ is the best-fit value of the nuisance parameter. $\Delta\hat{\theta}$ and $\Delta\theta$ are the post-fit and pre-fit uncertainties respectively. The post-fit and pre-fit impact of each nuisance parameter on $\mu(tWZ)$ are shown with the solid and lined rectangles respectively. The empty and solid blue rectangles correspond to the pre-fit and post-fit impacts on $\mu(tWZ)$ respectively. These impacts are shown on the upper axis ($\Delta\mu$). On the lower axis, the nuisance parameter pull, $\frac{\hat{\theta} - \theta_0}{\Delta\theta}$, is shown (θ_0 is the nominal pre-fit value of the nuisance parameter). The nuisance parameter pull is indicated by the black points, with their relative post-fit errors ($\frac{\Delta\hat{\theta}}{\Delta\theta}$) shown by the black horizontal error bars.

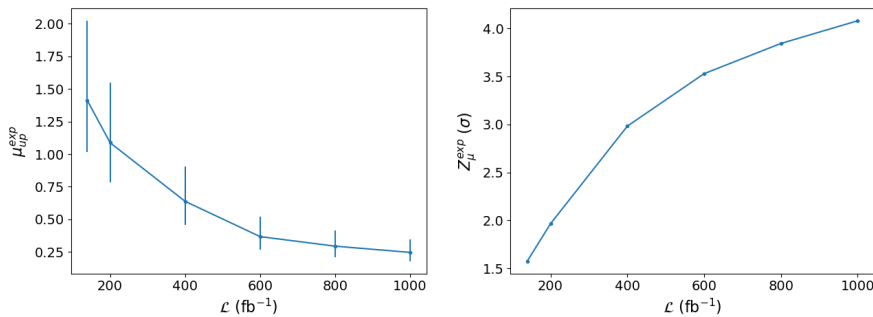


Figure 4.55: The expected upper limit (left) and significance (right) for combined fully blinded fits to the ASIMOV dataset across both the tri- and tetralepton channels for a range integrated luminosities are shown. **Left:** The integrated luminosity, \mathcal{L} , is shown on the x-axis. The expected upper limit, μ_{up}^{exp} , is shown on the y-axis. The vertical lines represent the total uncertainty ($\pm 1\sigma$) on the expected upper limit. **Right:** The integrated luminosity, \mathcal{L} , is shown on the x-axis. The expected significance, Z_μ^{exp} , is shown on the y-axis. The vertical lines represent the total uncertainty ($\pm 1\sigma$) on the expected significance.

1336 rather than the systematic effects. This is evident since increasing the luminosity, therefore increasing the number
1337 of events we see in the detector, directly causes a steady increase in sensitivity.

1338

Chapter 5

1339

Conclusion

1340 The search for tWZ production using 139 fb^{-1} of pp collision data at a centre-of-mass energy of $\sqrt{s} = 13 \text{ TeV}$,
 1341 recorded by the ATLAS experiment at CERN, has been presented. This thesis targeted the tetralepton final state
 1342 channel. To further increase the sensitivity of tWZ , a combined analysis was done across the tetralepton and
 1343 trilepton (studied in an independent analysis by Benjamin Warren (UCT) [66]) channels.

1344 Two SRs and Three CRs were defined. Two SRs, instead of one, were defined in order to suppress and constrain
 1345 the ZZ background. The definition of the tWZ OF SR and the tWZ SF SR take advantage of the OSSF lepton
 1346 pairs which originate from the decay of a Z boson, by requiring that non- Z leptons in the event have the opposite
 1347 and same flavours, for the tWZ OF SR and tWZ SF SR respectively. The resulting SRs successfully separate the
 1348 ZZ background, with the tWZ OF SR containing around 6% of the total ZZ background yield across both regions
 1349 (implying that the remaining $\sim 94\%$ is contained in the tWZ SF SR). The dominant background processes, $t\bar{t}Z$
 1350 and ZZ were constrained by the definition of $t\bar{t}Z$ and ZZ CRs, respectively. The dominant source of fake leptons,
 1351 originating from the $t\bar{t}Z$ background, was constrained by the $(tWZ)_{fake}$ CR, using the MC template method.
 1352

1353 Two BDTs were implemented: an object-level BDT which aims to classify between ℓb systems coming from top
 1354 quarks and an event-level BDT which aims to discriminate between tWZ and our major backgrounds, $t\bar{t}Z$ and
 1355 ZZ . The output from the object-level BDT was converted to an event-level variable to be used as input to
 1356 the event-level BDT. A kinematic reconstruction algorithm, $2\nu\text{SM}$, was used to reconstruct top quarks in order
 1357 to discriminate between tWZ and $t\bar{t}Z$. The output from this algorithm was used as an input variable to the
 1358 event-level BDT. The trained BDT was shown to discriminate well between signal and background events.
 1359

1360 Using a modified ASIMOV dataset in the SRs and real data in the CRs, a blinded maximum-likelihood fit was
 1361 performed across all regions in the tetralepton channel. The best-fit value of the signal strength in the tetralepton
 1362 channel was,

$$\mu(tWZ) = 1.91^{+0.95}_{-0.82} \quad (5.1)$$

1364 with an expected significance of 1.44σ . The expected upper limit on the signal strength of tWZ in the tetralepton
 1365 channel was,

$$\mu_{up}^{exp} = 1.61^{+2.35}_{-1.16} \quad (5.2)$$

1366 Furthermore, a blinded maximum-likelihood fit was performed across all regions across the trilepton and tetralepton
 1367 channels. The best-fit value of the signal strength across both the trilepton and tetralepton channels were,

$$\mu(tWZ) = 1.80^{+0.70}_{-0.65} \quad (5.3)$$

1368 with an expected significance of 1.61σ . The expected upper limit on the signal strength of tWZ across both the
 1369 trilepton and tetralepton channels were,

$$\mu_{up}^{exp} = 1.43^{+2.04}_{-1.03} \quad (5.4)$$

1370 Although this result does not satisfy the 3σ evidence nor the 5σ discovery standards, this is the tightest ever
 1371 constraint on the tWZ process. The results in this analysis are heavily statistically limited, we therefore expect
 1372 that future analyses of this process, using larger datasets (such as that from the HL-LHC), would significantly
 1373 improve the results.

1374

Appendix A

1375

Appendix

1376 A.1 Pre-Fit Plots

1377 A.1.1 tWZ OF SR

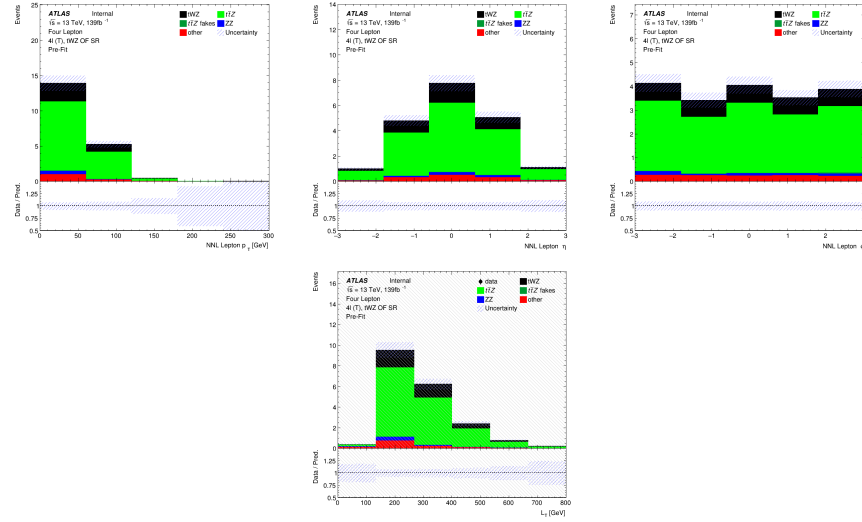


Figure A.1: Top row: MC predictions for p_T , η and ϕ for next-to-next-to-leading (NNL) leptons in the tWZ OF SR region (*blinded*). Bottom row: MC predictions for L_T (scalar sum of lepton p_T) in the tWZ OF SR region (*blinded*)

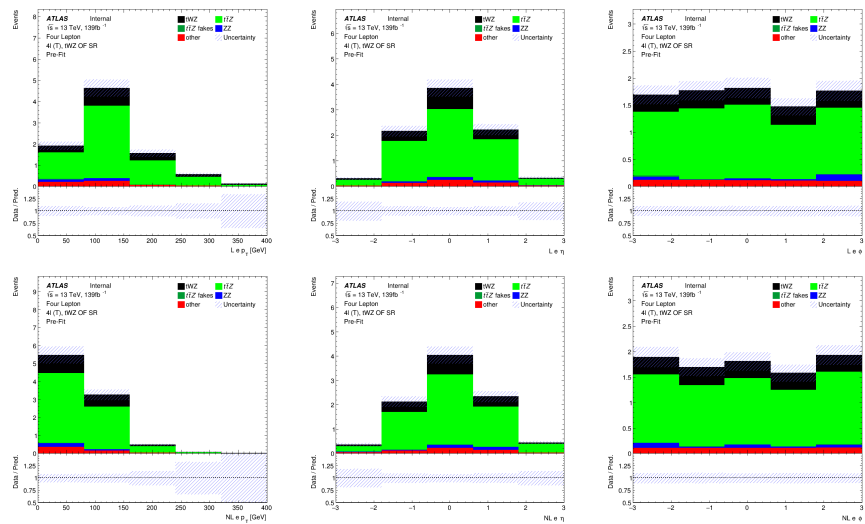


Figure A.2: MC predictions for p_T , η and ϕ for leading (L) electrons (top row) and next-to-leading (NL) electrons (bottom row) in the tWZ OF SR region (*blinded*)

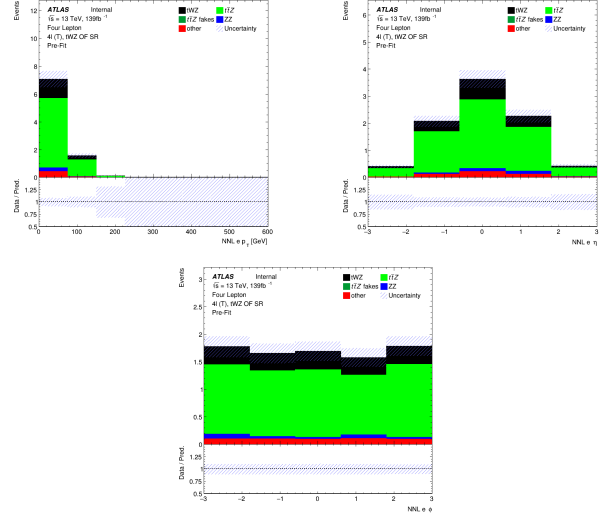


Figure A.3: MC predictions for p_T , η (top row) and ϕ (bottom row) for next-to-next-to-leading (NNL) electrons in the tWZ OF SR region

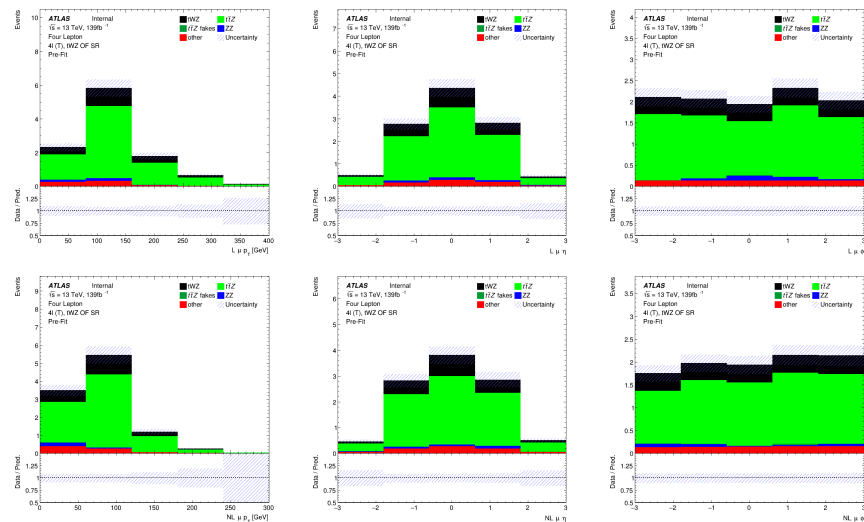


Figure A.4: MC predictions for p_T , η and ϕ for leading (L) muons (top row) and next-to-leading (NL) muons (bottom row) in the tWZ OF SR region (*blinded*)

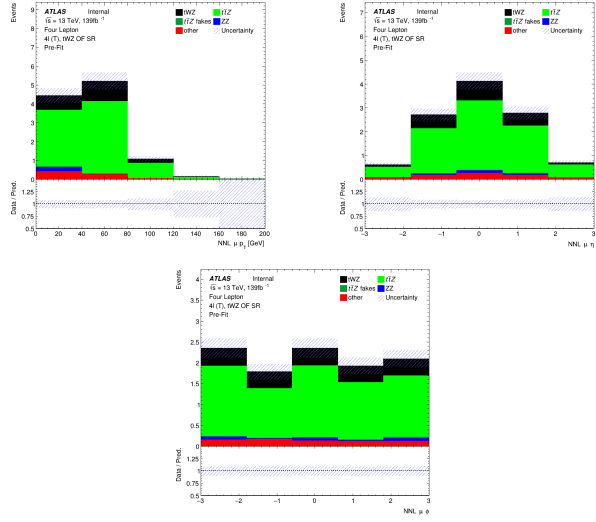


Figure A.5: MC predictions for p_T , η (top row) and ϕ (bottom row) for next-to-next-to-leading (NNL) muons in the tWZ OF SR region (*blinded*)

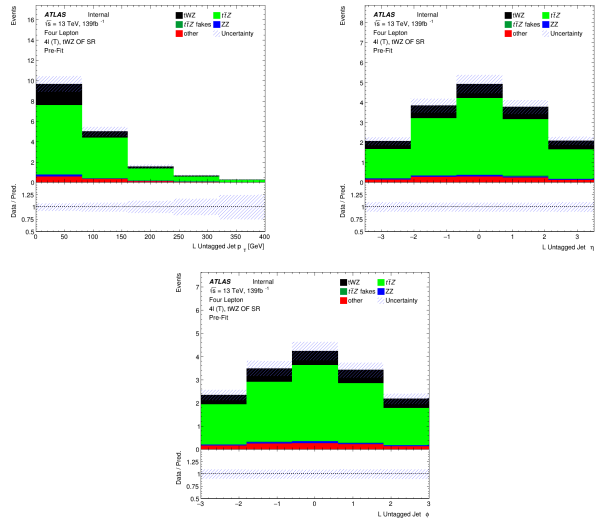


Figure A.6: MC predictions for p_T , η (top row) and ϕ (bottom row) for untagged jets in the tWZ OF SR region (*blinded*)

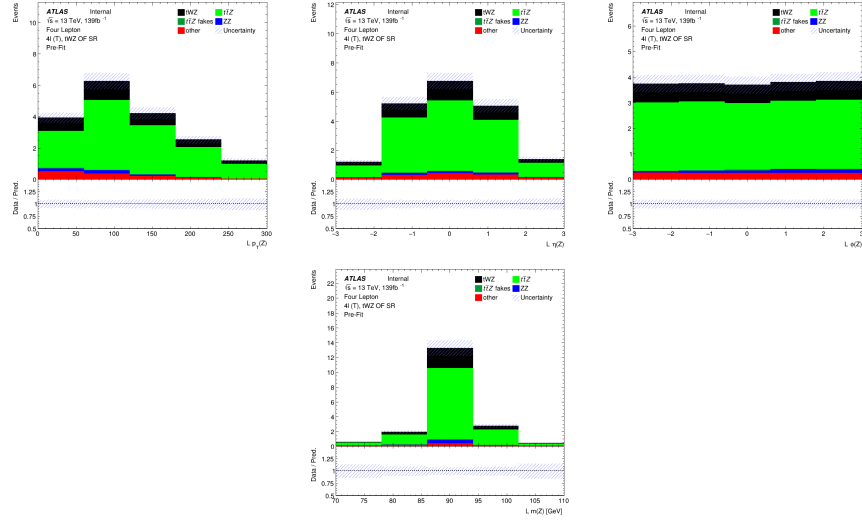


Figure A.7: MC predictions for p_T , η , ϕ (top row) and mass (m_Z) (bottom row) of the leading reconstructed Z candidate (OSSF lepton pair with $|m_{\text{OSSF}} - m(Z)| < 30 \text{ GeV}$) in the tWZ OF SR region (*blinded*)

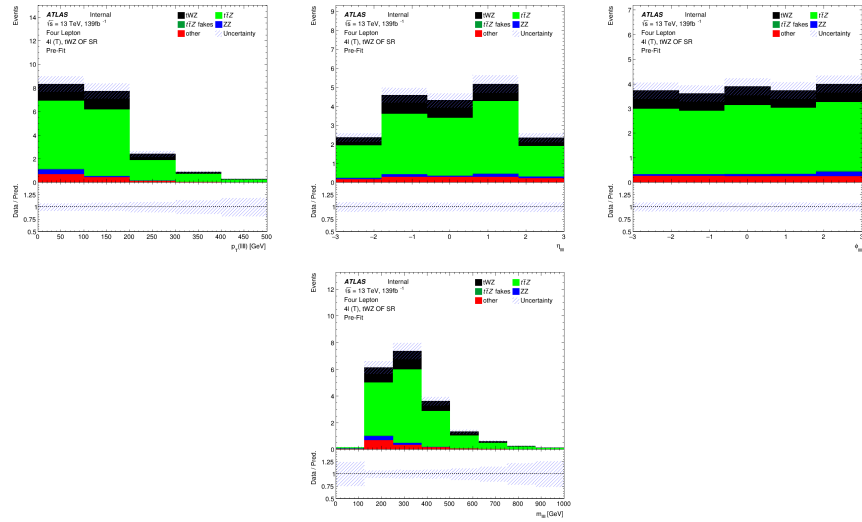


Figure A.8: MC predictions for p_T , η , ϕ (top row) and mass (bottom row) of the lepton system ($\ell\ell\ell\ell$) in the tWZ OF SR region (*blinded*)

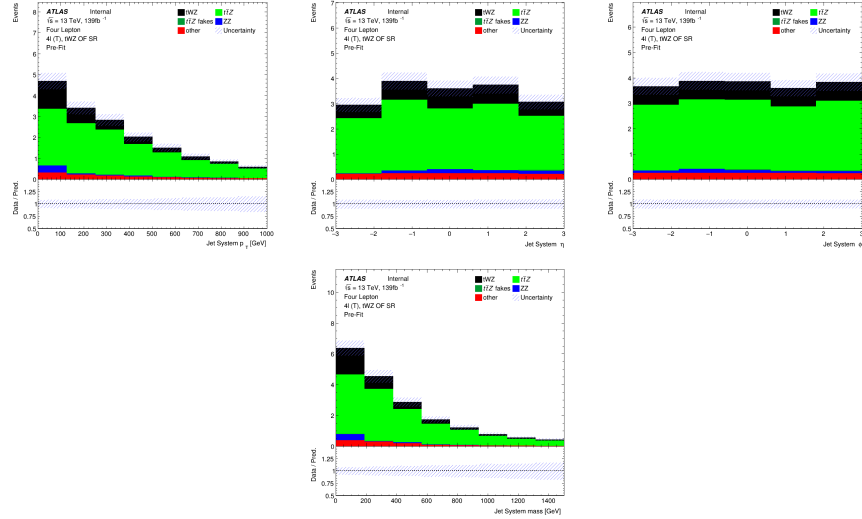


Figure A.9: MC predictions for p_T , η , ϕ (top row) and mass (bottom row) of the jet systems in the tWZ OF SR region (*blinded*)

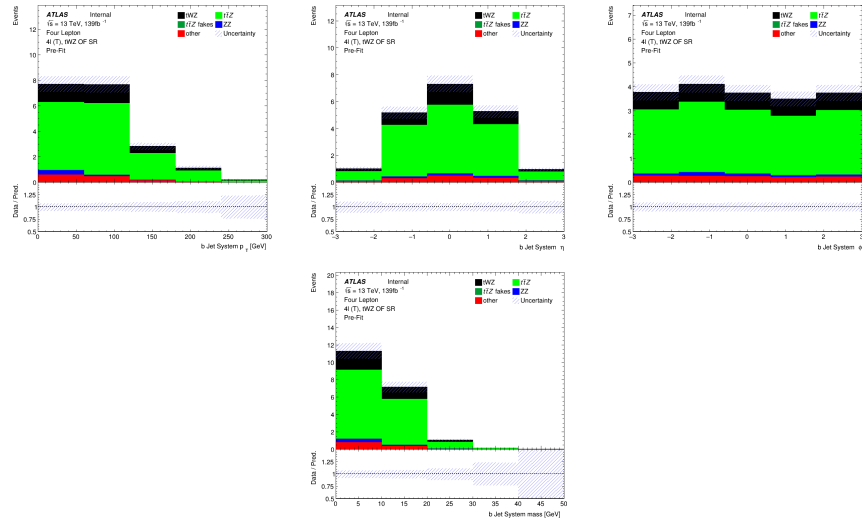


Figure A.10: MC predictions for p_T , η , ϕ (top row) and mass (bottom row) of the b-tagged jet systems in the tWZ OF SR region (*blinded*)

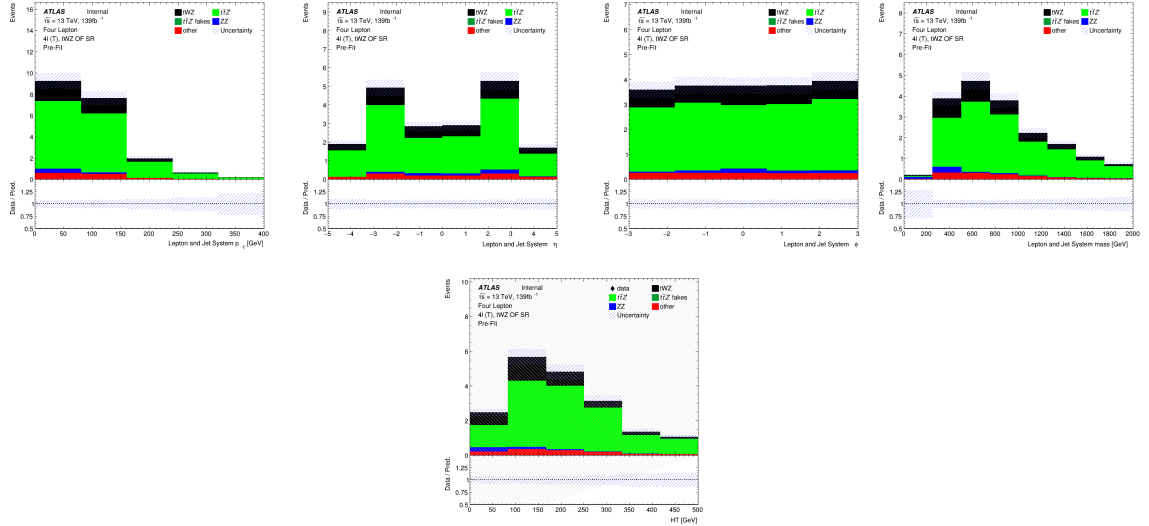


Figure A.11: MC predictions for p_T , η and ϕ (top row) and mass (bottom left) for the lepton + jet systems ($\ell\ell\ell\ell$ + jets) in the tWZ OF SR region (*blinded*). Bottom right: MC predictions for H_T (scalar sum of jet p_T and lepton p_T) in the tWZ OF SR region (*blinded*)

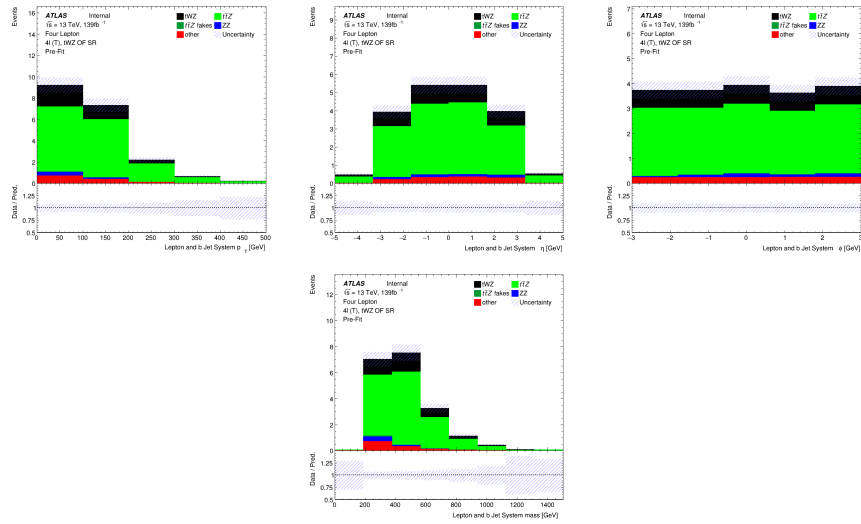


Figure A.12: MC predictions for p_T , η , ϕ (top row) and mass (bottom row) of the lepton + b-tagged jet systems ($\ell\ell\ell\ell$ + b-tagged jets) in the tWZ OF SR region (*blinded*)

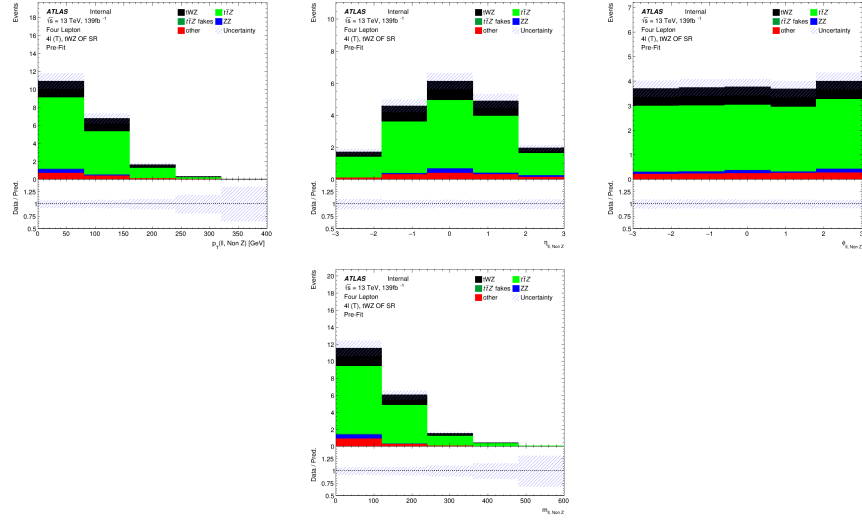


Figure A.13: MC predictions for p_T , η , ϕ (top row) and mass (bottom row) of reconstructed Non Z leptons (lepton pairs which don't originate from a Z candidate) in the tWZ OF SR region (*blinded*)

1378 A.1.2 tWZ SF SR

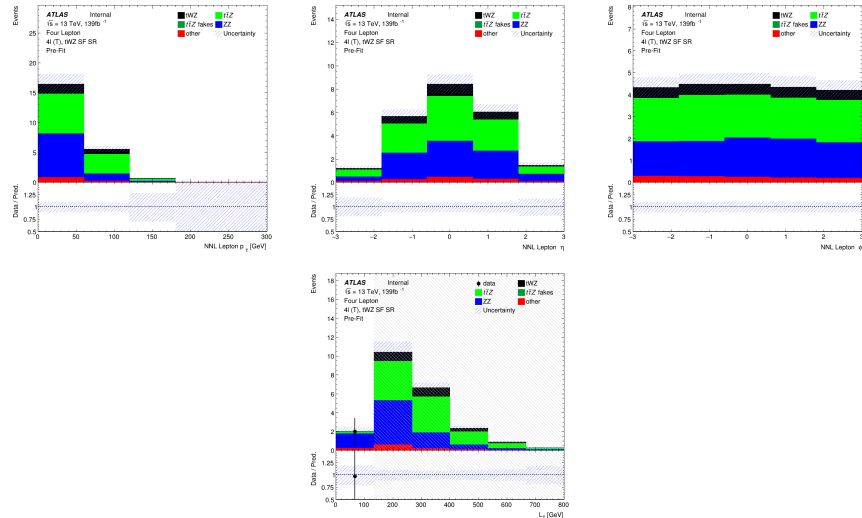


Figure A.14: Top row: MC predictions for p_T , η and ϕ for next-to-next-to-leading (NNL) leptons in the tWZ SF SR region (*blinded*). Bottom row: MC prediction for L_T (scalar sum of lepton p_T) in the tWZ SF SR region (*blinded*)

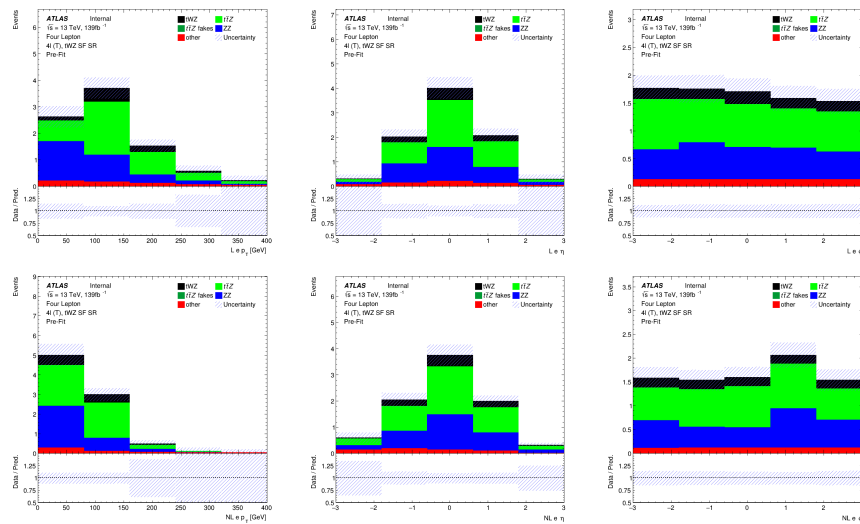


Figure A.15: MC predictions for p_T , η and ϕ for leading (L) electrons (top row) and next-to-leading (NL) electrons (bottom row) in the tWZ SF SR region (*blinded*)

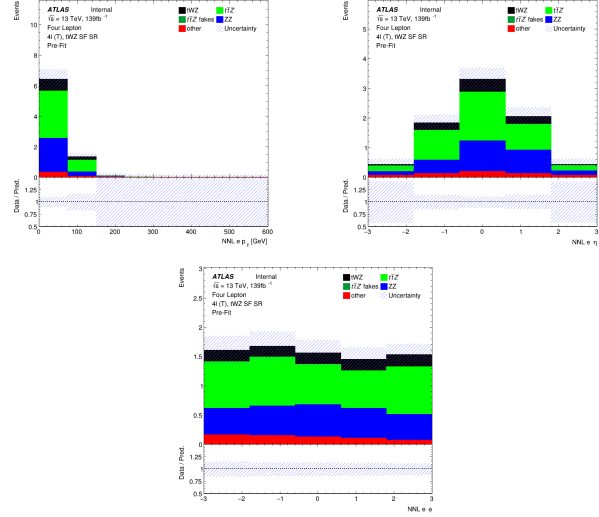


Figure A.16: MC predictions for p_T , η (top row) and ϕ (bottom row) for next-to-next-to-leading (NNL) electrons in the tWZ SF SR region

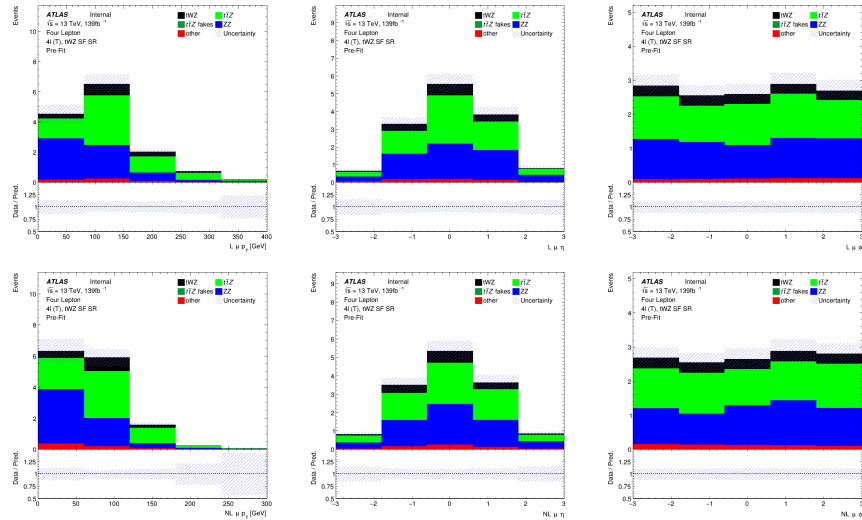


Figure A.17: MC predictions for p_T , η and ϕ for leading (L) muons (top row) and next-to-leading (NL) muons (bottom row) in the tWZ SF SR region (*blinded*)

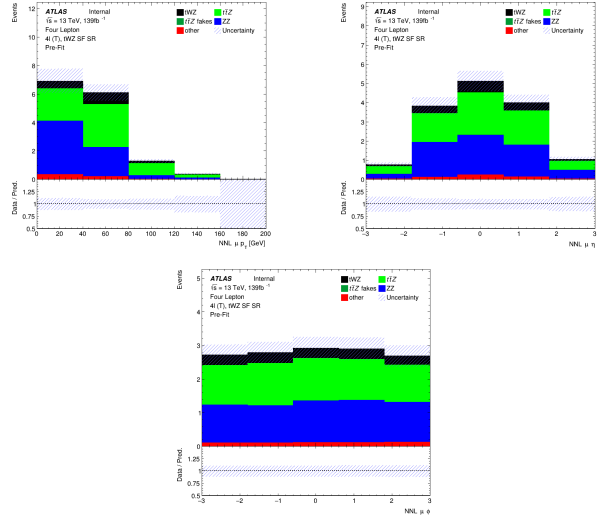


Figure A.18: MC predictions for p_T , η (top row) and ϕ (bottom row) for next-to-next-to-leading (NNL) muons in the tWZ SF SR region (*blinded*)

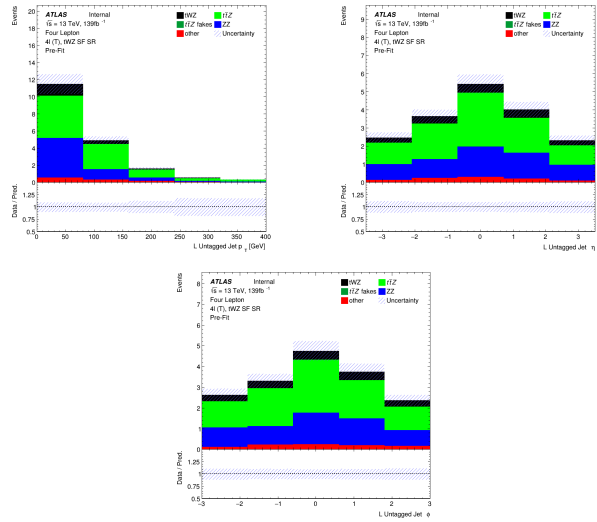


Figure A.19: MC predictions for p_T , η (top row) and ϕ (bottom row) for untagged jets in the tWZ SF SR region (*blinded*)

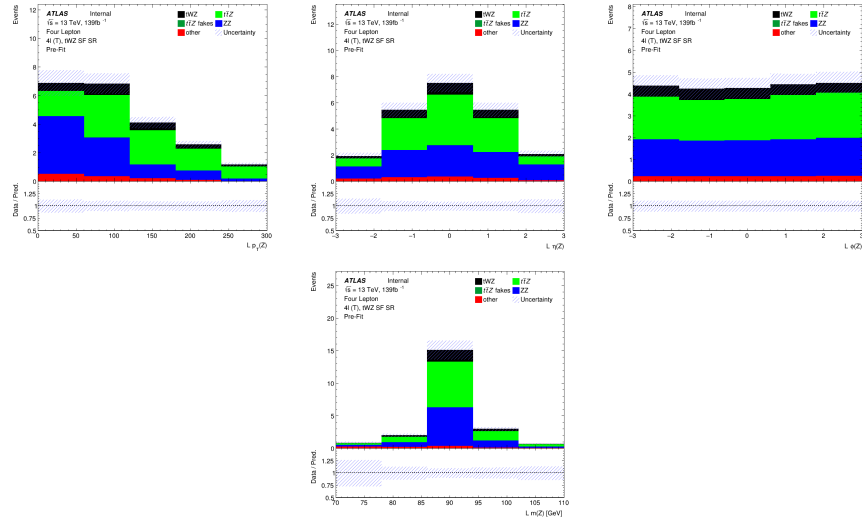


Figure A.20: MC predictions for p_T , η , ϕ (top row) and mass (m_Z) (bottom row) of the leading reconstructed Z candidate (OSSF lepton pair with $|m_{\text{OSSF}} - m(Z)| < 30$ GeV) in the tWZ SF SR region (*blinded*)

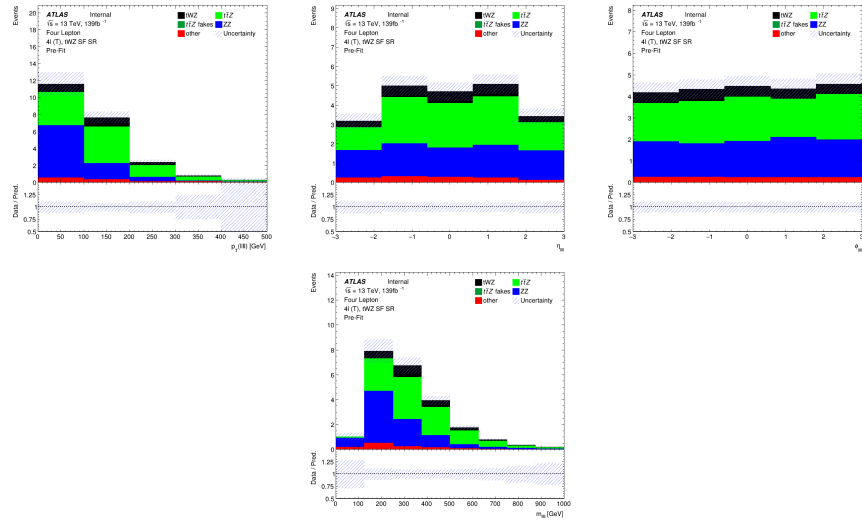


Figure A.21: MC predictions for p_T , η , ϕ (top row) and mass (bottom row) of the lepton system ($\ell\ell\ell\ell$) in the tWZ SF SR region (*blinded*)

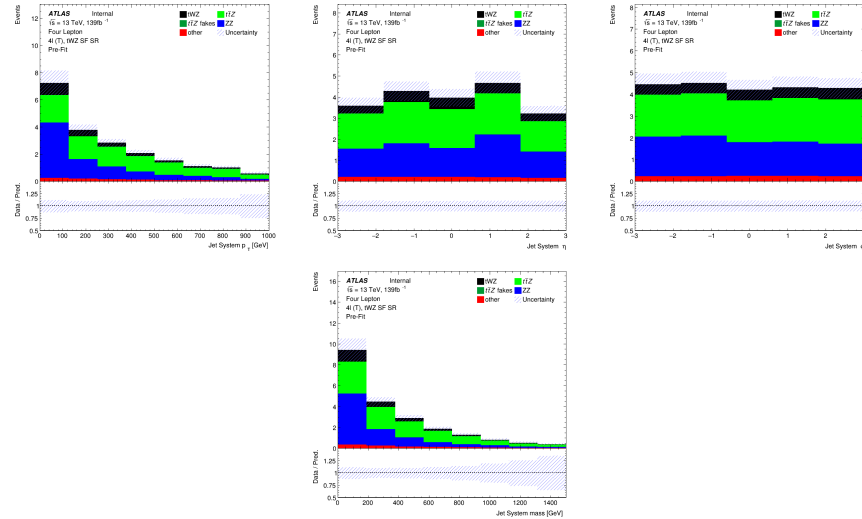


Figure A.22: MC predictions for p_T , η , ϕ (top row) and mass (bottom row) of the jet systems in the tWZ SF SR region (*blinded*)

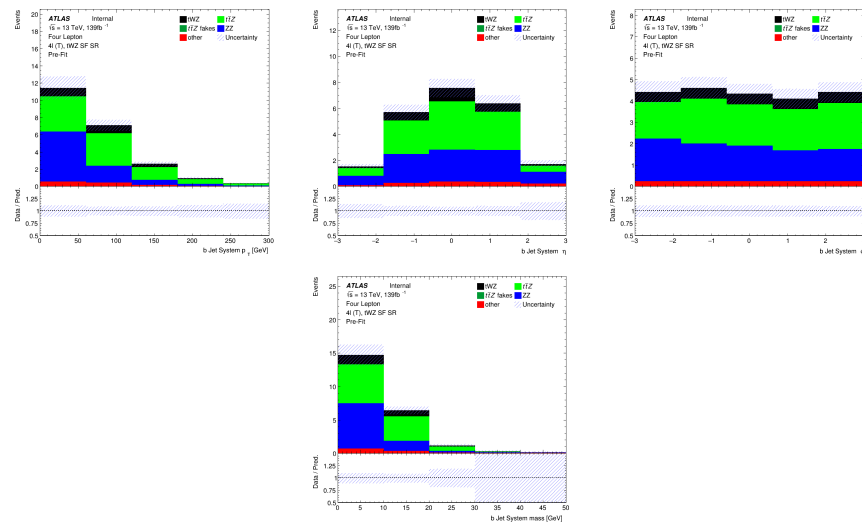


Figure A.23: MC predictions for p_T , η , ϕ (top row) and mass (bottom row) of the b-tagged jet systems in the tWZ SF SR region (*blinded*)

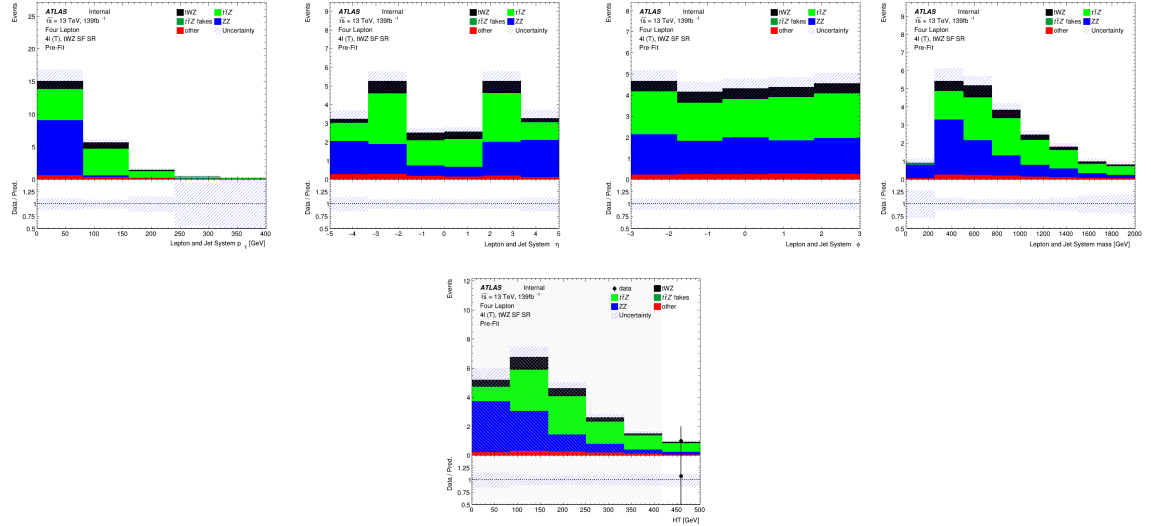


Figure A.24: MC predictions for p_T , η and ϕ (top row) and mass (bottom left) for the lepton + jet systems ($\ell\ell\ell\ell$ + jets) in the tWZ SF SR region (*blinded*). Bottom right: MC predictions for H_T (scalar sum of jet p_T and lepton p_T) in the tWZ SF SR region (*blinded*)

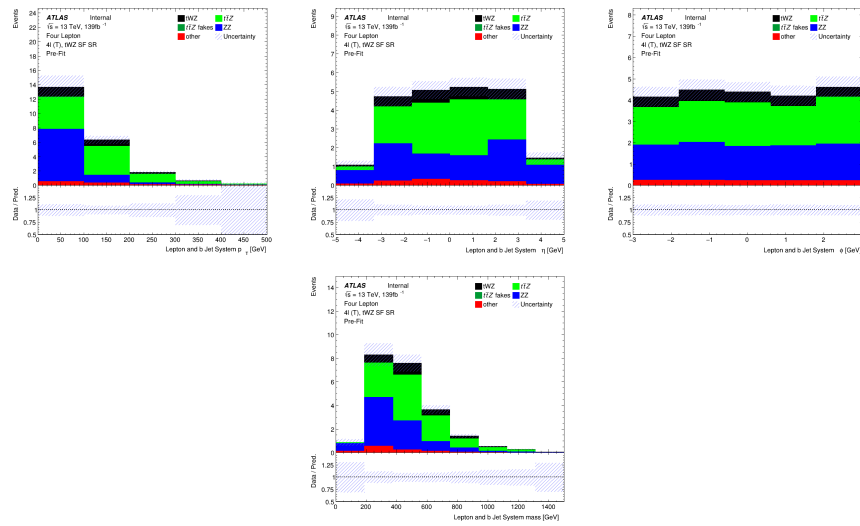


Figure A.25: MC predictions for p_T , η , ϕ (top row) and mass (bottom row) of the lepton + b-tagged jet systems ($\ell\ell\ell\ell$ + b-tagged jets) in the tWZ SF SR region (*blinded*)

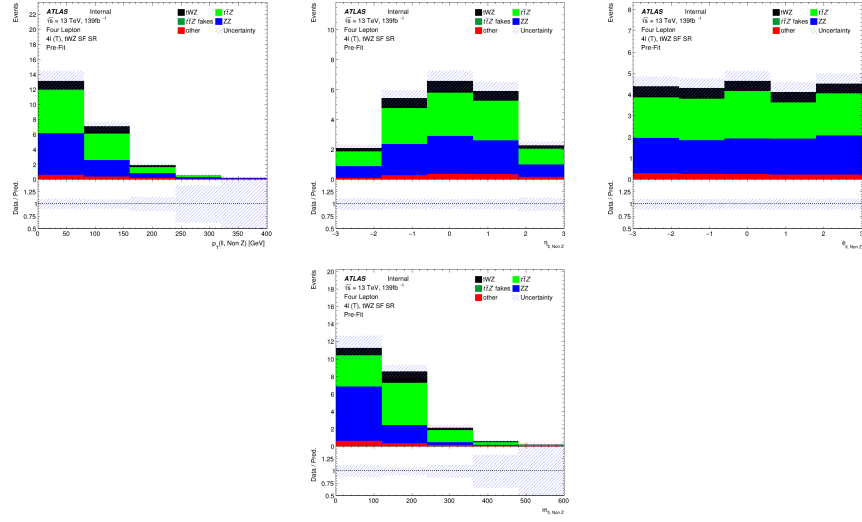


Figure A.26: MC predictions for p_T , η , ϕ (top row) and mass (bottom row) of reconstructed Non Z leptons (lepton pairs which don't originate from a Z candidate) in the tWZ SF SR region (*blinded*)

1379 A.1.3 $t\bar{t}Z$ CR

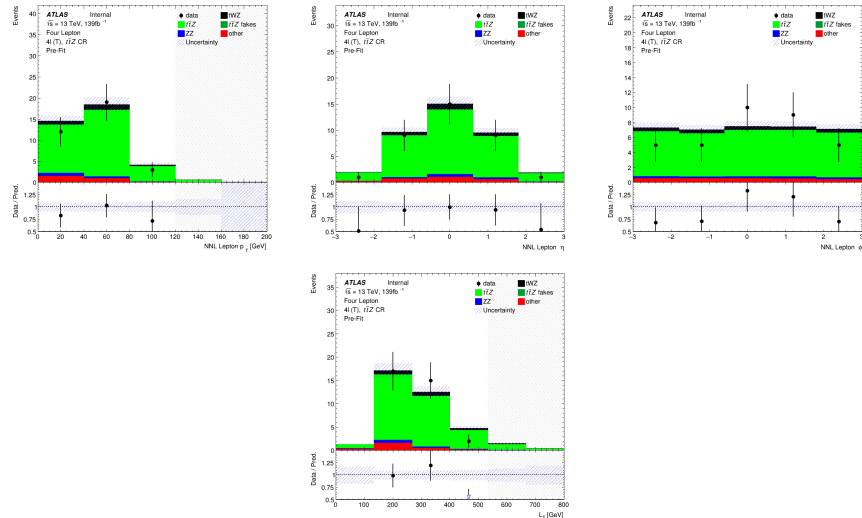


Figure A.27: Top row: MC predictions for p_T , η and ϕ for next-to-next-to-leading (NNL) leptons in the $t\bar{t}Z$ CR region . Bottom row: MC predictions for L_T (scalar sum of lepton p_T) in the $t\bar{t}Z$ CR region

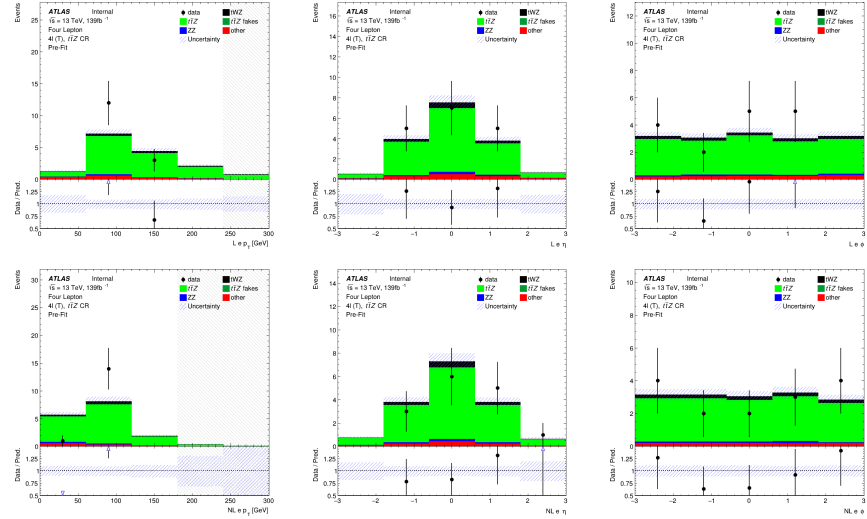


Figure A.28: MC predictions for p_T , η and ϕ for leading (L) electrons (top row) and next-to-leading (NL) electrons (bottom row) in the $t\bar{t}Z$ CR region

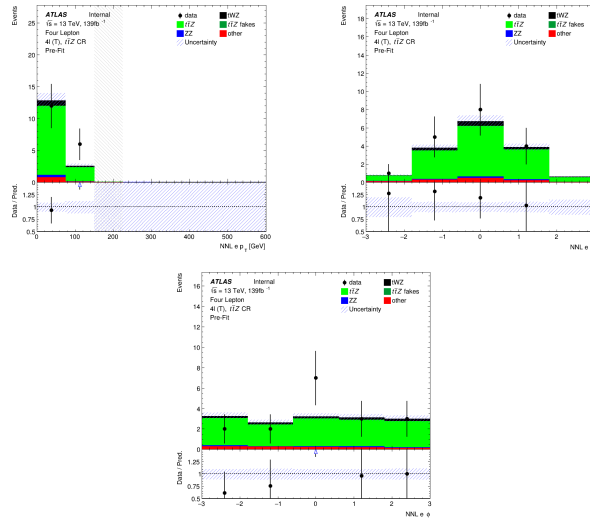


Figure A.29: MC predictions for p_T , η (top row) and ϕ (bottom row) for next-to-next-to-leading (NNL) electrons in the $t\bar{t}Z$ CR region

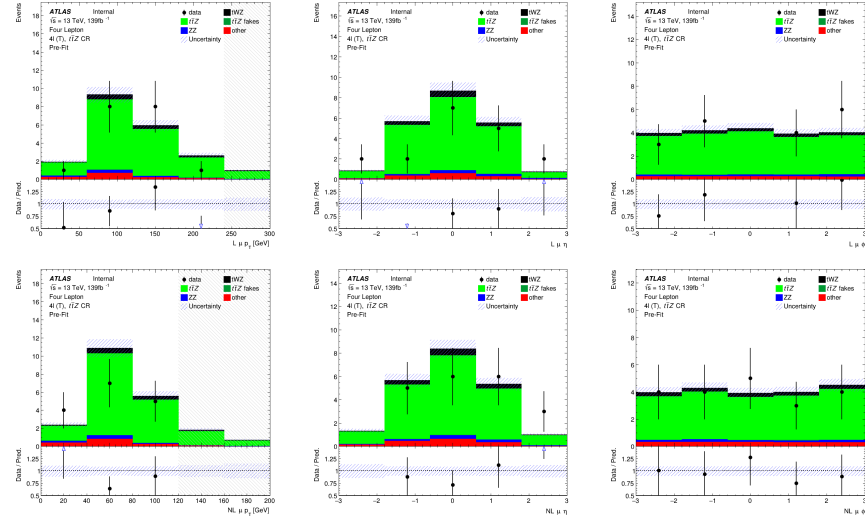


Figure A.30: MC predictions for p_T , η and ϕ for leading (L) muons (top row) and next-to-leading (NL) muons (bottom row) in the $t\bar{t}Z$ CR region

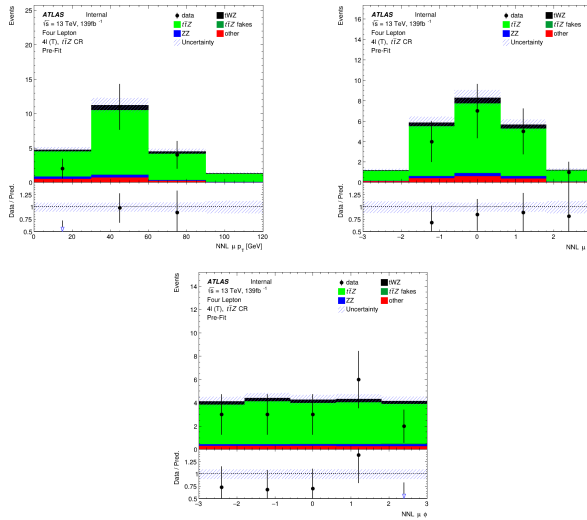


Figure A.31: MC predictions for p_T , η (top row) and ϕ (bottom row) for next-to-next-to-leading (NNL) muons in the $t\bar{t}Z$ CR region

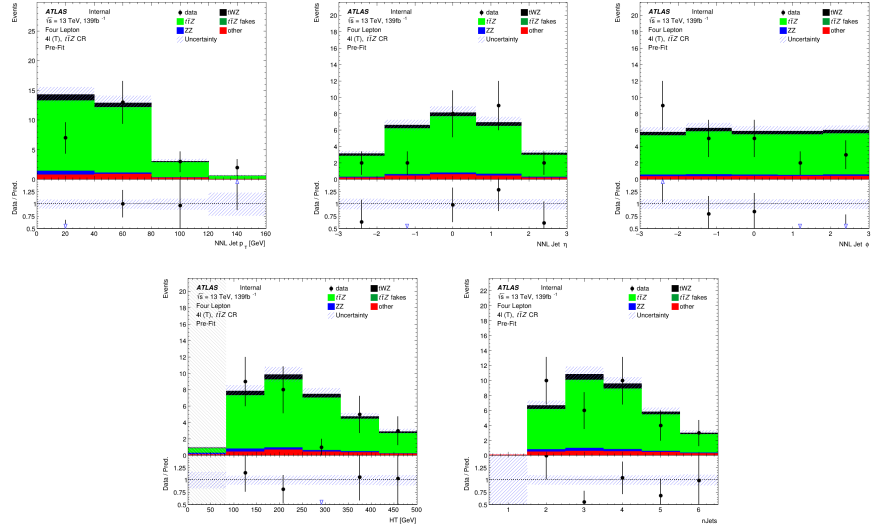


Figure A.32: Top row: MC predictions for p_T , η and ϕ for next-to-next-to-leading (NNL) jets in the $t\bar{t}Z$ CR region. . Bottom row: MC predictions for H_T (scalar sum of Jet p_T) (left) and the Number of jets (right) in the $t\bar{t}Z$ CR region

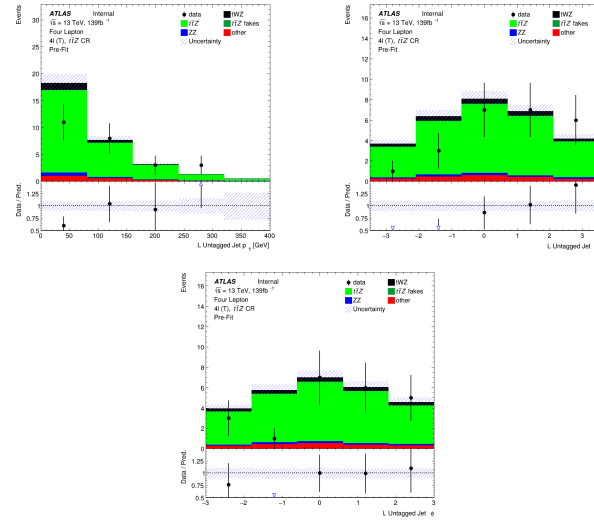


Figure A.33: MC predictions for p_T , η (top row) and ϕ (bottom row) for untagged jets in the $t\bar{t}Z$ CR region

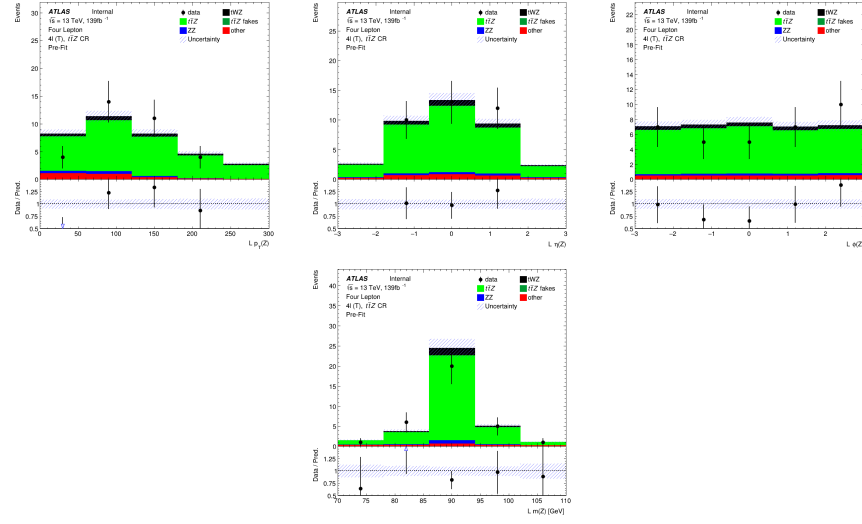


Figure A.34: MC predictions for p_T , η , ϕ (top row) and mass (m_Z) (bottom row) of reconstructed leading Z candidates (OSSF lepton pair with $|m_{\text{OSSF}} - m(Z)| < 30 \text{ GeV}$) in the $t\bar{t}Z$ CR region

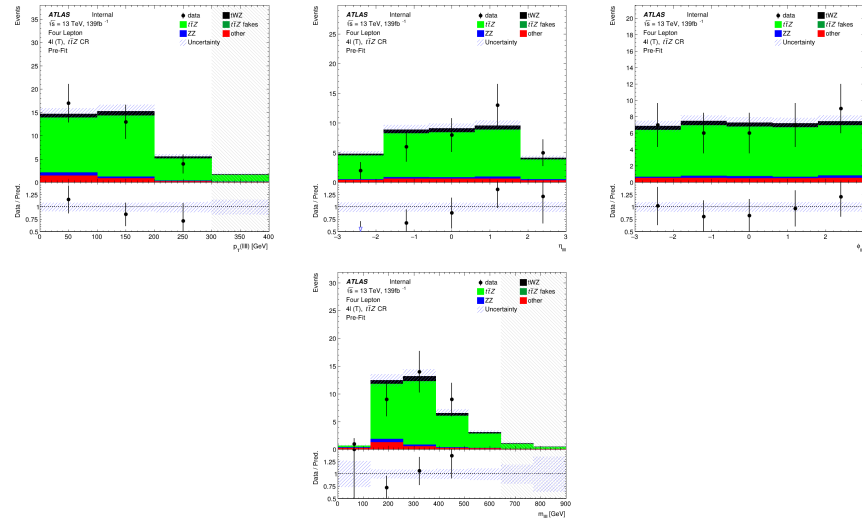


Figure A.35: MC predictions for p_T , η , ϕ (top row) and mass (bottom row) of the lepton system ($\ell\ell\ell\ell$) in the $t\bar{t}Z$ CR region

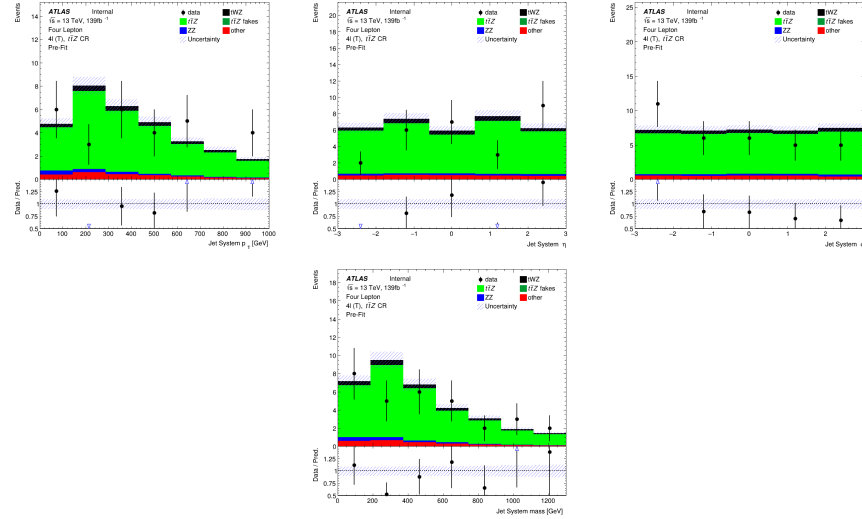


Figure A.36: MC predictions for p_T , η , ϕ (top row) and mass (bottom row) of the jet systems in the $t\bar{t}Z$ CR region

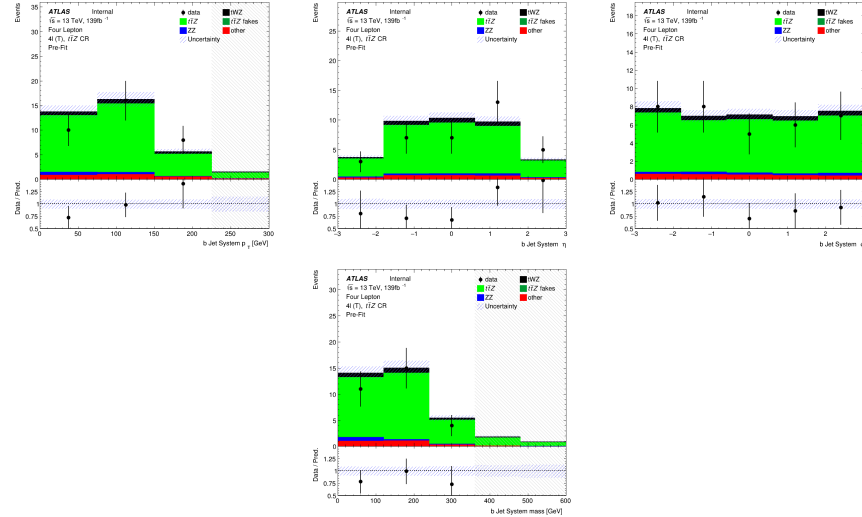


Figure A.37: MC predictions for p_T , η , ϕ (top row) and mass (bottom row) of the b-tagged jet systems in the $t\bar{t}Z$ CR region

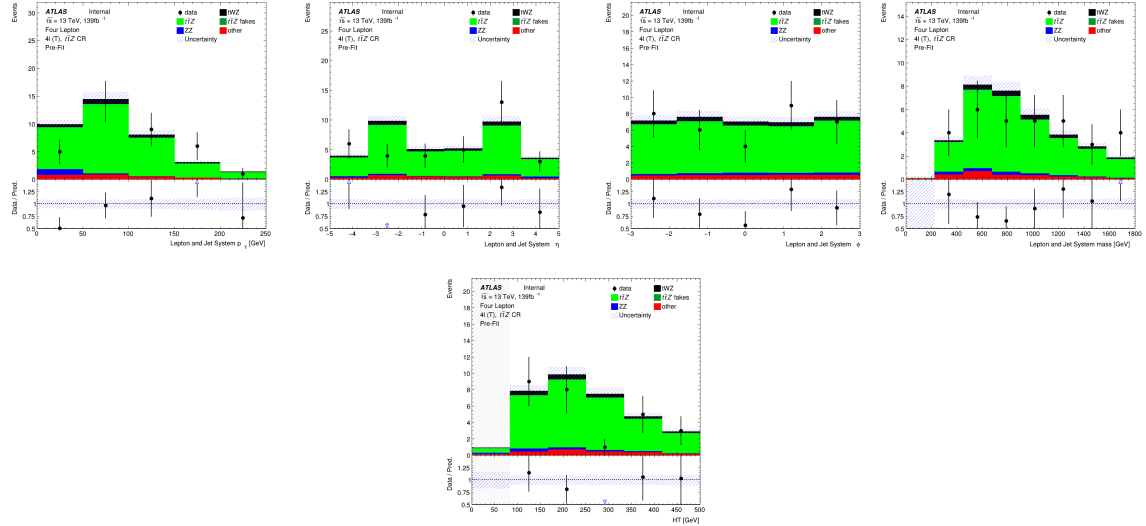


Figure A.38: MC predictions for p_T , η and ϕ (top row) and mass (bottom left) for the lepton + jet systems ($\ell\ell\ell\ell$ + jets) in the $t\bar{t}Z$ CR region . Bottom right: MC predictions for H_T (scalar sum of jet p_T and lepton p_T) in the $t\bar{t}Z$ CR region

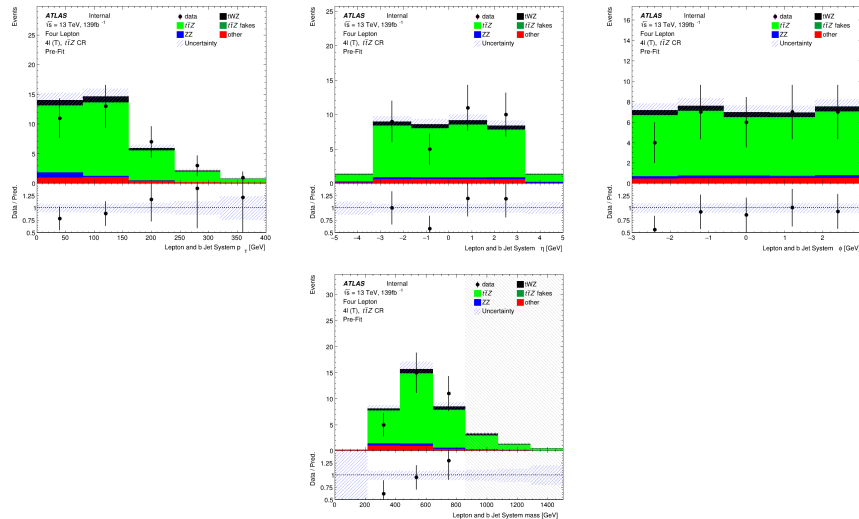


Figure A.39: MC predictions for p_T , η , ϕ (top row) and mass (bottom row) of the lepton + b-tagged jet systems ($\ell\ell\ell\ell$ + b-tagged jets) in the $t\bar{t}Z$ CR region

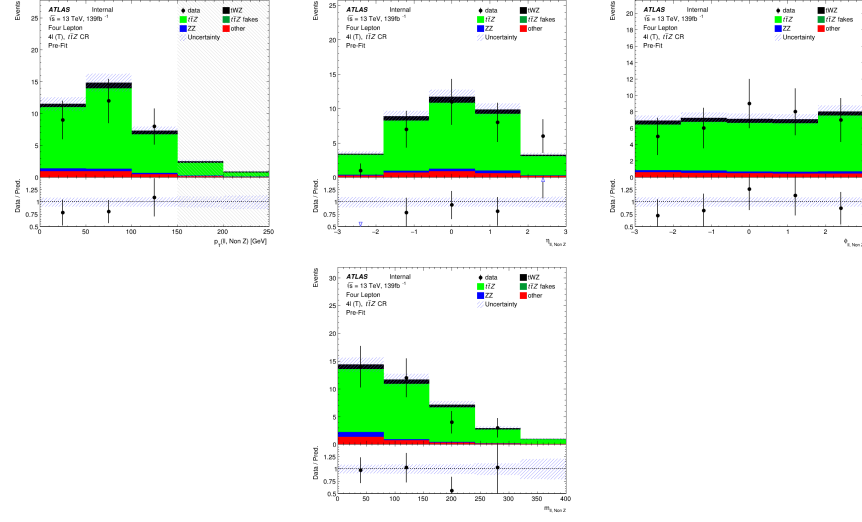


Figure A.40: MC predictions for p_T , η , ϕ (top row) and mass (bottom row) of reconstructed Non Z leptons (lepton pairs which don't originate from a Z candidate) in the $t\bar{t}Z$ CR region

1380 A.1.4 ZZb CR

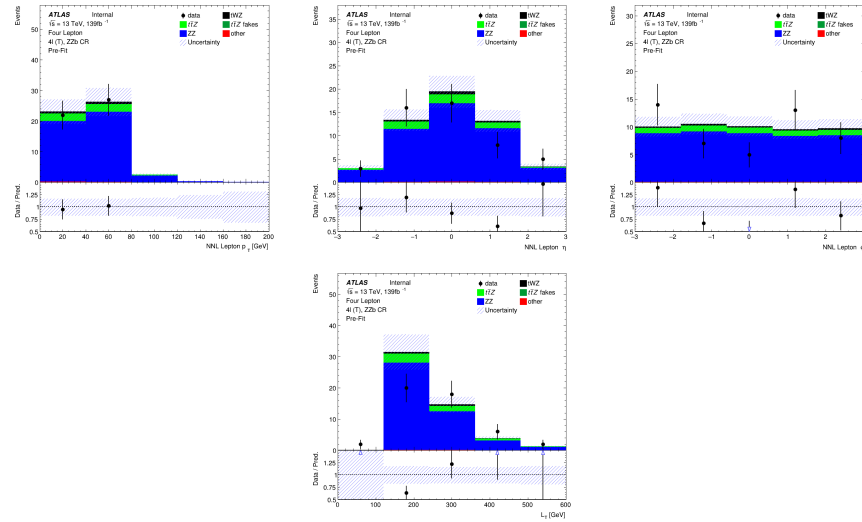


Figure A.41: Top row: MC predictions for p_T , η and ϕ for next-to-next-to-leading (NNL) leptons in the ZZb CR region . Bottom row: MC predictions for L_T (scalar sum of lepton p_T) in the ZZb CR region

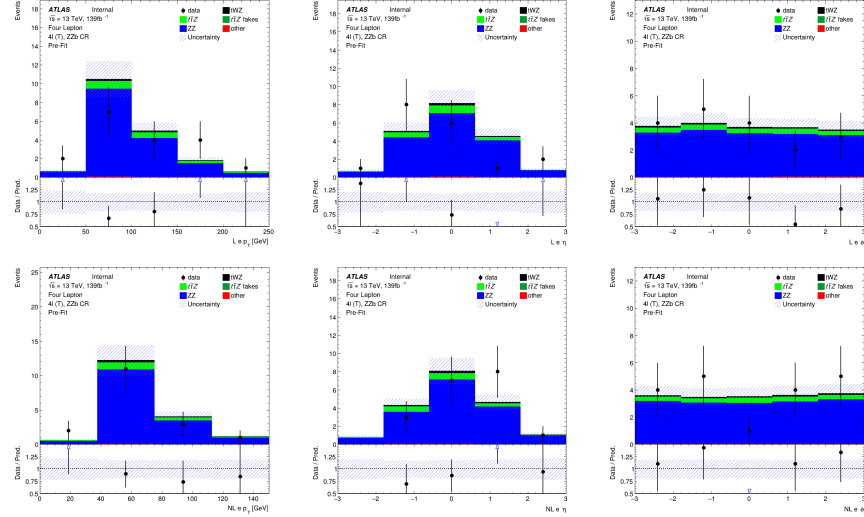


Figure A.42: MC predictions for p_T , η and ϕ for leading (L) electrons (top row) and next-to-leading (NL) electrons (bottom row) in the ZZb CR region

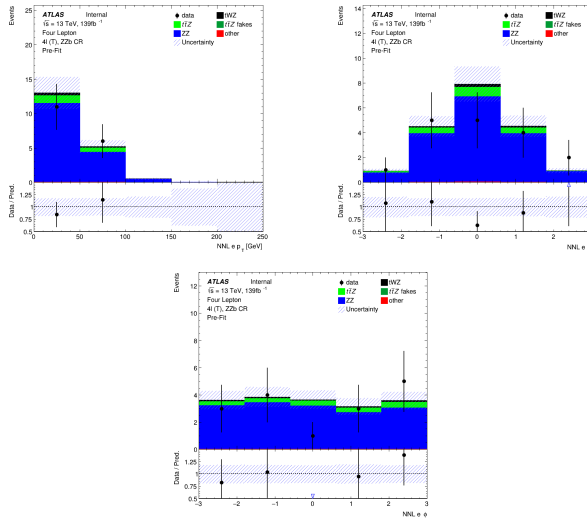


Figure A.43: MC predictions for p_T , η (top row) and ϕ (bottom row) for next-to-next-to-leading (NNL) electrons in the ZZb CR region

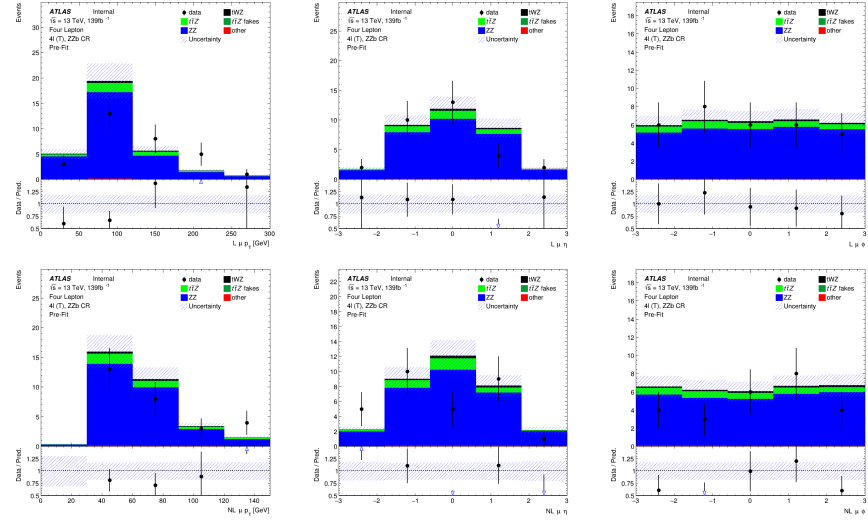


Figure A.44: MC predictions for p_T , η and ϕ for leading (L) muons (top row) and next-to-leading (NL) muons (bottom row) in the ZZb CR region

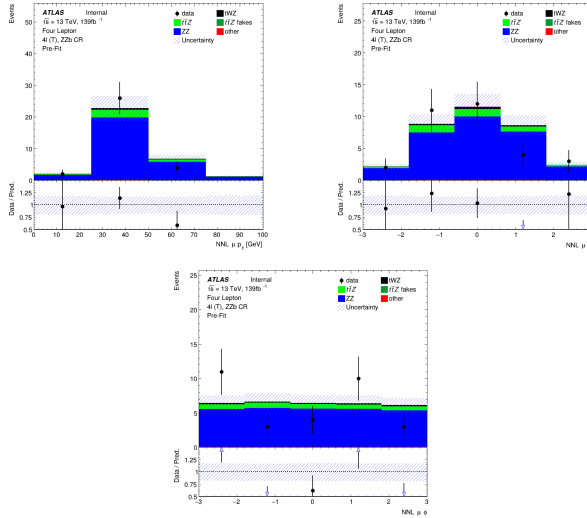


Figure A.45: MC predictions for p_T , η (top row) and ϕ (bottom row) for next-to-next-to-leading (NNL) muons in the ZZb CR region

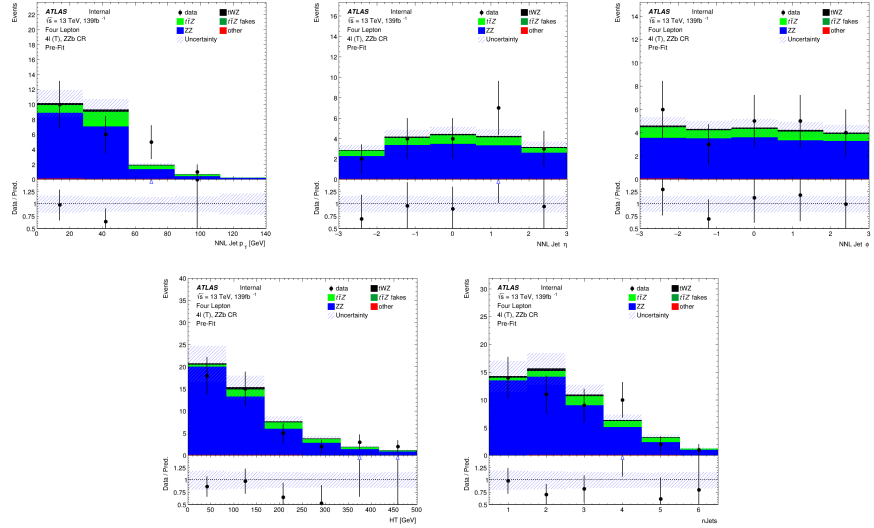


Figure A.46: Top row: MC predictions for p_T , η and ϕ for next-to-next-to-leading (NNL) jets in the ZZb CR region . . Bottom row: MC predictions for H_T (scalar sum of Jet p_T) (left) and the Number of jets (right) in the ZZb CR region

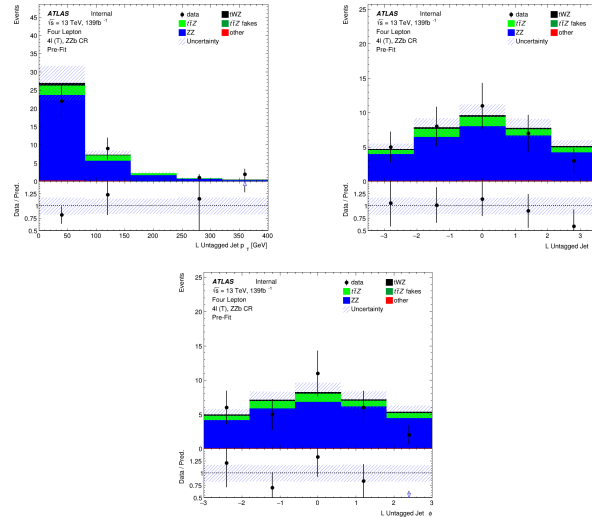


Figure A.47: MC predictions for p_T , η (top row) and ϕ (bottom row) for untagged jets in the ZZb CR region

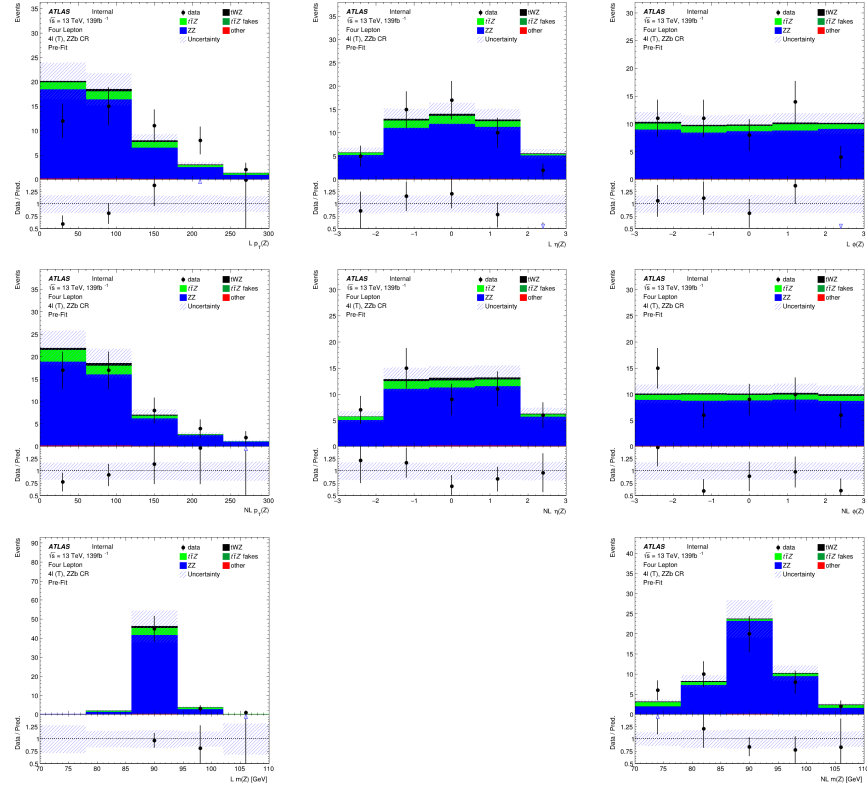


Figure A.48: MC predictions for p_T , η , ϕ of the leading (top row), next-to-leading (middle row) and mass (m_Z) (bottom row) of reconstructed Z candidates (OSSF lepton pair with $|m_{\text{OSSF}} - m(Z)| < 30 \text{ GeV}$) in the ZZb CR region

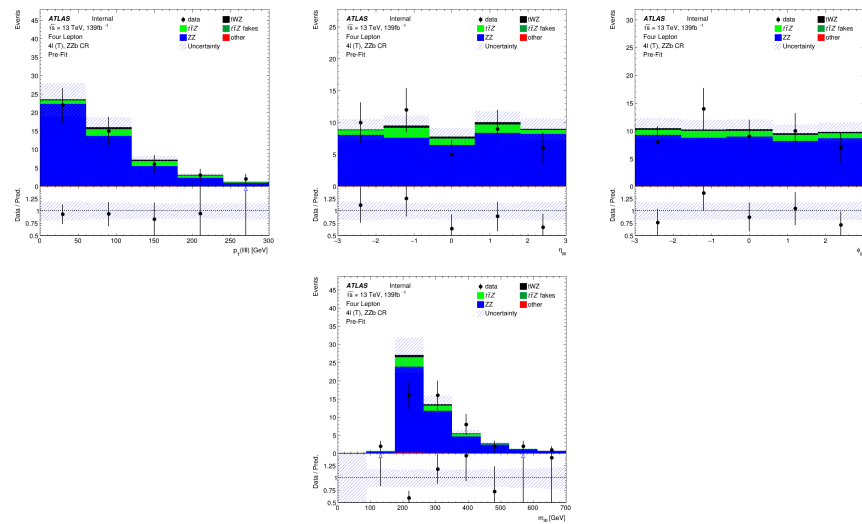


Figure A.49: MC predictions for p_T , η , ϕ (top row) and mass (bottom row) of the lepton system ($\ell\ell\ell\ell$) in the ZZ CR region

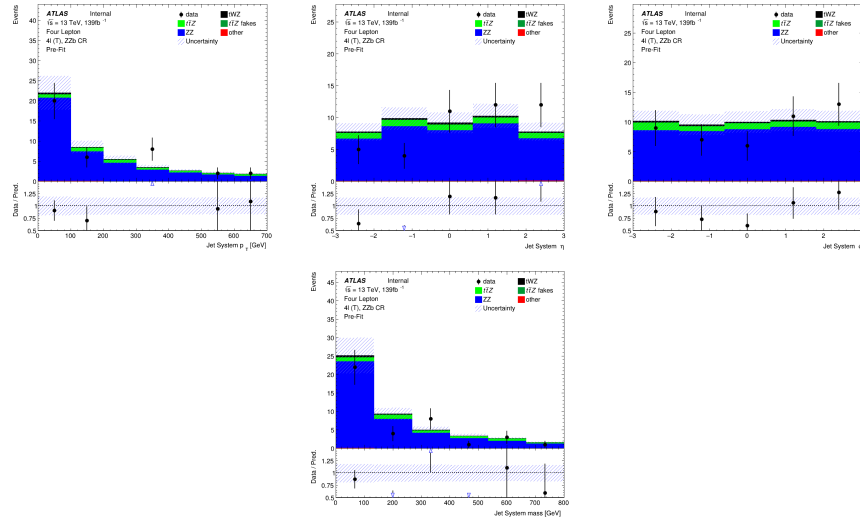


Figure A.50: MC predictions for p_T , η , ϕ (top row) and mass (bottom row) of the jet systems in the ZZb CR region

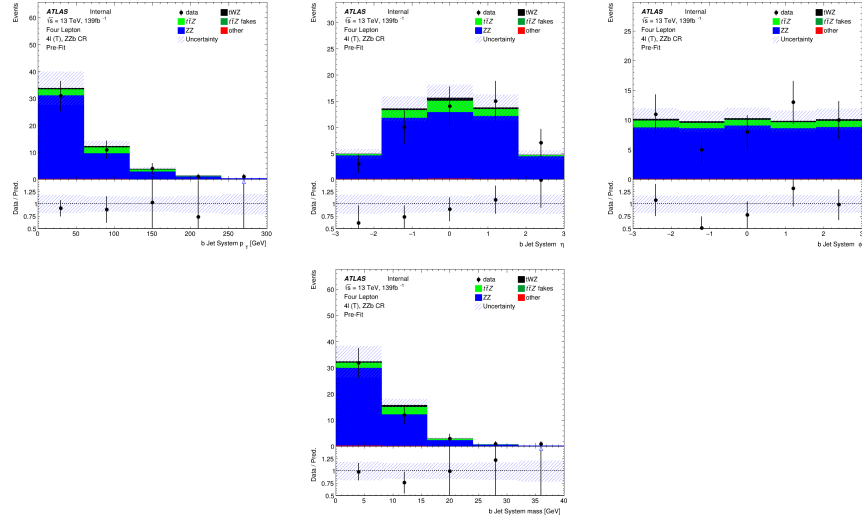


Figure A.51: MC predictions for p_T , η , ϕ (top row) and mass (bottom row) of the b-tagged jet systems in the ZZb CR region

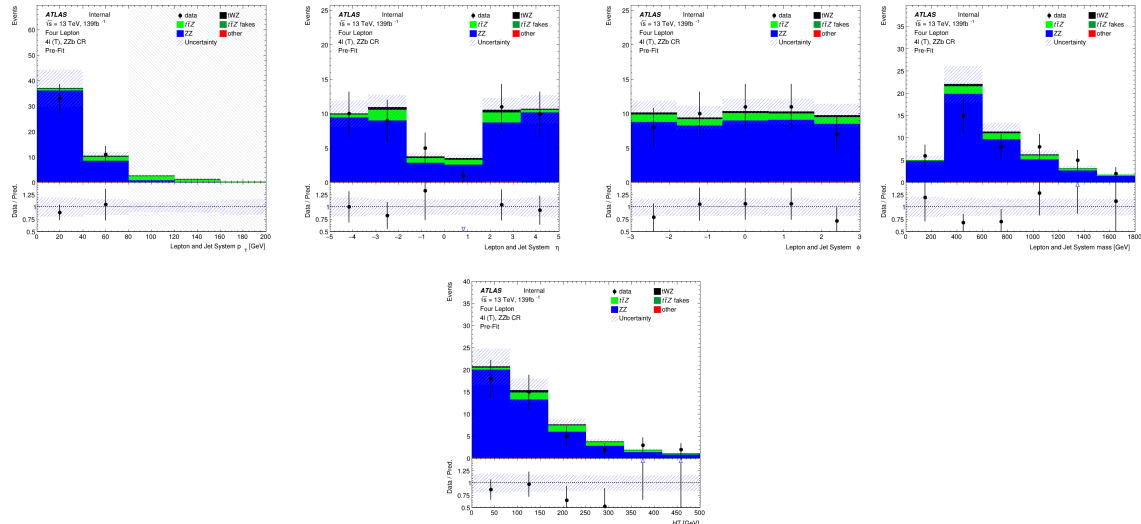


Figure A.52: MC predictions for p_T , η and ϕ (top row) and mass (bottom left) for the lepton + jet systems ($\ell\ell\ell\ell + \text{jets}$) in the ZZb CR region . Bottom right: MC predictions for H_T (scalar sum of jet p_T and lepton p_T) in the ZZb CR region

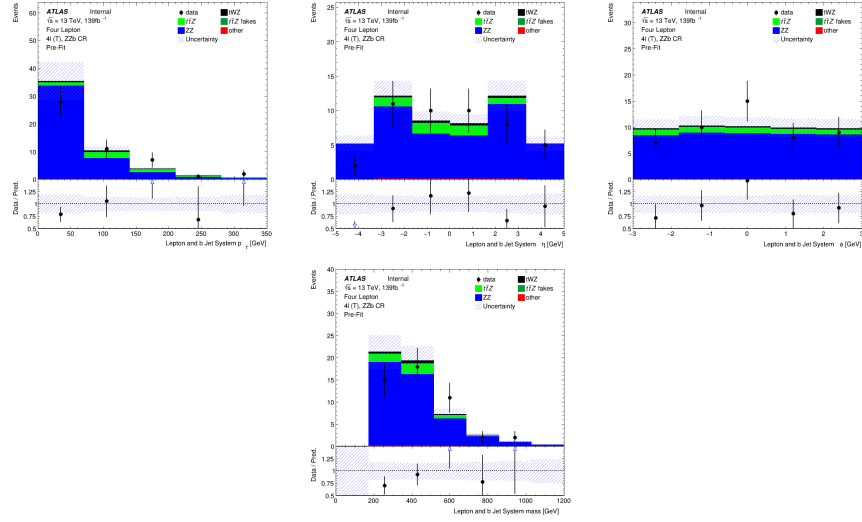


Figure A.53: MC predictions for p_T , η , ϕ (top row) and mass (bottom row) of the lepton + b-tagged jet systems ($\ell\ell\ell\ell + \text{b-tagged jets}$) in the ZZb CR region

1381 A.1.5 $(tWZ)_\text{fake}$ CR

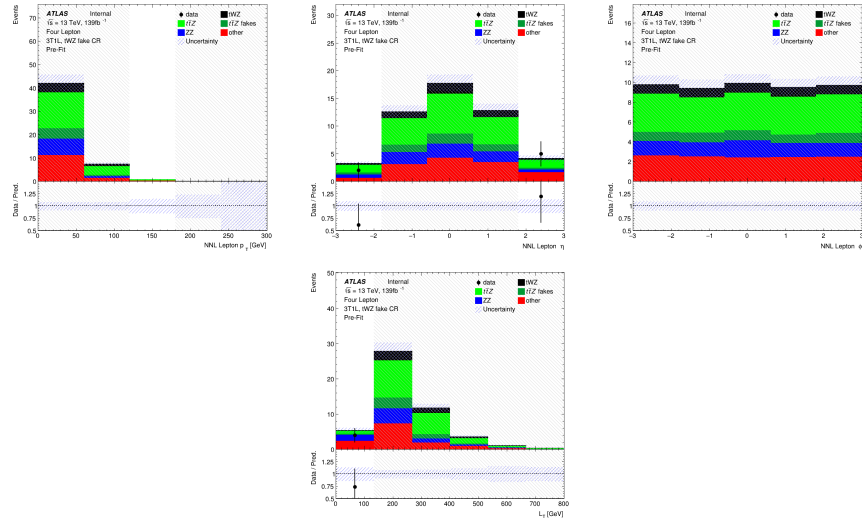


Figure A.54: Top row: MC predictions for p_T , η and ϕ for next-to-next-to-leading (NNL) leptons in the $(tWZ)_\text{fake}$ CR region . Bottom row: MC predictions for L_T (scalar sum of lepton p_T) in the $(tWZ)_\text{fake}$ CR region

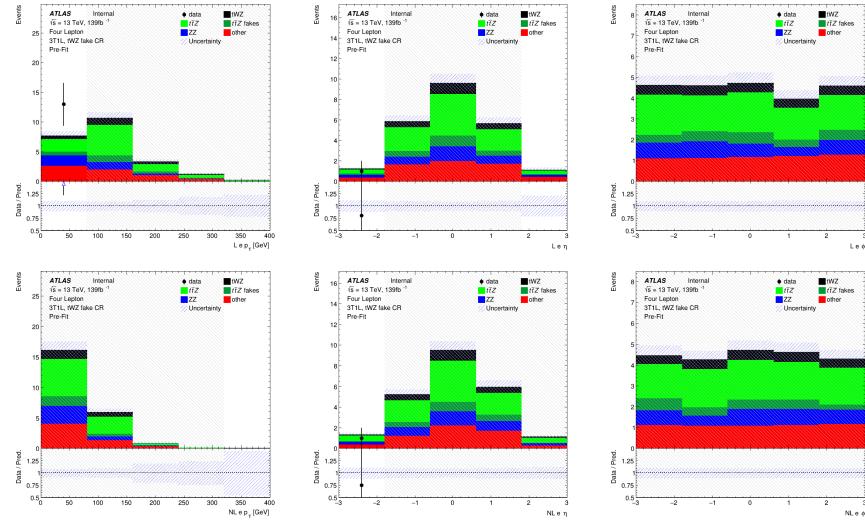


Figure A.55: MC predictions for p_T , η and ϕ for leading (L) electrons (top row) and next-to-leading (NL) electrons (bottom row) in the $(tWZ)_{\text{fake}}$ CR region

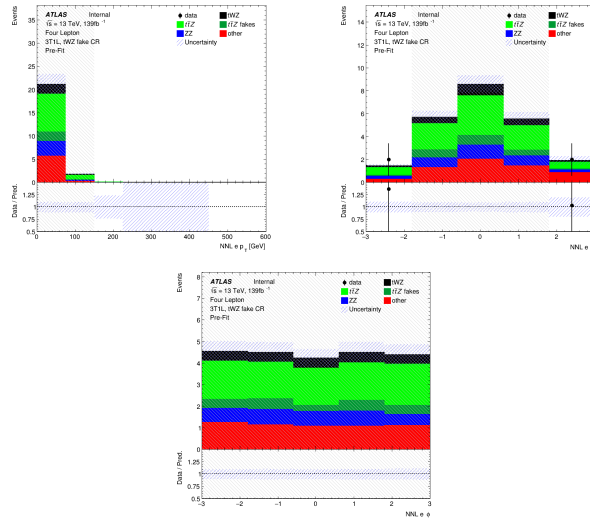


Figure A.56: MC predictions for p_T , η (top row) and ϕ (bottom row) for next-to-next-to-leading (NNL) electrons in the $(tWZ)_{\text{fake}}$ CR region

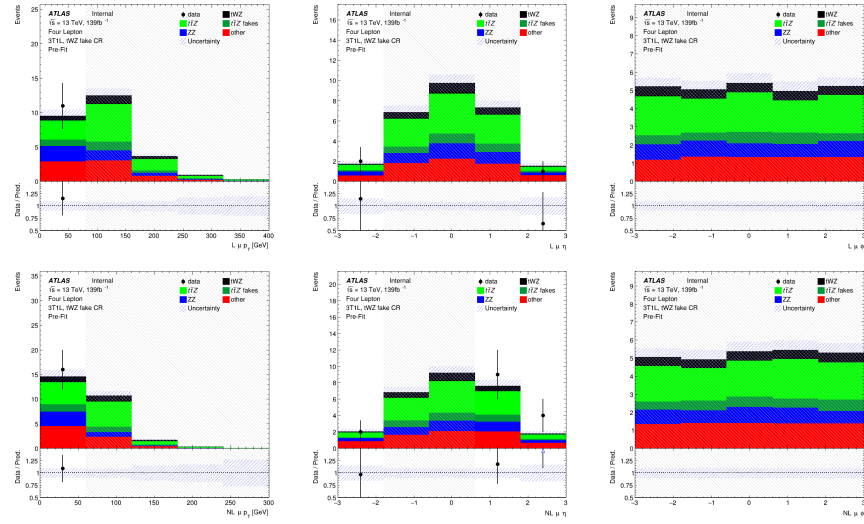


Figure A.57: MC predictions for p_T , η and ϕ for leading (L) muons (top row) and next-to-leading (NL) muons (bottom row) in the $(tWZ)_{\text{fake}}$ CR region

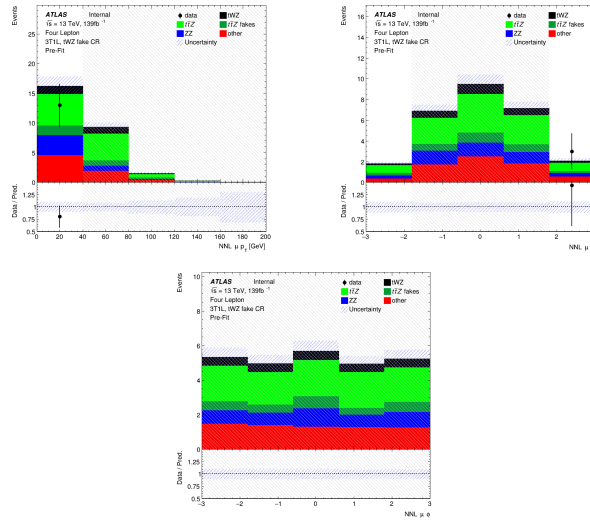


Figure A.58: MC predictions for p_T , η (top row) and ϕ (bottom row) for next-to-next-to-leading (NNL) muons in the $(tWZ)_{\text{fake}}$ CR region

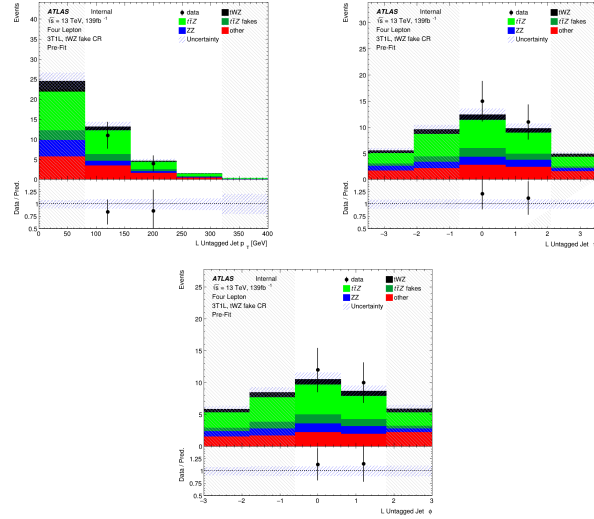


Figure A.59: MC predictions for p_T , η (top row) and ϕ (bottom row) for untagged jets in the $(tWZ)_{\text{fake}}$ CR region

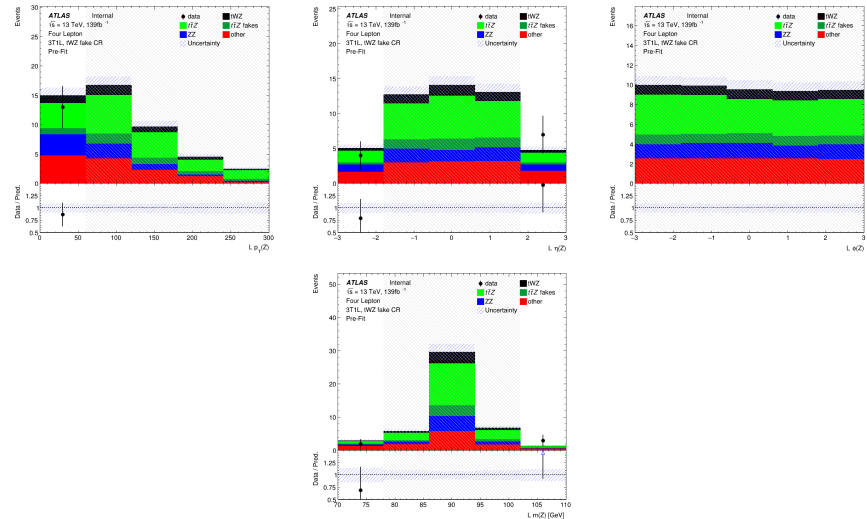


Figure A.60: MC predictions for p_T , η , ϕ (top row) and mass (m_Z) (bottom row) of the leading reconstructed Z candidate (OSSF lepton pair with $|m_{\text{OSSF}} - m(Z)| < 30$ GeV) in the $(tWZ)_{\text{fake}}$ CR region

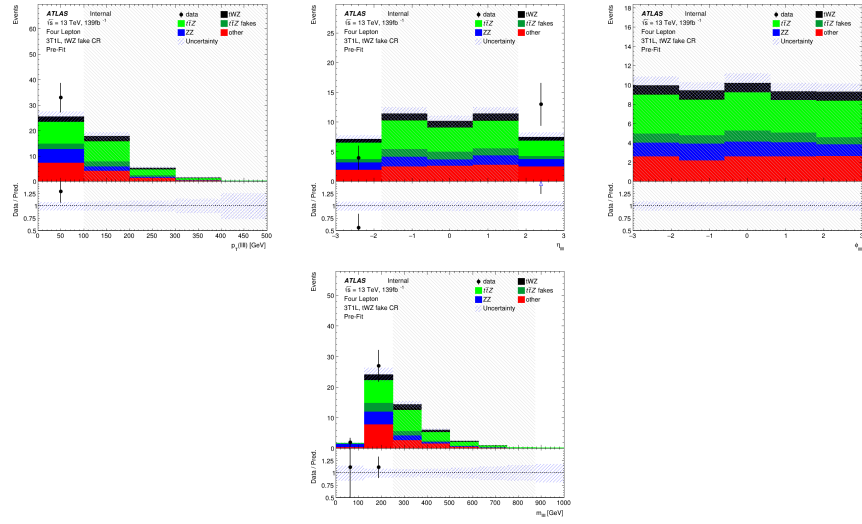


Figure A.61: MC predictions for p_T , η , ϕ (top row) and mass (bottom row) of the lepton system ($\ell\ell\ell\ell$) in the $(tWZ)_{\text{fake}}$ CR region

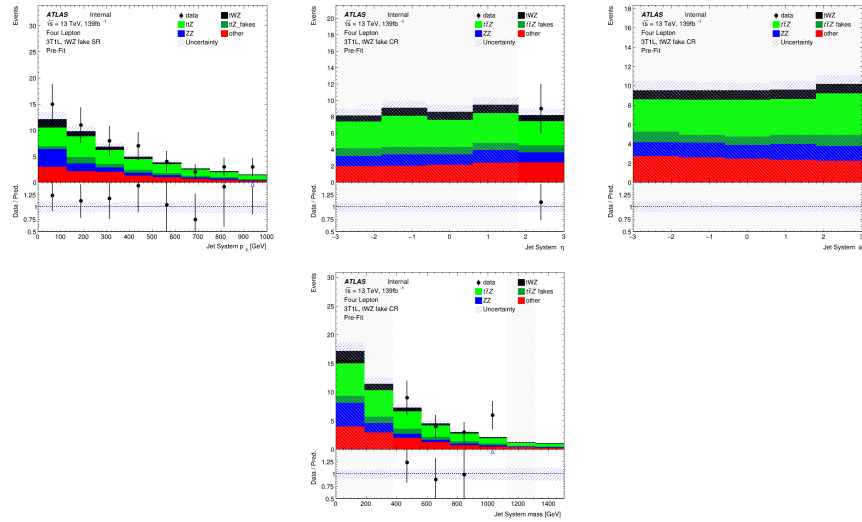


Figure A.62: MC predictions for p_T , η , ϕ (top row) and mass (bottom row) of the jet systems in the $(tWZ)_{\text{fake}}$ CR region

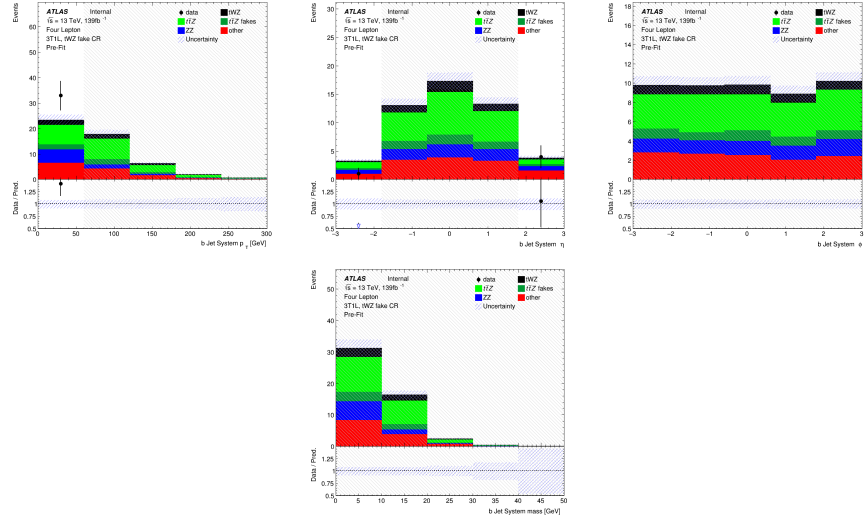


Figure A.63: MC predictions for p_T , η , ϕ (top row) and mass (bottom row) of the b-tagged jet systems in the $(tWZ)_{\text{fake}}$ CR region

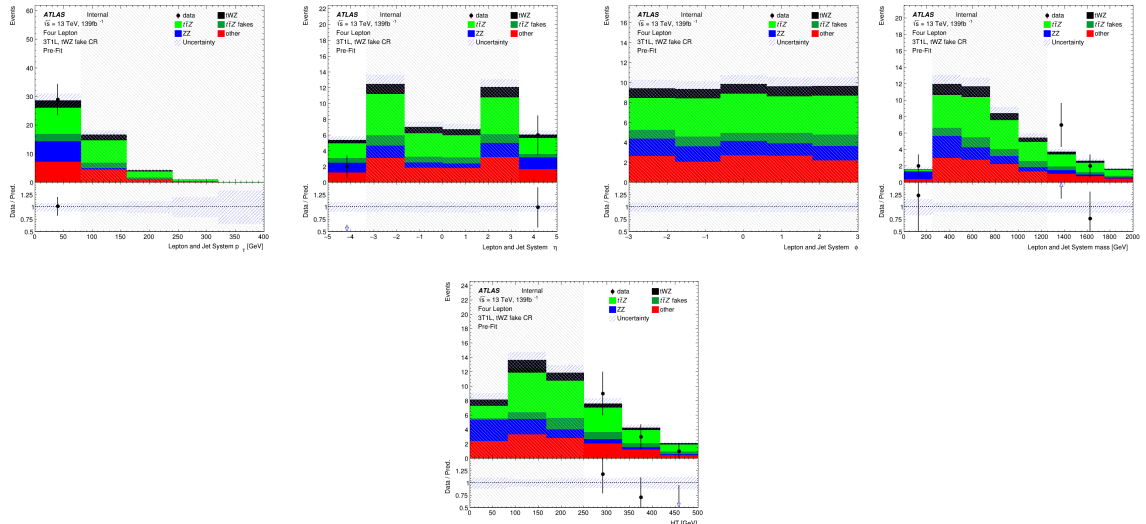


Figure A.64: MC predictions for p_T , η and ϕ (top row) and mass (bottom left) for the lepton + jet systems ($\ell\ell\ell\ell + \text{jets}$) in the $(tWZ)_{\text{fake}}$ CR region . Bottom right: MC predictions for H_T (scalar sum of jet p_T and lepton p_T) in the $(tWZ)_{\text{fake}}$ CR region

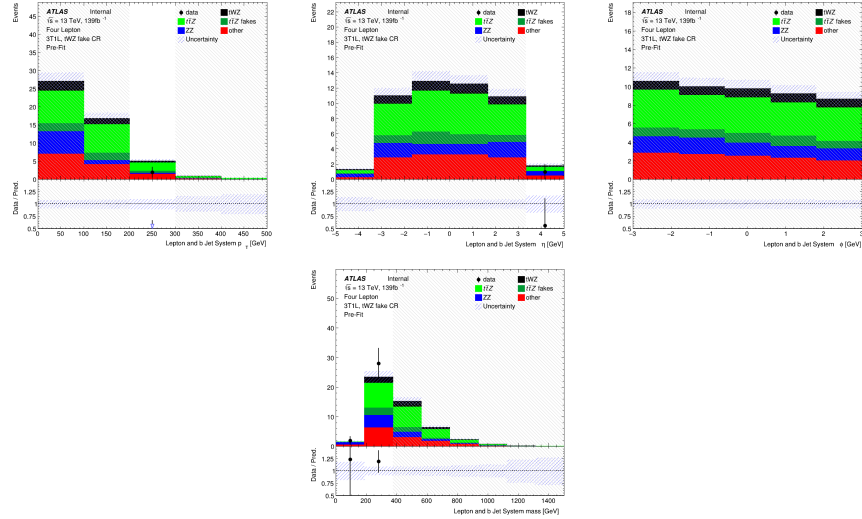


Figure A.65: MC predictions for p_T , η , ϕ (top row) and mass (bottom row) of the lepton + b-tagged jet systems ($\ell\ell\ell\ell +$ b-tagged jets) in the $(tWZ)_{\text{fake}}$ CR region

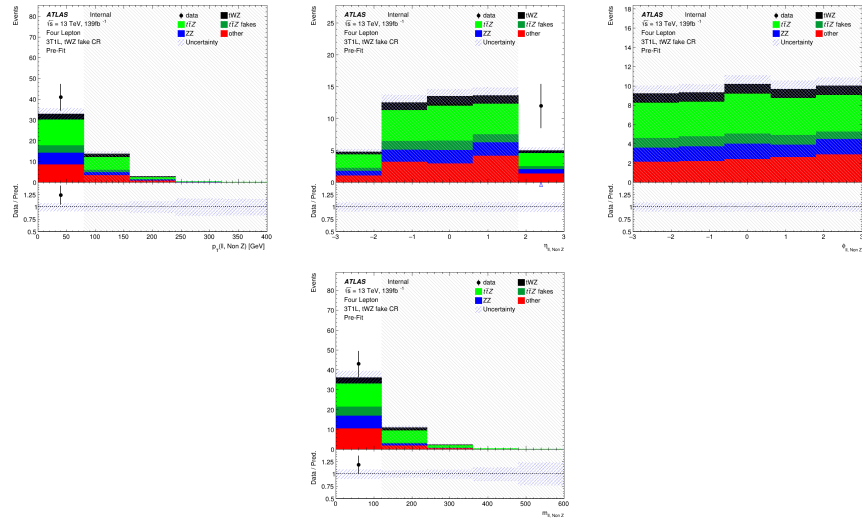


Figure A.66: MC predictions for p_T , η , ϕ (top row) and mass (bottom row) of reconstructed Non Z leptons (lepton pairs which don't originate from a Z candidate) in the $(tWZ)_{\text{fake}}$ CR region

1382

Bibliography

- 1383 [1] M. Aaboud et al. “Electron reconstruction and identification in the ATLAS experiment using the 2015 and
 1384 2016 LHC proton–proton collision data at $\sqrt{s} = 13$ TeV”. In: *The European Physical Journal C* 79.8 (Aug.
 1385 2019). ISSN: 1434-6052. DOI: 10.1140/epjc/s10052-019-7140-6. URL: <http://dx.doi.org/10.1140/epjc/s10052-019-7140-6>.
- 1387 [2] M. Aaboud et al. “Measurement of the $t\bar{t}Z$ and $t\bar{t}W$ cross sections in proton-proton collisions at $\sqrt{s} = 13$ TeV
 1388 with the ATLAS detector”. In: *Phys. Rev. D* 99 (7 Apr. 2019), p. 072009. DOI: 10.1103/PhysRevD.99.072009.
 1389 URL: <https://link.aps.org/doi/10.1103/PhysRevD.99.072009>.
- 1390 [3] Aaboud, M. and Aad, G. and Abbott, B. and Abbott, D. C. and Abdinov, O. and Abed Abud, A. and
 1391 Abhayasinghe, D. K. and Abidi, S. H. and AbouZeid, O. S. and et al. “Measurement of ZZ production
 1392 in the $\ell\ell\nu\nu$ final state with the ATLAS detector in pp collisions at $s \sqrt{s} = 13$ TeV”. In: *Journal of High
 1393 Energy Physics* 2019.10 (Oct. 2019). ISSN: 1029-8479. DOI: {10.1007/jhep10(2019)127}. URL: %7Bhttp:
 1394 //dx.doi.org/10.1007/JHEP10(2019)127%7D.
- 1395 [4] G. Aad et al. “Measurement of the $t\bar{t}$ production cross-section in the lepton+jets channel at $s=13$ TeV
 1396 with the ATLAS experiment”. In: *Physics Letters B* 810 (2020), p. 135797. ISSN: 0370-2693. DOI: <https://doi.org/10.1016/j.physletb.2020.135797>. URL: <https://www.sciencedirect.com/science/article/pii/S0370269320306006>.
- 1399 [5] G. Aad et al. “Muon reconstruction performance of the ATLAS detector in proton–proton collision data at
 1400 $\sqrt{s} = 13$ TeV”. In: *The European Physical Journal C* 76.5 (May 2016). ISSN: 1434-6052. DOI: 10.1140/epjc/s10052-016-4120-y. URL: <http://dx.doi.org/10.1140/epjc/s10052-016-4120-y>.
- 1402 [6] Georges Aad et al. “Topological cell clustering in the ATLAS calorimeters and its performance in LHC Run
 1403 1. Topological cell clustering in the ATLAS calorimeters and its performance in LHC Run 1”. In: *Eur. Phys.
 1404 J. C* 77 (Mar. 2016), 490. 87 p. DOI: 10.1140/epjc/s10052-017-5004-5. arXiv: 1603.02934. URL:
 1405 <https://cds.cern.ch/record/2138166>.
- 1406 [7] Shunichi Akatsuka and Shion Chen. *Isolation WPs summary: PLV + LowPtPLV*. Oct. 2019. URL: <https://indico.cern.ch/event/854783/contributions/3595486/attachments/1929380/3195230/PLV-Summary.pdf>.
- 1409 [8] Aaron Armbruster. *Asymptotic Formulae*. Feb. 2013. URL: https://indico.cern.ch/event/233551/contributions/493678/attachments/389871/542293/asymptotics_armbruster.pdf.
- 1411 [9] Pierre Astier et al. “Kalman filter track fits and track breakpoint analysis”. In: *Nuclear Instruments and
 1412 Methods in Physics Research Section A: Accelerators, Spectrometers, Detectors and Associated Equipment*
 1413 450.1 (2000), pp. 138–154. ISSN: 0168-9002. DOI: [https://doi.org/10.1016/S0168-9002\(00\)00154-6](https://doi.org/10.1016/S0168-9002(00)00154-6). URL:
 1414 <https://www.sciencedirect.com/science/article/pii/S0168900200001546>.
- 1415 [10] ATLAS Collaboration. “ATLAS b -jet identification performance and efficiency measurement with $t\bar{t}$ events in
 1416 pp collisions at $\text{sqrt}s = 13$ TeV”. In: *Eur. Phys. J. C* 79 (2019), p. 970. DOI: 10.1140/epjc/s10052-019-
 1417 7450-8. arXiv: 1907.05120 [hep-ex].
- 1418 [11] ATLAS Collaboration. *Calibration of light-flavour b -jet mistagging rates using ATLAS proton–proton collision
 1419 data at $\text{sqrt}s = 13$ TeV*. ATLAS-CONF-2018-006. 2018. URL: <https://cds.cern.ch/record/2314418>.
- 1420 [12] ATLAS Collaboration. “Electron and photon performance measurements with the ATLAS detector using
 1421 the 2015-2017 LHC proton-proton collision data”. In: *JINST* 14 (2019), P12006. DOI: 10.1088/1748-
 1422 0221/14/12/P12006. arXiv: 1908.00005 [hep-ex].

- [13] ATLAS Collaboration. “Identification and rejection of pile-up jets at high pseudorapidity with the ATLAS detector”. In: *Eur. Phys. J. C* 77 (2017), p. 580. DOI: 10.1140/epjc/s10052-017-5081-5. arXiv: 1705.02211 [hep-ex].
- [14] ATLAS Collaboration. *Measurement of b-tagging efficiency of c-jets in $t\bar{t}$ events using a likelihood approach with the ATLAS detector*. ATLAS-CONF-2018-001. 2018. URL: <https://cds.cern.ch/record/2306649>.
- [15] ATLAS Collaboration. “Measurements of b-jet tagging efficiency with the ATLAS detector using $t\bar{t}$ events at $\sqrt{s} = 13\text{TeV}$ ”. In: *JHEP* 08 (2018), p. 089. DOI: 10.1007/JHEP08(2018)089. arXiv: 1805.01845 [hep-ex].
- [16] ATLAS Collaboration. “Muon reconstruction and identification efficiency in ATLAS using the full Run 2 pp collision data set at $\sqrt{s} = 13\text{TeV}$ ”. In: (2020). arXiv: 2012.00578 [hep-ex].
- [17] Manuel Guth on behalf of the ATLAS collaboration. *Deep-Neural-Network-based b-Tagging as Basis for Improvements in Top Analyses*. URL: <https://cds.cern.ch/record/2693088/files/ATL-PHYS-SLIDE-2019-751.pdf>.
- [18] ATLAS Internal. *Electron Efficiencies for Analyses*. 2021. URL: <https://twiki.cern.ch/twiki/bin/viewauth/AtlasProtected/ElectronEfficienciesForAnalysis>.
- [19] ATLAS Internal. *Electron Efficiency Correlation Model*. 2021. URL: <https://twiki.cern.ch/twiki/bin/view/AtlasProtected/ElectronEfficiencyCorrelationModel>.
- [20] ATLAS Internal. *Jet Vertex Tagger for Run 2 in reco and analysis*. 2021. URL: <https://twiki.cern.ch/twiki/bin/view/AtlasProtected/JetVertexTaggerTool>.
- [21] ATLAS Internal. *Muon Efficiencies for Analyses*. 2021. URL: <https://twiki.cern.ch/twiki/bin/view/AtlasProtected/MuonEfficienciesForAnalysis>.
- [22] G. Avoni et al. “The new LUCID-2 detector for luminosity measurement and monitoring in ATLAS”. In: *JINST* 13.07 (2018), P07017. DOI: 10.1088/1748-0221/13/07/P07017.
- [23] Olga Bessidskaia Bylund. *Measurement of $t\bar{t}Z$ and $t\bar{t}W$ production at ATLAS in 13 TeV data, using trilepton and same charge dimuon final states*. Tech. rep. Geneva: CERN, Aug. 2016. DOI: 10.22323/1.276.0237. URL: <http://cds.cern.ch/record/2211022>.
- [24] Oliver Sim Brüning et al. *LHC Design Report*. CERN Yellow Reports: Monographs. Geneva: CERN, 2004. DOI: 10.5170/CERN-2004-003-V-1. URL: <https://cds.cern.ch/record/782076>.
- [25] Matteo Cacciari, Gavin P. Salam, and Gregory Soyez. “The anti- k_t jet clustering algorithm”. In: *JHEP* 04 (2008), p. 063. DOI: 10.1088/1126-6708/2008/04/063. arXiv: 0802.1189 [hep-ph].
- [26] Thomas Calvet. *Automatic binning implementation in TTHFitter - Htop(bb)*. URL: https://indico.cern.ch/event/455289/contributions/1953694/attachments/1209081/1762963/Calvet_binning_Htop-160108.pdf.
- [27] *CERN Twiki - TOP WG Summary Plots*. URL: <https://twiki.cern.ch/twiki/bin/view/LHCPhysics/LHCTopWGSummaryPlots>.
- [28] CERN Yellow Reports: Monographs. *CERN Yellow Reports: Monographs, Vol. 10 (2020): High-Luminosity Large Hadron Collider (HL-LHC): Technical design report*. en. 2020. DOI: 10.23731/CYRM-2020-0010. URL: <https://e-publishing.cern.ch/index.php/CYRM/issue/view/127>.
- [29] Shion Chen. *Track isolation variable for the PFlow WPs*. Oct. 2019. URL: https://indico.cern.ch/event/854783/contributions/3595529/attachments/1926980/3190772/IFF_20191003_PflowWPs.pdf.
- [30] CMS Collaboration. *Measurements of $pp \rightarrow ZZ$ production cross sections and constraints on anomalous triple gauge couplings at $\sqrt{s} = 13$ TeV*. 2020. arXiv: {2009.01186} (hep-ex).
- [31] The ATLAS Collaboration et al. “The ATLAS Experiment at the CERN Large Hadron Collider”. In: *Journal of Instrumentation* 3.08 (Aug. 2008), S08003–S08003. DOI: 10.1088/1748-0221/3/08/s08003. URL: <https://doi.org/10.1088/1748-0221/3/08/s08003>.
- [32] I. Connelly. “Performance and calibration of b-tagging with the ATLAS experiment at LHC Run-2”. In: 2017.
- [33] Glen Cowan et al. “Asymptotic formulae for likelihood-based tests of new physics”. In: *The European Physical Journal C* 71.2 (Feb. 2011). ISSN: 1434-6052. DOI: 10.1140/epjc/s10052-011-1554-0. URL: <http://dx.doi.org/10.1140/epjc/s10052-011-1554-0>.

- [34] Federico Demartin et al. “tWH associated production at the LHC”. In: *Eur. Phys. J. C* 77.1 (2017), p. 34. DOI: 10.1140/epjc/s10052-017-4601-7. arXiv: 1607.05862 [hep-ph].
- [35] *Electron identification efficiency in data for electrons with $E_T > 30\text{GeV}$* . URL: https://atlas.web.cern.ch/Atlas/GROUPS/PHYSICS/PAPERS/EGAM-2018-01/fig_16.png.
- [36] F. Englert and R. Brout. “Broken Symmetry and the Mass of Gauge Vector Mesons”. In: *Phys. Rev. Lett.* 13 (9 Aug. 1964), pp. 321–323. DOI: 10.1103/PhysRevLett.13.321. URL: <https://link.aps.org/doi/10.1103/PhysRevLett.13.321>.
- [37] *Errors in weighted histograms*. URL: <https://www.zeuthen.desy.de/~wischnew/amanda/discussion/wgterror/working.html>.
- [38] Guido Fantini et al. *The formalism of neutrino oscillations: an introduction*. 2020. arXiv: 1802.05781 [hep-ph].
- [39] Steve Farrell. *Overlap Removal Tools, FTAG/Hbb Workshop*. URL: https://indico.cern.ch/event/631313/contributions/2683959/attachments/1518878/2373377/Farrell_ORTools_ftaghbb.pdf.
- [40] *GoodRunListsForAnalysisRun2*. URL: <https://twiki.cern.ch/twiki/bin/viewauth/AtlasProtected/GoodRunListsForAnalysisRun2>.
- [41] Particle Data Group et al. “Review of Particle Physics”. In: *Progress of Theoretical and Experimental Physics* 2020.8 (Aug. 2020). 083C01. ISSN: 2050-3911. DOI: 10.1093/ptep/ptaa104. eprint: <https://academic.oup.com/ptep/article-pdf/2020/8/083C01/33653179/ptaa104.pdf>. URL: <https://doi.org/10.1093/ptep/ptaa104>.
- [42] Peter W. Higgs. “Broken Symmetries and the Masses of Gauge Bosons”. In: *Phys. Rev. Lett.* 13 (1964). Ed. by J. C. Taylor, pp. 508–509. DOI: 10.1103/PhysRevLett.13.508.
- [43] Peter W. Higgs. “Spontaneous Symmetry Breakdown without Massless Bosons”. In: *Phys. Rev.* 145 (1966), pp. 1156–1163. DOI: 10.1103/PhysRev.145.1156.
- [44] *IFFTruthClassifier GitLab Repository*. URL: <https://gitlab.cern.ch/ATLAS-IFF/IFFTruthClassifier/-/tree/master>.
- [45] *IFFTruthClassifier Lepton Categories*. URL: <https://gitlab.cern.ch/ATLAS-IFF/IFFTruthClassifier/-/tree/master#3-details-about-the-lepton-categories>.
- [46] F. Jegerlehner. “The hierarchy problem of the electroweak Standard Model revisited”. In: (May 2013).
- [47] V. Khachatryan et al. “Measurement of the ZZ production cross section and $Z \rightarrow \ell^+\ell^-\ell^+\ell^-$ branching fraction in pp collisions at $\sqrt{s} = 13\text{TeV}$ ”. In: *Physics Letters B* 763 (2016), pp. 280–303. ISSN: 0370-2693. DOI: <https://doi.org/10.1016/j.physletb.2016.10.054>. URL: <https://www.sciencedirect.com/science/article/pii/S0370269316306256>.
- [48] Luigi Marchese. *Lepton and photon reconstruction and identification performance in ATLAS and CMS*. Tech. rep. Geneva: CERN, Sept. 2019. DOI: 10.22323/1.350.0237. URL: <https://cds.cern.ch/record/2688452>.
- [49] Thomas McCarthy. *Macro developed to compare t/W/Z reconstruction performance (2ℓ , 3ℓ , 4ℓ)*. URL: https://indico.cern.ch/event/986357/contributions/4172907/attachments/2169451/3666801/reco_performance_macro_20210112.pdf.
- [50] Thomas McCarthy and Florian Fischer. *Exploiting full/partial $t\bar{t}$ reconstruction for background suppression in 2ℓ* . URL: https://indico.cern.ch/event/955360/contributions/4016465/attachments/2102418/3534816/top_reco_bkgd_suppression_2L_20200915.pdf.
- [51] *MCTruthClassifier - ATLAS Twiki*. URL: <https://twiki.cern.ch/twiki/bin/view/AtlasProtected/MCTruthClassifier>.
- [52] F. Meloni. “Primary vertex reconstruction with the ATLAS detector”. In: *Journal of Instrumentation* 11.12 (Dec. 2016), pp. C12060–C12060. DOI: 10.1088/1748-0221/11/12/c12060. URL: <https://doi.org/10.1088/1748-0221/11/12/c12060>.
- [53] Users MissMJ and Cush. *Standard model of elementary particles - Wikimedia Commons*. URL: https://en.wikipedia.org/wiki/File:Standard_Model_of_Elementary_Particles.svg.
- [54] *Monte Carlo to Monte Carlo scale factors for flavour tagging efficiency calibration*. Tech. rep. ATL-PHYS-PUB-2020-009. Geneva: CERN, May 2020. URL: <https://cds.cern.ch/record/2718610>.

- 1521 [55] *MuonSelectionTool, ATLAS TWiki*. URL: <https://twiki.cern.ch/twiki/bin/view/Atlas/MuonSelectionTool>.
- 1522
- 1523 [56] O Oncel. *Search for Single Top Quark Production in Association with a W and a Z Boson in the 3 Lepton Final State with the ATLAS Experiment at 13 TeV*. URL: <https://cds.cern.ch/record/2625170>.
- 1524
- 1525 [57] *Option to force a shape withing an error band by hand - TRF documentation*. URL: https://trexfitter-docs.web.cern.ch/trexfitter-docs/model_building/shape/.
- 1526
- 1527 [58] *Pileup jet recommendations*. URL: <https://twiki.cern.ch/twiki/bin/view/AtlasProtected/PileupJetRecommendations>.
- 1528
- 1529 [59] *Recommended isolation working points*. URL: <https://twiki.cern.ch/twiki/bin/view/AtlasProtected/RecommendedIsolationWPs>.
- 1530
- 1531 [60] *scikit-learn Documentation - Gradient Boosting Classifier*. URL: <https://scikit-learn.org/stable/modules/generated/sklearn.ensemble.GradientBoostingClassifier.html>.
- 1532
- 1533 [61] *Scikit-Learn GradientBoostingClassifier Documentation*. URL: <https://scikit-learn.org/stable/modules/generated/sklearn.ensemble.GradientBoostingClassifier.html>.
- 1534
- 1535 [62] *TopRecoObjTwikiModel*. URL: <https://twiki.cern.ch/twiki/bin/view/AtlasProtected/TopRecoObjTwikiModel>.
- 1536
- 1537 [63] *Total Integrated Luminosity and Data Quality in 2015-2018 - LuminosityPublicResultsRun2*. URL: <https://twiki.cern.ch/twiki/bin/view/AtlasPublic/LuminosityPublicResultsRun2>.
- 1538
- 1539 [64] *TRExFitter*. URL: <https://twiki.cern.ch/twiki/bin/viewauth/AtlasProtected/TtHFitter>.
- 1540
- 1541 [65] *TRExFitter: Mixed data and MC fit*. URL: <https://trexfitter-docs.web.cern.ch/trexfitter-docs/AdvancedTutorial2020/Mixed/>.
- 1542
- 1543 [66] Benjamin Warren. “A search for tWZ production in the trilepton channel using Run 2 data from the ATLAS experiment.” In: (2021).
- 1544
- 1545 [67] Kenneth G. Wilson. “Confinement of quarks”. In: *Phys. Rev. D* 10 (8 Oct. 1974), pp. 2445–2459. DOI: 10.1103/PhysRevD.10.2445. URL: <https://link.aps.org/doi/10.1103/PhysRevD.10.2445>.